Volumetric Imaging Using 2D Phased Arrays

JESSICA G. MCKEE

University of BRISTOL

Department of Mechanical Engineering

A dissertation submitted to the University of Bristol in accordance with the requirements for award of the degree of DOCTOR OF PHILOSOPHY in the Faculty of Engineering.

FEBRUARY 2021

Word count: 26,609

Author's Declaration

I declare that the work in this dissertation was carried out in accordance with the requirements of the University's *Regulations and Code of Practice for Research Degree Programmes* and that it has not been submitted for any other academic award. Except where indicated by specific reference in the text, the work is the candidate's own work. Work done in collaboration with, or with the assistance of, others, is indicated as such. Any views expressed in the dissertation are those of the author.

SIGNED: ..... DATE: .....

Abstract

Phased arrays are commonly employed in the ultrasonic non-destructive testing of industrial components. Their use allows the full-matrix capture (FMC) acquisition technique to be used; this contains all possible information of an inspection for a specific array location, and therefore allows a number of imaging algorithms to be applied in post-processing. One such algorithm, termed the total focusing method (TFM), produces fully focused images of inspection regions and outperforms conventional imaging techniques.

Having access to three-dimensional (3D) volumetric knowledge of a specimen's interior is imperative for accurate inspections, as it enables any defects present to be accurately characterised so their severity can be evaluated. The type of array used also has an impact on the resulting TFM images. As two-dimensional (2D) phased arrays have the ability to focus in multiple directions, more information regarding a defect is able to be obtained from a single array location when compared to a linear one-dimensional (1D) array. Furthermore, the use of a 2D array can speed up inspections and reduce data size, as volumetric inspections with a linear array requires multiple data sets to be captured as the array is scanned over a given area. This thesis aims to demonstrate the benefits of using a 2D array over a linear array when obtaining accurate volumetric knowledge of defects.

A 2D array is also used to investigate 3D volumetric imaging of defects within a complex-shaped specimen, which is a current challenge in industry. This is achieved by extracting an estimate of the surface profile using a novel TFM image-based method. The extracted surface is then used to produce another 3D TFM image of the interior of the specimen to enable defect detection and characterisation to be investigated. Scanned array inspections using a 2D array are also explored to investigate the 3D characterisation of machined defects within a large specimen.

The response of a defect varies with inspection setup, which can result in one region of the specimen being viewed well from one array position and poorly from another. This effect is investigated by generating a 3D ultrasonic model of the predicted defect response and using it to improve the detection of defects within simple and complex specimens.

Acknowledgements

Firstly, I would like to express my deepest gratitude to my supervisors, Professor Paul Wilcox and Dr. Rob Malkin, for their guidance, encouragement and dedication of time over the course of this work. Their insights have been invaluable and I would not have been able to do any of this without them.

This work was made possible by Frazer-Nash Consultancy and the Ministry of Defence (MOD), and I wish to thank Dr. Brian Gribben and Mr. Mike Anderson in particular for their support and eagerness to help in any way they could over the past four years.

My appreciation extends to the Ultrasonics and Non-Destructive Testing group in Bristol and my colleagues. It has been exciting to be part of such a dynamic and intelligent group of people who helped keep my spirits high and were always up for a good chat. Special thanks go to Dr. Rhodri Bevan and Dr. Nicolas Budyn for sharing their ideas and code with me; I am extremely grateful for their patience and good humour during times when I thought all hope was lost.

The Research Centre in NDE (RCNDE) also deserves some praise; I am grateful for the opportunities and courses that were made available to me, along with the experiences I had and people I met along the way.

I would also like to thank my close friends for keeping me humble and pretending to be interested in my research. They always made time when the pressure got too intense and never let me give up.

Finally, I am eternally indebted to my parents, Andrew and Kerry, my sister Holly and the rest of my family members for their unwavering belief in my abilities and support throughout my studies.

Author's publications

1. J. G. McKee, P. D. Wilcox, & R. E. Malkin, *Effect of surface compensation for imaging through doubly-curved surfaces using a 2D phased array,* in AIP Conference Proceedings, 38 (2019). https://doi.org/10.1063/1.5099836

2. J. G. McKee, R. L. T. Bevan, P. D. Wilcox & R. E. Malkin *Volumetric imaging through a doubly-curved surface using a 2D phased array,* NDT and E International, 113 (2020). https://doi.org/10.1016/j.ndteint.2020.102260

Table of Contents

List of Figures

List of Tables

Abbreviations

NDT	Non-destructive testing
NDE	Non-destructive evaluation
UT	Ultrasonic testing
1D	One-dimensional
1.5D	One-and-a-half dimensional
2D	Two-dimensional
3D	Three-dimensional
dB	Decibel
TFM	Total Focusing Method
FMC	Full-matrix capture
HMC	Half-matrix capture
PWI	Plane Wave Imaging
ToF	Time-of-flight
FBH	Flat bottom hole
SNR	Signal-to-noise ratio
MB	Megabyte
CPU	Central processing unit
GPU	Graphics processing unit
BDH	Bottom drilled hole
EDM	Electrical discharge machining

RMSE	Root-mean square error
DE	Differential evolution
S-matrix	Scattering matrix
RBH	Round bottom hole

Symbols

f_c	Array centre frequency
x	Primary/secondary imaging axis
y	Primary/secondary imaging axis
z	Depth imaging axis
T	Transmitting element index
R	Receiving element index
$\mathbf{E}$	Position vector of element (with transmission (T) and reception (R) components)
$\mathbf{P}$	Position vector of image point (with various components defined in text)
v	Velocity of sound (with various components defined in text)
I	Image intensity (2D or 3D)
τ	Time
h	Complex analytic signal of an A-scan
V	Volume (with component defined in text)
λ	Wavelength (with various components defined in text)
$\mathbf{A}$	Position vector of surface-crossing location (with transmission (T) and reception (R) components)
ε	Size of single-medium TFM window in z
Z	Locations of extracted 3D surface points in z
σ	Standard deviation
θ	Angle (various components defined in text)

D	Directivity coefficient
ϕ	Beam elevation angle
E	Sensitivity image intensity
B	Beamspread coefficient
Γ	Transmission coefficient
S	Scattering matrix
ρ	Material density (various components defined in text)
d	Hole diameter
l	Slot length

Chapter 1

Introduction

Non-destructive testing (NDT), also known as non-destructive evaluation (NDE), refers to the collection of techniques that can be used to test and analyse industrial components for defects, flaws or weaknesses to evaluate the useability of a component or system without causing permanent damage. This is an essential process in industries such as power generation [1, 2], aerospace [3] and transport [4], where failure of a component could lead to catastrophic damage. Developments in NDT over the last few decades have made it possible to obtain accurate internal images of solid structures within the engineering design process, after part manufacture is completed and during service. Frequently used NDT techniques include ultrasonic testing (UT), electromagnetic testing (ET), magnetic particle testing (MPI), radiography, dye penetrant inspection (DPI) and visual inspection. It is common for multiple inspection techniques to be used in conjunction with others, but the geometry of the component or type of defect being imaged can have an impact on the chosen method. For example, radiography is preferred when inspecting small-bore and thin-walled tubing welds, while UT is desirable when collecting thickness measurements over time in the case of pipe corrosion. UT in particular is a highly desirable technique to use in industry due to the flexibility of inspections, ability to obtain high resolution internal images, lack of harm to the operator and potential for real-time imaging. This introductory chapter introduces the principles of phased arrays and their use in volumetric UT, along with the motivation for this work.

1.1 Ultrasonic phased arrays

UT involves transmitting a high-frequency sound pulse into a component and processing the reflected signals to generate an image. If the pulse encounters a change in material property or density, such as a boundary or crack, the signal is reflected and can be picked up by the transducer at a registered time. Traditionally this pulse was generated from a single-element transducer and yielded a time-amplitude trace, termed an A-scan, which could be presented graphically. Single-element transducers consist of a single crystal element in a casing which vibrates when exposed to electrical signals; the crystal both transmits and receives sound energy and is therefore the foundation of all ultrasonic imaging methods. Any density or material property changes that a sound pulse encounters can be identified by the timing of peaks in the A-scan, which correspond to positions that can easily be calculated using the time the peak occurs and the acoustic velocity of the sound wave in the component. While A-scans are an effective tool for thickness measurements, they are not effective at characterising the interior of a specimen beyond identifying large defects. Therefore, key limitations of using single-element probes in UT inspections include the inability to vary focal depth, a restricted number of fixed directions available from which to detect defects, and the consequent potential for missing defects that are in unexpected positions or orientations. It is for these reasons that research groups began to focus on ultrasonic phased arrays and their ability to improve inspections.

Ultrasonic phased arrays, more commonly referred to as just ‘arrays’, are composed of many single-element transducers, and therefore have the benefits of electronic beam steering, focusing and scanning by applying delay laws to individually addressable elements [5]. As a direct result of these properties, phased arrays can be applied to a wider range of imaging scenarios and have the ability to speed up ultrasonic inspections significantly, along with improving defect image resolution [6]. Arrays typically contain between 64–128 individual elements, with the maximum number limited by the number of channels available in the array controller. Array controllers exist that can accommodate arrays with up to 512 elements, however arrays of this type are relatively rare due to electrical complexity and cost.

Arrays are typically designed to be either one-dimensional (1D), one-and-a-half-dimensional (1.5D) or two-dimensional (2D). Descriptions of these types of arrays are given in the following sections.

1.1.1 1D arrays

Linear 1D arrays, or simply just linear arrays, are composed of a row of single-element transducers arranged in a straight line, as shown in Fig. 1.1(a). The elements are spaced along the x direction and are comparatively long in the y direction, so therefore are assumed to behave as infinitely long strip sources. Traditional imaging methods involved transmitting a sub-aperture of elements in the array; this was most commonly achieved by pulsing all elements in a sub-aperture simultaneously to behave as a monolithic transducer. Upon capturing an A-scan, the aperture is moved one element along and the process is repeated until the last element is included in the aperture; advancing the aperture beyond this limit results in an aperture with fewer elements than it initially contained. When the A-scans are stacked side-by-side they represent a 2D B-scan image, displaying depth below the array and lateral distance. As the area insonified by a linear array is substantially larger when compared to a single-element transducer, physical movement of the array is not required between A-scan capture when imaging the same size of area. By manipulating the delay laws to a selection of elements, focused and sector B-scans can be obtained to provide more information of a region [7]. B-scans are commonly used in medical imaging for a wide range of applications due to their ease of implementation and ability to image in real-time [8]. The interactions of different pairs of elements can also be investigated depending on the data capture method, so inspections with a linear array are not limited to pulse-echo.

Despite the many benefits linear arrays have over single-element transducers, they still do not demonstrate the true potential of phased array technology. A substantial limitation of using linear arrays is that the steering is confined to a single plane and therefore there is no ability to control focusing in the plane perpendicular to the image plane, or the out-of-plane direction [9]. This means that inspections with this type of array are limited to 2D slices, which is of particular concern when building up a volumetric image of the interior of a component, or imaging through surfaces that are curved in multiple directions. Three-dimensional (3D) volumetric inspections using a linear array have previously been achieved by translating the array in the out-of-plane direction and combining the resulting images together to reconstruct a ‘pseudo-3D’ volume from a series of 2D slices [10]. As there is the possibility of missing scattering effects in the out-of-plane direction, there is the subsequent chance of completely missing defects that are in unexpected positions or orientations.

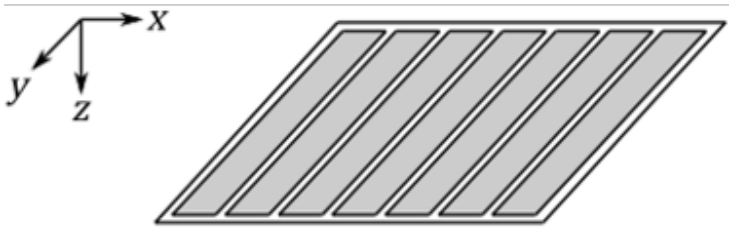

(a)

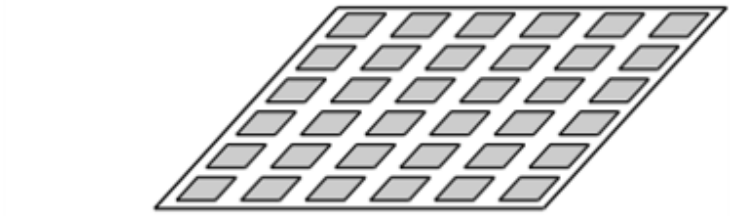

(b)

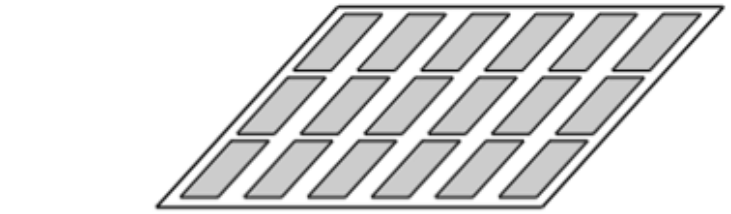

(c)

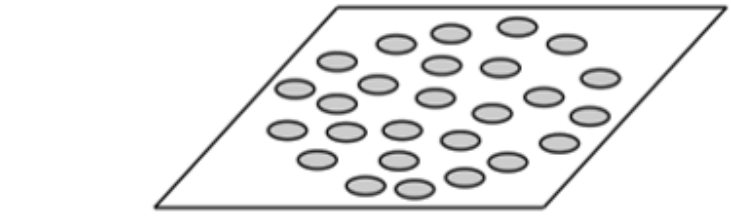

(d)

FIGURE 1.1. Element layout for a (a) linear 1D array, (b) matrix 2D array, (c) matrix 1.5D array and (d) sparse 2D array.

1.1.2 2D arrays

A 2D array is characterised by having its elements distributed across a 2D aperture. By distributing elements in this way, it is possible to better characterise defects within components as beam manipulation can occur throughout a 3D volume without requiring movement of the array, along with the ability to probed a defect over a larger range of solid angles [11]. This ability significantly increases coverage of the imaging region, as long as the array and surface orientations are favourable, and allows a more detailed inspection through volumetric beam steering and focusing. Due to the layout of elements in this type of array, the ultrasonic beam can be focused in both lateral directions. As a result, components with complex surfaces can be inspected and defects in unexpected orientations have a higher likelihood of being detected.

When considering the design of 2D arrays, there are infinite possibilities of element layouts. Researching the optimal element layout has been the focus of research over the past couple of decades [6, 12–15] and two common types of 2D arrays are considered in the current work.

Matrix 2D

The most intuitive 2D array design consists of elements arranged in a grid layout, termed a matrix array, as illustrated in Fig. 1.1(b). This type of array is essentially an extension of a linear array, where the long elements have been divided into smaller, independent square elements arranged in a regular grid orientation across the x and y directions. A major problem with matrix arrays is the requirement of the inter-element spacing, or pitch, to be less than half the wavelength of emitted waves. This limit is derived from the Nyquist spatial sampling critera and is needed to avoid aliasing effects in the form of unwanted grating lobes, which can minimise energy in the main lobe and hence reduce overall imaging capabilities in periodic arrays [16, 17]. At the same time, a wide spatial extension is necessary for high resolution imaging, as the lateral resolution is directly dependent on aperture size. To enhance array performance the number of elements can be increased while maintaining the pitch constraint, but this quickly increases the number of elements required, and therefore complexity and cost. Furthermore, the periodic spacing of elements in a matrix array also results in the appearance of grating lobes [11, 18].

An alternative matrix element layout has been presented in the form of a 1.5D

array, whereby the linear elements are coarsely divided into rectangles in the y direction, as shown in Fig. 1.1(c). As a result, the number of elements in a row does not equal the number of elements in a column, as is typical in a matrix 2D array. The number of elements has been reduced, while still enabling focusing in the out-of-plane direction for enhanced detection capability [19, 20]. However, finer resolution of elements in the y direction is necessary for beam steering and only 2D images are formed using this type of array. It is for this reason that 1.5D arrays are unused in the current work.

Sparse 2D

Research has demonstrated that a sparse 2D array with elements arranged in a Poisson disk distribution outperforms a matrix 2D array with the same number of elements [5, 11]. This is a result of the non-periodic element layout preventing the formation of grating effects while still maintaining a high level of imaging resolution. In this configuration, circular elements are randomly distributed across the aperture with a constraint applied to the minimum separation distance. Although the presence of grating lobes has been removed, a consequence of the sparseness of the array is that the overall background noise in the image increases, and hence lowers the signal-to-noise ratio (SNR). This is a result of the psuedorandom spacing of elements dispersing the energy of would-be grating lobes into the surrounding environment. An illustration of the element layout for an array of this type is shown in Fig. 1.1(d).

1.1.3 Array parameters

Descriptions of the Immasonic (Besançon, France) arrays used in the current work are given in Table 1.1; to collect data throughout this thesis, the commercial array controller device MicroPulse FMC (Peak NDT Ltd., Derby, UK) was used.

The dimensions, shape and pitch of an element all contribute towards the nature of the ultrasonic field produced. In both the linear 1D and matrix 2D arrays, the element pitch is determined by the Nyquist criterion, which states that the pitch in a periodic array should be less than half the wavelength of emitted sound waves. Both arrays were manufactured for anticipated use in metals, as both pitches satisfy the half-wavelength criterion when travelling with velocities greater than ~3000 m/s and ~6000 m/s respectively. As it is not necessary to satisfy the Nyquist criterion when considering an irregular distribution of elements, the pitch of the sparse 2D array can

be larger than $\lambda/2$ while still avoiding grating lobes. However, the pitch must be large enough to avoid cross-coupling between neighbouring elements, but small enough to allow high resolution imaging. This results in the ability to create a sparse 2D array with a larger aperture than would be possible using a matrix 2D array using the same number of elements. The sparse 2D array was designed to operate at 3 MHz in order to be comparable with the matrix 2D array. Although the classic Nyquist rule for the element pitch of a periodic array design is well known, a study in [18] shows that the pitch can be increased without significant degradation of image quality, providing angle limits are applied to the aperture. This means that future arrays of a certain size could be populated with larger pitches and fewer elements to reduce data sizes, and ultimately speed up inspections.

The length and width values associated with a circular element in the sparse 2D array are equal and represent the element diameter. Matrix 2D arrays typically have square-shaped elements, while the sparse 2D array contains circular elements; elements of this shape complement the Poisson disk shape and produce symmetrical ultrasonic beams. The bandwidth is defined here as the magnitude of the spread of frequencies corresponding to 6 dB below the maximum signal amplitude (defined to be 0 decibels, or dB), or the full width at half maximum (FWHM).

TABLE 1.1. Parameters of the linear 1D, matrix 2D and sparse 2D arrays used in the current work.

Array type	Linear 1D	Matrix 2D	Sparse 2D
Element properties			
Count	128	121 (11x11)	128
Shape	Rectangular	Square	Circular
Length (mm)	15.0	0.8	1.7
Width (mm)	0.2	0.8	1.7
Pitch (mm)	0.3	1.0	$\geq$ 1.9
Spacing (mm)	0.1	0.2	$\geq$ 0.2
Array properties			
Active area (mm)	38.5 x 15.0	10.8 x 10.8	$\approx 15^2\pi$
Centre frequency (MHz)	5	3	3
Bandwidth (–6 dB)	$\geq$ 2.5	> 1.5	$\geq$ 1.5

1.2 Ultrasonic imaging techniques

Ultrasonic imaging is generally conducted in three main stages: acquisition, reconstruction and visualisation. Acquisition refers to the collection of time-domain data from an experimental setup, reconstruction aims to process the information contained in the collected data set by applying an imaging algorithm, and visualisation is the method of displaying the final image result.

Up to this point, the reconstruction of data has only been discussed in terms of B-scans. While arrays have the ability to produce focused B-scans, this is limited to a predefined depth in a component. This is a problem when the location of a defect is unknown and an accurate image of a region within a component is to be obtained. It therefore follows that a fully-focused image would be optimal. Within recent decades, computer power has enabled improvements in post-processing techniques that allow data sets to be processed offline instead of physical beam forming at the time of inspection. This enabled an imaging algorithm, termed the Total Focusing Method (TFM), to be implemented, which focuses the full array in both transmission and reception at every point in a defined imaging grid [7]. TFM imaging requires the full-matrix capture (FMC) data set containing the A-scans of all transmit-receive element pair combinations and results in n^2 scans, where n is the number of elements in a given array. Time-domain data acquired in this format contains the maximum possible amount of information of a setup, and therefore can result in large data files and slow scanning speeds. A practice for reducing the amount of data collected can be used, whereby reciprocities can be eliminated by assuming that the A-scan obtained from transmitting from element T and receiving on element R is identical to the A-scan obtained by transmitting from R and receiving on T. This results in the half-matrix data set being captured, termed the HMC [5], which reduces the number of A-scans to $n(n+1)/2$. Inspection is therefore sped up without a significant loss of data, and hence HMC is used throughout the current work.

While TFM offers clear imaging advantages, obtaining the FMC data set requires at least n separate transmissions and processing can be computationally intensive. An alternative imaging approach known as Plane Wave Imaging (PWI) has been shown to produce images with equivalent quality to those obtained using TFM, but with fewer transmissions [21–23]. The basic premise of capturing data for PWI is to emit m plane waves at m different angles into a component and receive the backscattered signals on all n elements in parallel, resulting in a $m \times n$ matrix. The higher power input into the

component, along with significantly fewer acquisition cycles makes PWI an appealing alternative imaging method. However, 3D imaging using plane waves has yet to be fully explored and not investigated in the current work.

Volumetric images of processed data can be challenging to visualise, but are typically displayed by (i) 2D slices through a chosen image point, or (ii) showing the location of 3D amplitude values above a specified threshold. The type of images produced depends on the properties of the transducer that was used. Real-time imaging is possible with present technology, however significant optimisations are required during post-processing due to the large number of calculations.

1.3 Motivation

When a component contains a flaw or defect hidden beneath the surface, the structural integrity can be compromised depending on the nature of the defect. Distinguishing between defect types is crucial for thorough and accurate inspections, as the severity of defects depends on their size, orientation and shape; for instance, it is well known that planar discontinuities (e.g. cracks) are usually more dangerous than volumetric defects (e.g. voids) due to their sharp edges that have the potential to grow and cause breaks. To enable precise defect characterisation, it is therefore necessary to obtain volumetric information about defects. 2D arrays have the ability to obtain volumetric defect information from a single location, and their use is therefore desirable for UT inspections.

A cross sector problem in the NDT industry is the inspection of defects within regions where the surface geometry of a component curves in multiple directions, also known as doubly curved surfaces, such as those found in turbine blades, pipework branches and nozzles. Current inspection procedures through these surfaces involve using either (i) a single-element transducer that probes the region from a range of locations, or (ii) radiography. The use of a single-element transducer means that a highly-skilled operator needs to interpret the data and it is extremely challenging to build up a volumetric image of the region, while radiography is not very effective for detecting and sizing planar defects without prior knowledge of their likely location and orientation [24]. Developments over the past few decades have introduced phased array transducers to the UT process and the choice of transducer plays an integral role in the imaging

capability of the inspection. Due to the double curvature of the surface, linear arrays are not ideal for inspections of this type. However, the ability of 2D arrays to focus through doubly curved surfaces presents an opportunity for improving the detection and characterisation of defects within complex-shaped components.

1.4 Aims & objectives

The aim of the current work is to improve FMC-based inspections for volumetric defect imaging through complex surfaces using 2D phased arrays. A sparse 2D array is used due to its ability to suppress prominent grating lobes while maintaining a high imaging resolution when compared to a matrix 2D array of a similar number of elements; this is a result of the larger aperture of a sparse 2D array which is made possible as the pitch is not constrained by the Nyquist criterion. The captured time-domain data is processed using TFM imaging to produce fully focused images of the interior of specimens. Initially, imaging is conducted on a simple, planar surface in contact and immersion setups to quantitatively illustrate the benefits of using a sparse 2D array. A test specimen with a doubly curved surface is then imaged, whereby the surface profile is assumed unknown and a surface compensation method is required. A scanned array system is then considered, whereby a large specimen is imaged using multiple data sets collected at different locations. Two methods will be introduced to combine the data sets and ultimately 3D defects will be detected and characterised through a large, complex surface. The current work provides the groundwork for 3D TFM imaging of specimens without prior surface knowledge using a 2D array, and demonstrates the benefits for their uptake in industry for improved UT inspections.

1.4.1 Thesis outline

Chapter 2 introduces 3D TFM imaging through a planar surface utilising linear, matrix 2D and sparse 2D arrays. Imaging methods in both contact and immersion are compared and the imaging capabilities of each type of array are compared using experimental data.

In chapter 3, a method of imaging through a complex, non-planar surface from a single array position is introduced. A novel 3D surface extraction algorithm is introduced and validated against the true surface before the positioning of defects is investigated. Computational processing speed is also examined here and a method for increasing 3D TFM imaging speeds is described.

Chapter 4 expands on the previous chapter and introduces a scanned array system for volumetric imaging through a doubly curved surface. The surface profile is extracted and subsequently used for the positioning of defects at a range of depths and positions.

Chapter 5 furthers the results of chapter 4 by proposing a new technique for combining individual TFM images obtained from a scanned array inspection. This is achieved through the generation of sensitivity images, which are used to normalise TFM images depending on the array imaging performance for specific array locations.

Chapter 6 considers the challenge of characterising defects using volumetric defect information. A range of defects are imaged using a scanned array inspection and their orientations determined before being compared to their true values.

Chapter 7 summarises the key findings of the current work and discusses potential avenues for future work.

Chapter 2

Imaging through a planar surface

Specimens with a planar surface profile are the simplest to image through due to the continuity of the surface. When considering a direct contact inspection setup using an array with a flat footprint, i.e. all of the elements are in a single plane, the active region of the array and the surface of the specimen are complementary and imaging is straightforward using a thin layer of couplant. In this case, the complexity of calculations required to produce an internal image is low due to all of the ultrasonic rays travelling in a single medium. In cases where contact inspection is not possible, for example in corrosive or hostile environments [25], or if elevated temperatures prevent the array from being close to the surface [26], a waveguide could be used to facilitate the transmission of ultrasonic energy into the specimen. The inclusion of this intermediate layer adds a level of complexity to the imaging process as the pulse no longer travels at a constant speed and refraction effects must be accounted for. Additionally, non-contact systems involving laser ultrasonics [27] and electromagnetic acoustic transducers (EMATs) [28] could be implemented. Direct coupling with the surface is not necessary using these methods, where transduction is achieved using light and magnetic fields respectively.

Linear arrays are commonly used in industry for ultrasonic inspections, while 2D arrays have not yet been fully implemented. 2D imaging using a linear array is a relatively simple process and can give inspectors an estimation of artefact positions within a specimen, along with allowing post-processing defect characterisation and model validation. 2D images are routinely used in academia and industry because of their ease of implementation, however a more detailed picture can be obtained by employing 2D arrays. This chapter investigates the 3D volumetric imaging capabilities

of the three types of ultrasonic arrays described in the introduction: linear 1D, matrix 2D and sparse 2D. The imaging performance of each array is investigated and compared by imaging machined defects in a test specimen with a planar surface. The imaging process is described for contact and immersion setups using the TFM algorithm. A linear array is used as a comparison of the imaging capabilities of 1D and 2D arrays, while the matrix and sparse 2D arrays are used to compare the effect of element layout on imaging performance. It is worth noting that all array types used here have flat footprints, however arrays with curved footprints are commonly found in industry to perform inspections of pipes.

2.1 Inspection in contact

When conducting a contact inspection, the active region of the array is placed directly on the surface of the specimen. This setup maximises the transmission of energy as the flat footprint of the array and the planar surface are in close contact, while an added layer of gel couplant on the interface eliminates the presence of any trapped air. As the couplant layer is very thin, any effect it has on ray refraction is assumed negligible and so only the properties of a single medium need to be considered. This simplifies the imaging process as a relatively small number of calculations are required when compared to imaging in immersion. An 2D illustration of the ray path an ultrasonic pulse takes while travelling from a transmitting element, T, at $\mathbf{E}_T$ to an image point at $\mathbf{P}$ to a receiving element, R, at $\mathbf{E}_R$ in a contact setup is shown in Fig. 2.1, where bold letters represent position vectors. A 2D system is illustrated for clarity, however it is representative of a 3D system. When considering 3D space, the image point is referred to as a voxel.

When performing TFM imaging, the time taken, τ, for sound, travelling at velocity v, to traverse the journey from $\mathbf{E}_T$ to $\mathbf{P}$ to $\mathbf{E}_R$, termed the time-of-flight (ToF), is required to obtain the amplitude of the signal at $\mathbf{P}$. The amplitude of each element-pair contribution at $\mathbf{P}$ is summed to obtain the final intensity, $I(\mathbf{P})$, and it follows that the process is repeated for each voxel and element-pair. This is described mathematically as:

$$I(\mathbf{P}) = \left| \sum_T \sum_R a_{T,R}\, h_{T,R}\left(\frac{||\mathbf{E}_T - \mathbf{P}|| + ||\mathbf{E}_R - \mathbf{P}||}{v} \right) \right|, \tag{2.1}$$

where $a_{T,R}$ denotes an optional apodisation term which is unused in this work, hence $a_{T,R} = 1$, and $h_{T,R}(\tau)$ represents the complex analytic signal of the A-scan corresponding

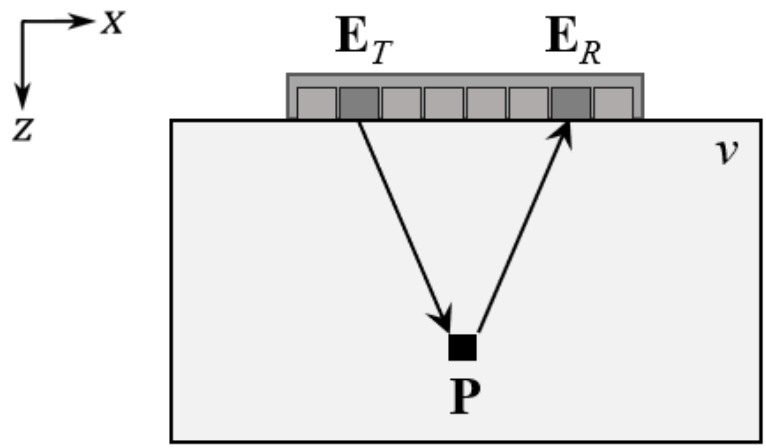

FIGURE 2.1. 2D illustration of a contact inspection setup showing a ray path travelling from $\mathbf{E}_T$ to $\mathbf{P}$ to $\mathbf{E}_R$, which represent the position vectors of the transmitting element, image point and receiving element respectively. v is the velocity of sound in the material.

to transmitting from T and receiving on R, obtained using the Hilbert transform and filtered using a Gaussian window function centred at the array centre frequency, f_c with a -40 dB half bandwidth of 90% of f_c. These filter specifications were chosen to include as much useful information as possible without rendering the signal too noisy. Lanczos interpolation [29] of $h_{T,R}(\tau)$ using a kernel size of 3 is utilised to sample from the discrete time domain signal and ||.|| denotes the Euclidean norm of a vector. If v is not known, it can be calculated using pulse-echo A-scans and knowledge of the specimen thickness, or by using a calibration block. In this chapter, v was measured using the former method and a value of 6300 m/s is used for all TFM calculations.

An illustration of the contact inspection setup used is shown in Fig. 2.2(a). In this case, the test specimen is an aluminium cube of side 50 mm with 13 flat bottom holes (FBHs) of 2 mm diameter that are drilled to different depths in the shape of the letter A. Fig. 2.2(b) provides a $(x-y)$ plane showing a more detailed description of the FBHs.

2.1.1 Linear array

A description of the 5 MHz linear array used in this experiment is given in Table 1.1. The geometric properties of the element layout in this type of array results in the generation of only 2D image planes from a single array position. Therefore, in order to obtain a 3D

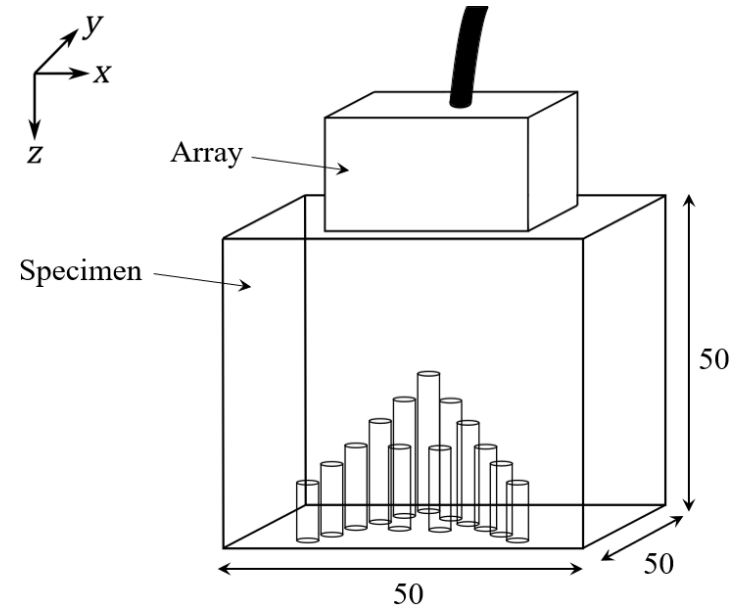

(a)

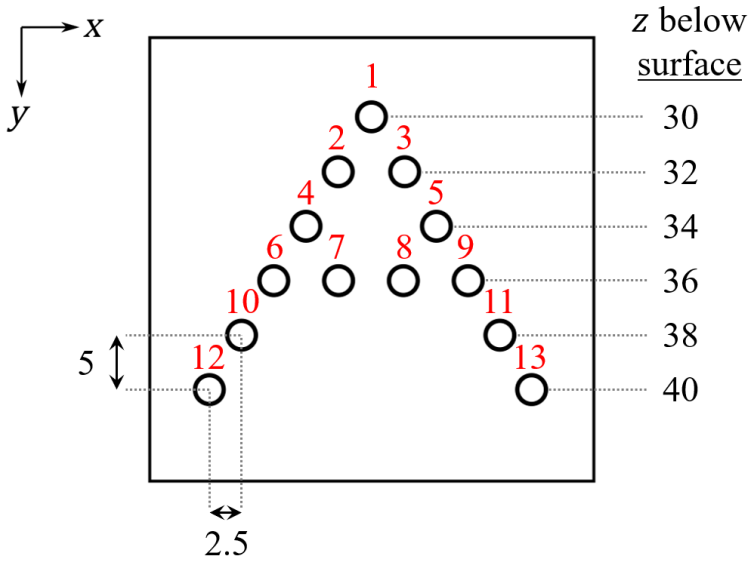

(b)

FIGURE 2.2. Contact inspection setup for imaging through a planar surface. (a) Illustrates the experimental setup, where the aluminium specimen has 13 FBHs of 2 mm diameter arranged in the shape of the letter *A*, and (b) details the FBH locations. The FBHs are labelled 1–13 and the depth of each x row beneath the surface is given on the right hand side. Units in mm.

volumetric image, a pseudo-3D TFM method has to be implemented to combine multiple 2D TFM image frames together, as illustrated in Fig. 2.3. Using this method, the array is translated in the y direction and a data set is collected at a predefined number of positions. Each data set is then processed individually using Eq. (2.1) and the final 3D image consists of the stacked 2D TFM images. This method has the drawback of the lack of resolution in the y direction due to the 2D imaging plane of a linear array. A consequence of this is that any artefact imaged in the y dimension is collapsed to 2D during processing and appears elongated in the final 3D image. This results in an erroneous picture of the internal nature of the specimen. It is important to note that the data sets were filtered at 3 MHz to match the centre frequency of both 2D arrays.

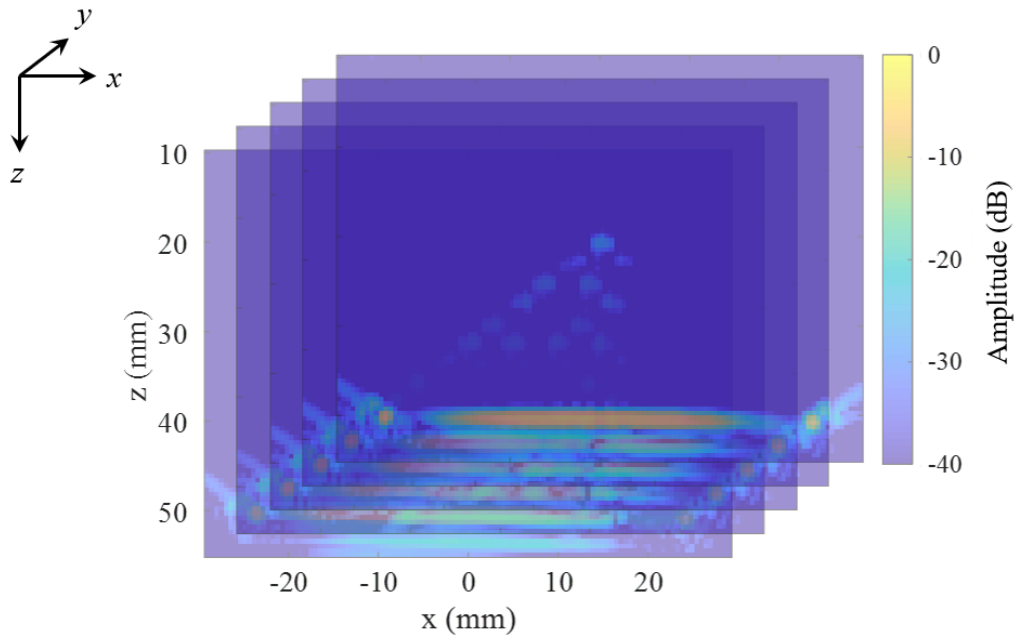

FIGURE 2.3. Example of 5 individual 2D TFM images taken at different y locations using a linear array. The images can be combined to form a pseudo-3D volumetric TFM image.

When experimentally imaging the specimen described in Fig. 2.2, the array was scanned in the y direction in increments of 1.5 mm, for a total of 26 individual array positions. This provided a 90% element overlap and is comparable to the element spacing in the 2D arrays. A HMC data set was captured at each array position, resulting in a total of 26 data sets being required to image the volume of the specimen. Each data set was processed individually using Eq. (2.1) where only the (x,z) components of the position vectors were used. The resulting 26 linear 2D TFM images were then

stacked in a 3D matrix at 1.5 mm intervals to represent the 3D volume inspected. The maximum amplitude across all back wall indications was then used to normalise the 3D matrix. The result is shown in Fig. 2.4 plotted on log scale as multiple isosurfaces at different amplitude levels. The plotting of 3D data sets can be challenging; in the current work, MATLAB's isosurface function was used to visualise the 3D matrix of amplitudes (which corresponds to the 3D TFM image). To aid with visualisation the isosurfaces are plotted with decreasing levels of transparency relative to the maximum amplitude, which is plotted as opaque. The corresponding colour of each isosurface is given in the legend, however in the presence of an underlying darker contour, the overlying contour colour may be distorted. The z axis has been reduced to exclude the back wall for visual purposes.

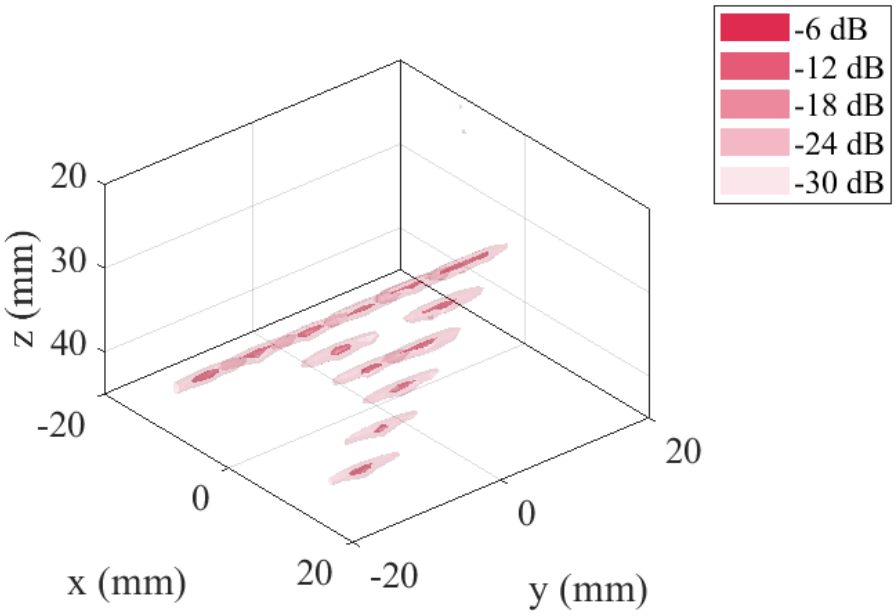

FIGURE 2.4. Contact pseudo-3D volumetric TFM image of the A block using a linear array translated in the y direction and plotted as multiple isosurfaces at different amplitude levels. The dB scale is relative to the amplitude of the largest indication from the back wall (not shown).

2.1.2 Matrix 2D array

As was mentioned in section 1.1.2, 2D arrays have their elements dispersed over a 2D aperture and therefore are able to resolve in both lateral directions. A significant consequence of this ability is that a 3D volume can be inspected from a single array location,

eliminating the need to combine multiple 2D TFM images. The 3D TFM algorithm can be directly applied to generate the final image using a single data set.

A 3 MHz matrix 2D array described by parameters in Table 1.1 was placed centrally on the surface of the A block specimen and a single data set was captured. Eq. (2.1) was implemented using the (x, y, z) components of the position vectors and the result is shown in Fig. 2.5 as isosurfaces plotted at different dB levels relative to the maximum amplitude in the back wall.

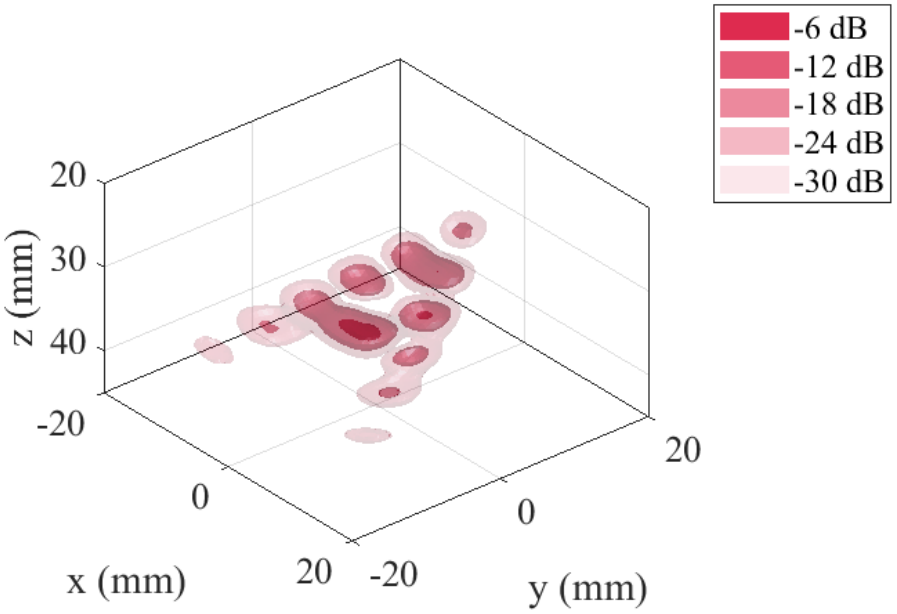

FIGURE 2.5. Contact 3D TFM image of the A block using a matrix 2D array plotted as multiple isosurfaces of different amplitudes. The dB scale is relative to the maximum amplitude in the back wall (not shown).

2.1.3 Sparse 2D array

The final type of array used is a 3 MHz sparse 2D array, a full description of which is also given in Table 1.1. As was the case for the matrix array, a 3D volume can be inspected from a single location with this array. The active region was placed centrally on the surface of the specimen and a data set was collected and processed the same as in the previous section. The resulting 3D TFM image is shown in Fig. 2.6 as isosurfaces plotted at different dB levels relative to the maximum amplitude in the back wall.

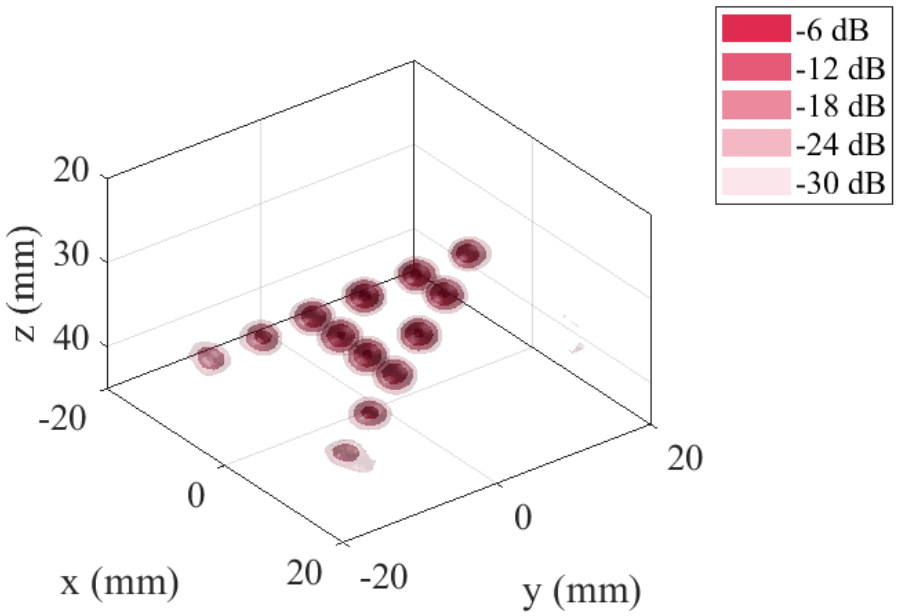

FIGURE 2.6. Contact 3D TFM image of the *A* block using a sparse 2D array plotted as multiple isosurfaces of different amplitudes. The dB scale is relative to the maximum amplitude in the back wall (not shown).

2.1.4 Discussion

From visual comparison of $(x-z)$ elevations of the 3D TFM images, shown in Fig. 2.7, it is clear that the choice of array has an impact on the resulting image. Due to the combination of multiple individual 2D TFM images when imaging with the linear array, the FBHs in Fig. 2.7(a) have been elongated and determining the true nature of the defect is not possible without further scans. From the images alone it is not clear whether the defects are FBHs or notches. A potential solution could be to take another scan of the specimen but with the linear array rotated 90°, thereby scanning the specimen along the x axis. Combination of the two pseudo-3D TFM images could result in a more accurate understanding of the defects. However, this would yield a large volume of data and an increase in both scanning and processing times. The result of imaging using the matrix array visually illustrates the ability of a 2D array to focus in multiple directions as the FBHs appear circular. Although the isosurfaces representing the amplitudes of FBHs 2 and 3 and those of 3, 6 and 8 have merged into two blobs, it is evident to an observer that the defects are bottom-drilled holes and not notches or side drilled holes as they do not extend along the x or y directions and can be approximated as circular. The merged indications is a result of the element layout of the matrix array not having the ability to distinguish defects that are separated by less than 5 mm in the current specimen. By comparison, using the sparse 2D array with an optimised element layout, Fig. 2.7(c) shows well-focused circular defects. Visual comparison of Fig. 2.7(b) and Fig. 2.7(c) qualitatively demonstrates the benefits of using a sparse array over a matrix array.

Quantitative verification can be obtained by measuring the spatial size of each defect; this can be achieved by measuring the volume, $V_{\text{-6 dB}}$, within which the defect response is greater than 6 dB less than the maximum peak of each response. $V_{\text{-6 dB}}$ is calculated by multiplying the number of voxels which satisfy this condition by the volume of a single voxel. 6 dB below the maximum corresponds to 50% of the maximum amplitude signal and is commonly used in ultrasonic imaging as a sizing technique [30]. Fig. 2.8 shows the calculated values for each defect and array. Values for FBHs 2, 3, 6, 7 and 8 using the matrix array case have been excluded as their indications cannot be resolved. From Fig. 2.8, the sparse array has the lowest $V_{\text{-6 dB}}$ for most defects, indicating a well-focused defect. On the other hand, the matrix array has larger values, confirming the inability of this array to tightly focus the ultrasound beam. The linear array has comparatively lower $V_{\text{-6 dB}}$ values than the matrix array, even though the FBHs appear elongated in the TFM image. A problem with this method of comparison is

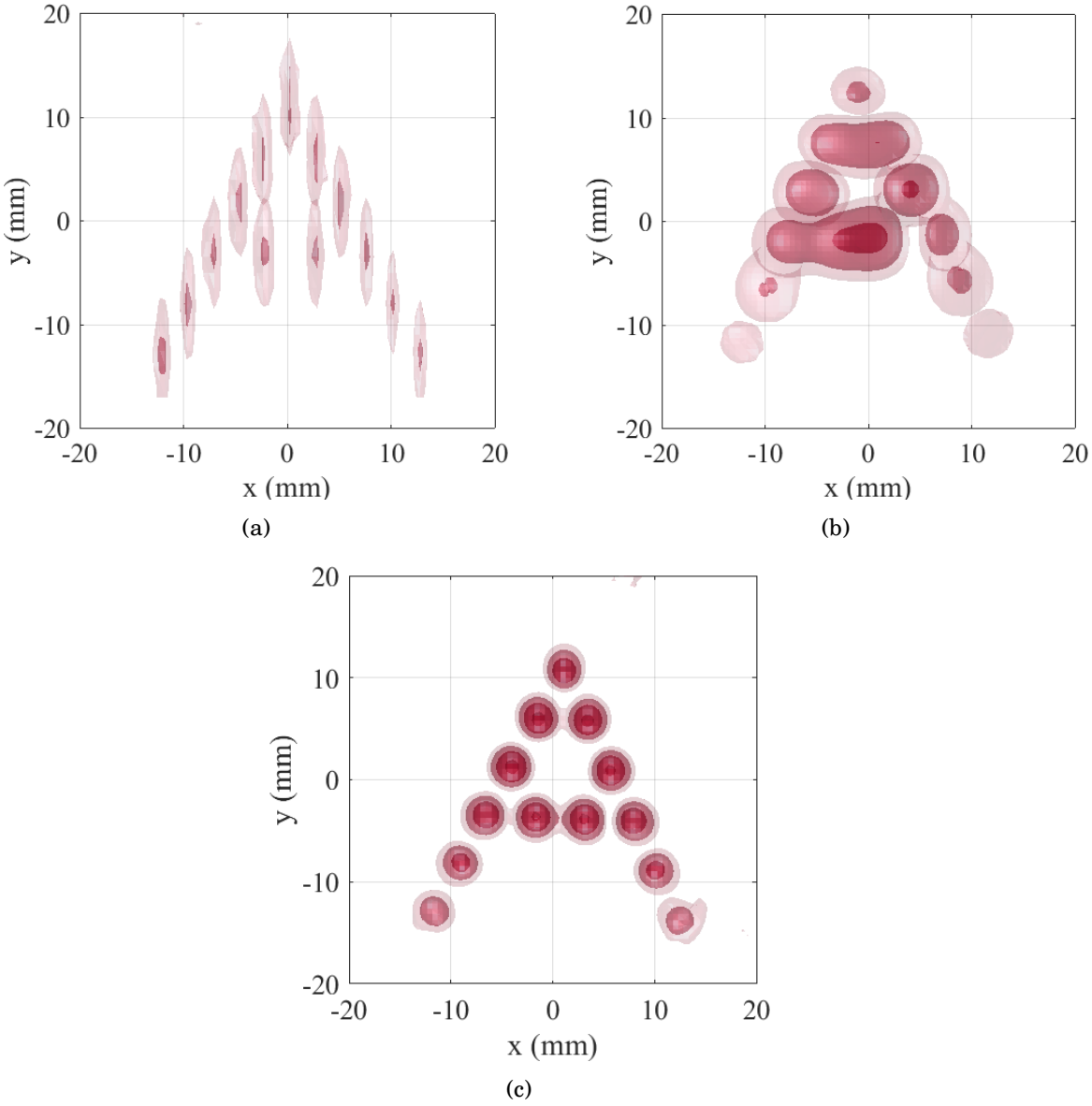

FIGURE 2.7. $(x-z)$ elevation views of the contact 3D TFM images in (a) Fig. 2.4 using a linear array, (b) Fig. 2.5 using a matrix array and (c) Fig. 2.6 using a sparse array. Each image is plotted at multiple isosurfaces relative to their local maximum in the back wall.

the assumption that the defects are point-like reflectors. The defect indications using the 2D arrays are circular and therefore assuming they are point-like is acceptable, however, defect indications which are not point-like can result in an underestimation of $V_{\text{-6 dB}}$ and is likely the cause of the linear array having lower than expected values. The reason for this is that the amplitude of a notch is spread out along one direction, while the response

from a point has a narrow amplitude spread, as illustrated in the zoomed in regions around FBH 13 in Fig. 2.9. Additionally, the resolution in the y direction using the linear array is limited by the translation of the array between scans, which in this case was 1.5 mm, leading to 21 voxels in Fig. 2.9(a) exceeding the amplitude threshold, while 73 voxels satisfy the condition in Fig. 2.9(b) when imaged using the sparse array with a grid spacing of $\lambda/4 = 0.53$ mm in all x, y, z directions, where λ is the wavelength of sound in the specimen. It is for this reason that $V_{\text{-6 dB}}$ is not an accurate measure parameter for the results using the linear array, however the results do illustrate the benefits of imaging with a sparse array over a matrix or linear array.

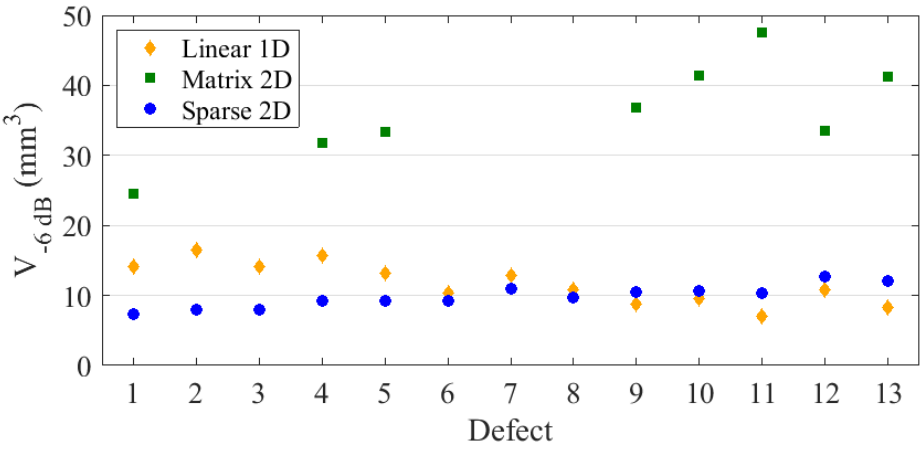

FIGURE 2.8. $V_{\text{-6 dB}}$ values obtained from 3D TFM images generated using different arrays in contact.

The signal-to-noise ratio (SNR) was also used as an additional comparison measure. The SNR reflects the overall image quality by looking at the relationship between the defect signal strength and the amplitude level in a defect-free region of the image. There are two main categories of noise that negatively affect ultrasonic imaging: coherent and incoherent [31]. An incoherent noise source in this setup is random electrical noise from the array controller; the effect of this is minimised by averaging the signals on collection. Coherent noise sources are intrinsic to the inspection and their effect can not be reduced by averaging. Common causes include backscatter from grain boundaries in the microstructure and artefacts due to multiple reflections, mode conversion or diffraction from sharp corners. When imaging with the sparse array, an additional source of coherent noise is a direct result of the non-periodic element spacing; as was mentioned in section 1.1, the non-periodic spacing of elements disperses the energy of would-be grating lobes into specimen. In this contact setup, there has been

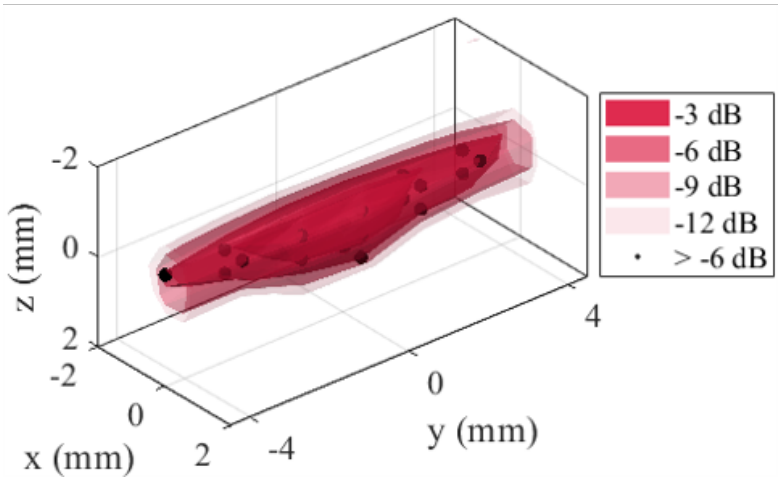

(a)

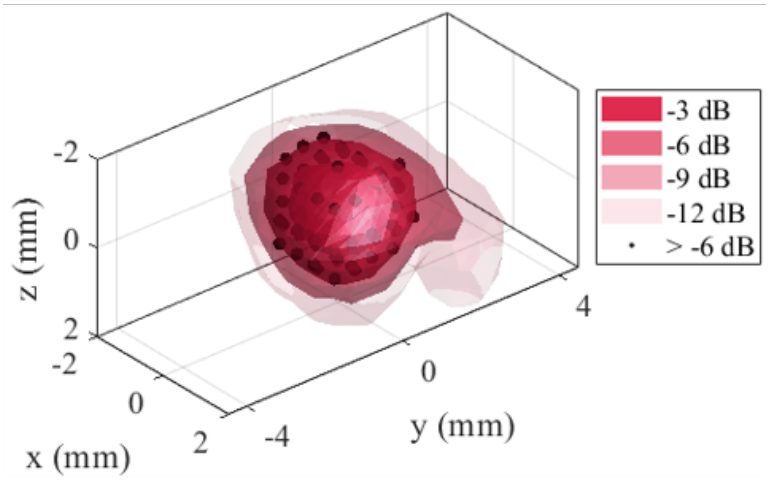

(b)

FIGURE 2.9. Zoomed in windows around FBH 13 using (a) the linear array, and (b) the sparse array. Each defect is centered on the point of maximum amplitude and dB levels are relative to maximum defect amplitude. The black dots mark voxels that have amplitudes greater than 6 dB below the maximum defect amplitude.

no mode conversion and hence it does not contribute to the background noise. However, as the specimen is a cuboid with a side length of 50 mm, background noise sources are backscatter from grain boundaries, multiple reflections and diffraction from the corners. In this case a λ^3 defect-free region between the surface, or front wall, and FBH 1 was selected in the specimen to calculate the average background noise. The formula for

calculating the SNR is given by:

$$\text{SNR} = 20 \cdot \log\left(\frac{I_{max}}{I_{average}}\right) \tag{2.2}$$

where I_{max} is the maximum amplitude of a defect and $I_{average}$ is the average background noise. The SNR for each defect and array is shown in Fig. 2.10, where again some defects imaged using the matrix array have been excluded. The figure shows that all defects are able to be imaged with acceptable SNR levels. The SNRs for defects imaged with the 2D arrays begin to decrease past defect 8, whereas the values remain relatively constant for the linear array. This is a result of the element layouts; the line sources in the linear array transmit sound that is more directional along the z axis when compared to the square or circular elements in the 2D arrays. Fig. 2.11 shows the average SNR against defect depth. Although the defect responses are highest using the matrix array, the inherent properties of the array make obtaining high resolution defect images impossible.

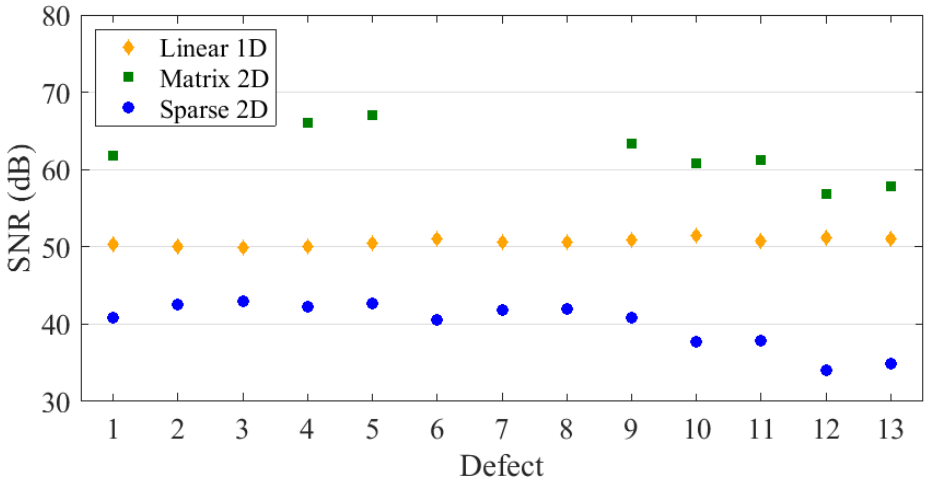

FIGURE 2.10. SNR of FBHs for each type of array.

Data size is an important concern when comparing arrays for a volumetric inspection. Imaging with the 128-element linear array required 26 data sets to be captured and processed individually before being combined in a final stage. Even with using HMC instead FMC, a total of 350 MB of data was collected, compared to 14 MB and 15 MB for the 121-element matrix array and 128-element sparse array respectively. Although the number of elements in each array is similar, the linear array scan required a significant amount more computer memory. Processing speed is also an important factor of any inspection process. Table 2.1 shows the time taken to process the data sets for each array using MATLAB; the desktop computer used in the current work contains

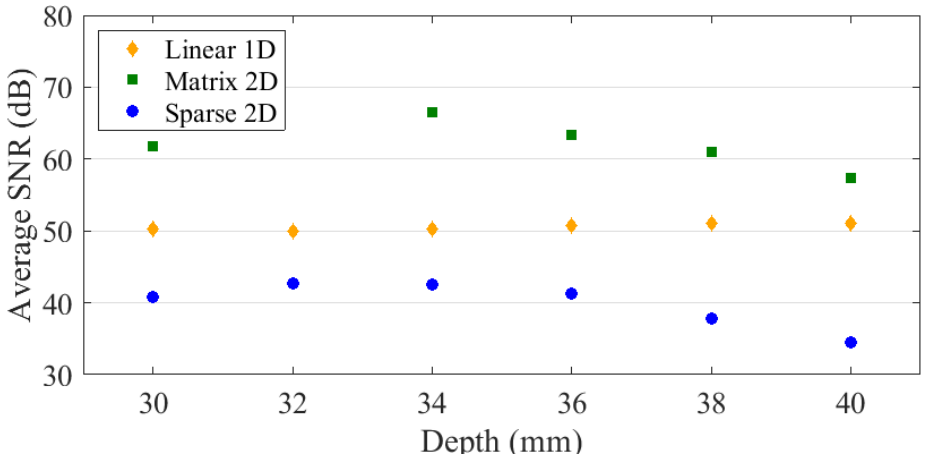

FIGURE 2.11. Average SNR of FBHs for each type of array at increasing depth.

an Intel Core i7-6700 3.4 GHz quad-core processor, 32 GB RAM and Nvidia GeForce GTX Titan X graphics card. The table shows that the linear array was quickest while both 2D arrays take similar times to complete. In all imaging cases, the data sets were filtered to 3 MHz and the imaging grid resolution for both 2D arrays was $\lambda/4$. The resolution in the y direction using a linear array was limited by the translation of the array to 1.5 mm, while a resolution of $\lambda/4$ was used in both x and z directions.

After comparing the imaging capabilities of linear, matrix and sparse arrays in a contact setup, it has been demonstrated that the sparse array outperforms the others. Although the SNR decreases with increasing z depth in the specimen beyond 34 mm, the associated $V_{\text{-6 dB}}$ values and visual images showed well-focused and easily distinguished defects. The matrix array underperformed when compared to the other array types, however it did image defects with the highest SNR and was able to discern the shape of the FBHs while the linear array could not. The linear array is able to focus well in each $(x-z)$ plane, as evidenced by a consistently high SNR across all defects, but the inability to resolve in the y dimension and large amount of memory required to store the data makes volumetric imaging with this type of array challenging.

2.2 Inspection in immersion

In many scenarios in industry, contact inspections are not possible and an alternative coupling method is required to obtain information about a specimen. Effective coupling is important as any mismatch between the footprint of the array and the surface of

TABLE 2.1. Processing times for contact 3D TFM using different arrays.

	Linear 1D	Matrix 2D	Sparse 2D
Number of scans	26	1	1
Number of voxels	26 x 6700	516,000	516,000
Processing time			
Single frame (s)	4.4	340	380
Total (s)	115	340	380

the component results in a loss of inspection performance due to the large impedance mismatch between air and the specimen material [32]. This can result in most of the ultrasound being reflected at the surface and not transmitted. To avoid a large impedance mismatch, the component under inspection can be immersed in water, which has an acoustic impedance roughly 3,500 times higher than that of air, and so the water acts as an acoustic couplant between the array and the component. If the specimen is too large to be moved or the inspection is being conducted *in situ*, it is possible to attach either a water-filled jacket to the outer circumference of the pipe with an array located inside, or a water jet coupled system [33]. It is worth noting that immersion inspections are not only carried out when contact with the specimen surface is not possible; the generation of different wave modes, such as shear and Rayleigh waves, typically requires an interface between water and the specimen material [34]. With the introduction of another medium, care must be taken while calculating the ray paths between elements and image points within the specimen while correctly compensating for two acoustic velocities. This is necessary in order to query the associated A-scan for element pairs at the correct time for the TFM algorithm. Therefore, for the case of a specimen with a planar surface parallel to the footprint of the array, the distance between the array and surface of the specimen must be known.

3D volumetric imaging in immersion through a planar surface using the same three arrays used previously in this chapter is investigated using the setup illustrated in Fig. 2.12. The base of each array was placed flat on the surface of the specimen described in Fig. 2.2 before being moved using a computer controlled scanning frame to a standoff distance above the surface of approximately 20 mm, which will be referred to in future as the ‘set standoff’. For accuracy, the acoustic velocities of sound in water and the specimen were experimentally measured by examining A-scans and only longitudinal waves are considered; the velocity of sound in the specimen was taken as the same value as previously mentioned, 6300 m/s, while the velocity of sound in water was measured

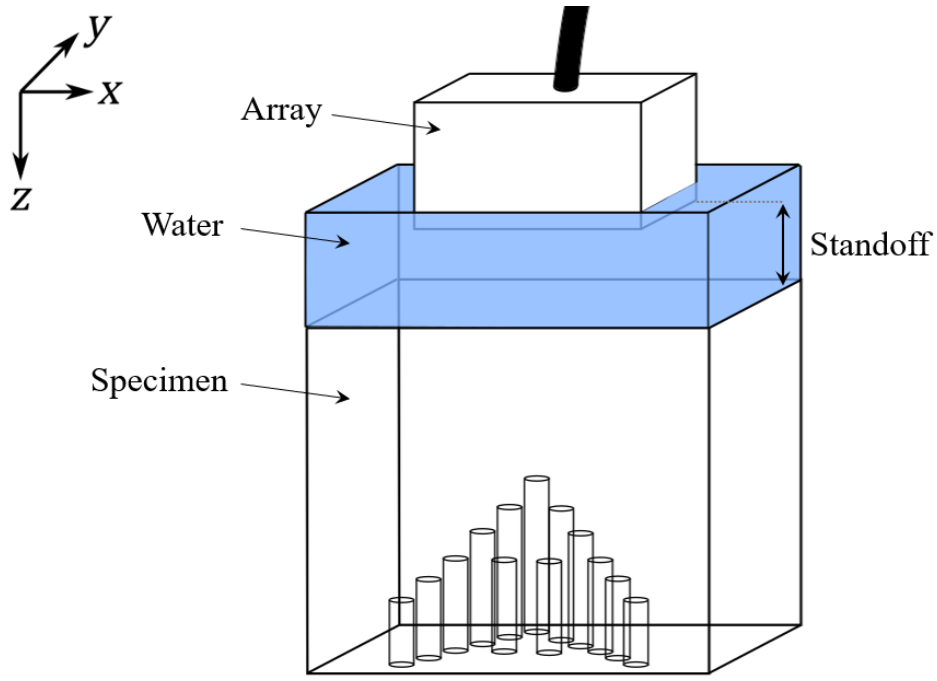

FIGURE 2.12. Illustration of experimental setup for immersion inspection through a planar surface.

using pulse-echo A-scans to be 1470 m/s.

2.2.1 Surface measurement and compensation

Measuring the standoff distance of a planar surface is simple once the couplant velocity is known. In an immersion setup, the largest amplitude in a pulse-echo A-scan, after the ringdown period, typically corresponds to the reflection from the surface of the specimen and the time this occurs, t, is easily determined from the peak of the envelope. Using the velocity of sound in water, v_1, the standoff distance for each element is calculated using:

$$\text{standoff} = \frac{1}{2} v_1 t \tag{2.3}$$

where the factor of one half is required as t corresponds to the time taken to travel the return path between the element and surface. The mean of all standoff values is taken as the estimated standoff distance.

The easiest method of integrating a surface into the imaging process is to describe it as a series of discretised points. Alternatively, it could be described as an

equation as in [35], but that is not considered in the current work. When imaging with a linear array, the surface profile only needs to be represented by a 2D line of (x,z) points for each array position. For this case, x is defined over a distance equal to the length of the array and aligned with the central element. The x spacing of surface points is set as $\lambda_1/2$, where λ_1 is the wavelength of sound in water and was calculated to be 0.49 mm. The z coordinate of each surface point is set equal to the estimated standoff value. When imaging with a 2D array, a 3D point cloud is required, where the lengths of x and y are defined as 1.5 times the diameter of the array and spaced using a resolution of $\lambda_1/2$; the x and y lengths were arbitrarily chosen to encompass a large volume without significantly impacting the image processing speed. The z value of each (x,y) point was set to the estimated standoff distance.

Once the surface profile has been discretised, the next stage is to determine the path an ultrasonic pulse traverses between an element pair and voxel in the imaging grid. This process was simple in the contact case, but more complex in immersion. For a pair of elements and image point within the specimen, the associated surface crossing points need to be accurately determined to ensure the correct amplitudes are being summed. A 2D illustration of such a ray path is shown in Fig. 2.13, where $\mathbf{A}_T$ and $\mathbf{A}_R$ represent the position vectors of the surface-crossing points on the transmit and receive paths respectively, v_2 is the acoustic velocity in the specimen material and the remaining symbols have been defined previously. The process of determining the locations of $\mathbf{A}_T$ and $\mathbf{A}_R$ is as follows. Firstly, trigonometry is used to calculate the times for a pulse in water to travel from $\mathbf{E}_T$ to all of the surface points and the values are stored in an array. Then the times taken for the pulse to travel from all surface points to the voxel in the specimen are calculated and stored in the same array. The two times associated with each surface point are then summed to give the total travel time for a pulse to travel from $\mathbf{E}_T$ to $\mathbf{P}$ through the surface. Fermat's principle of least time [36], which states that path taken by a ray between two points is the path that can be travelled in the least amount of time, is then used to determine the surface-crossing point. It is the surface point that yields the absolute minimum time that is taken as $\mathbf{A}_T$ [37]. The process is then repeated for $\mathbf{E}_R$ and $\mathbf{P}$ to find the location of $\mathbf{A}_R$. The time taken to traverse the journey from $\mathbf{E}_T$ to $\mathbf{A}_R$ via $\mathbf{A}_T$, $\mathbf{A}_R$ and $\mathbf{P}$ is then used in the adjusted TFM algorithm given by:

$$I(\mathbf{P}) = \left| \sum_T \sum_R a_{T,R}\, h_{T,R} \left(\frac{||\mathbf{E}_T - \mathbf{A}_T||}{v_1} + \frac{||\mathbf{A}_T - \mathbf{P}||}{v_2} + \frac{||\mathbf{P} - \mathbf{A}_R||}{v_2} + \frac{||\mathbf{A}_R - \mathbf{E}_R||}{v_1} \right) \right|, \quad (2.4)$$

where Lanczos interpolation is used to query $h_{T,R}(\tau)$ at indiscrete times and $a_{T,R} = 1$.

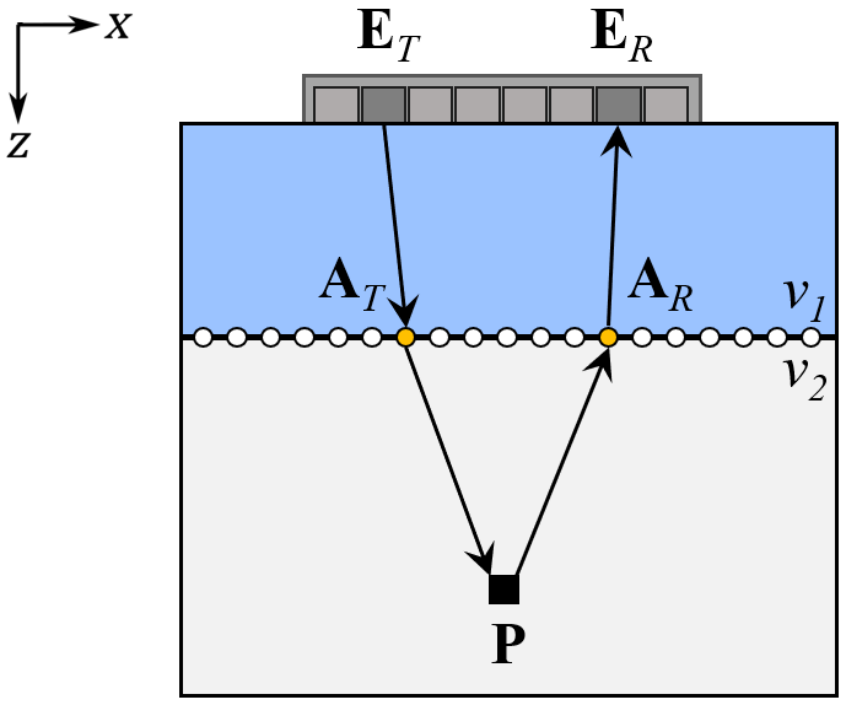

FIGURE 2.13. 2D illustration of the ray paths required for immersion TFM imaging with a discretised surface. $\mathbf{E}_T$, $\mathbf{E}_R$ and $\mathbf{P}$ represent the position vectors of the transmitting element, receiving element and image point respectively. $\mathbf{A}_T$ and $\mathbf{A}_R$ represent the position vectors of the surface-crossing locations. v_1 is the velocity of sound in water, while v_2 is the velocity of sound in the specimen.

2.2.2 Linear array

As was described in the contact case in section 2.1.1, the linear array was translated in 1.5 mm increments and a data set was collected at each position. The pulse-echo A-scans were processed using the method described in the previous section to calculate the estimated standoff for individual array positions. Each data set was processed using its associated estimated standoff distance and the resulting 2D TFM amplitudes were stacked into a 3D matrix to represent a pseudo-3D TFM image, which is shown in Fig. 2.14. The amplitudes shown on a dB scale are normalised to the maximum amplitude across all back wall indications.

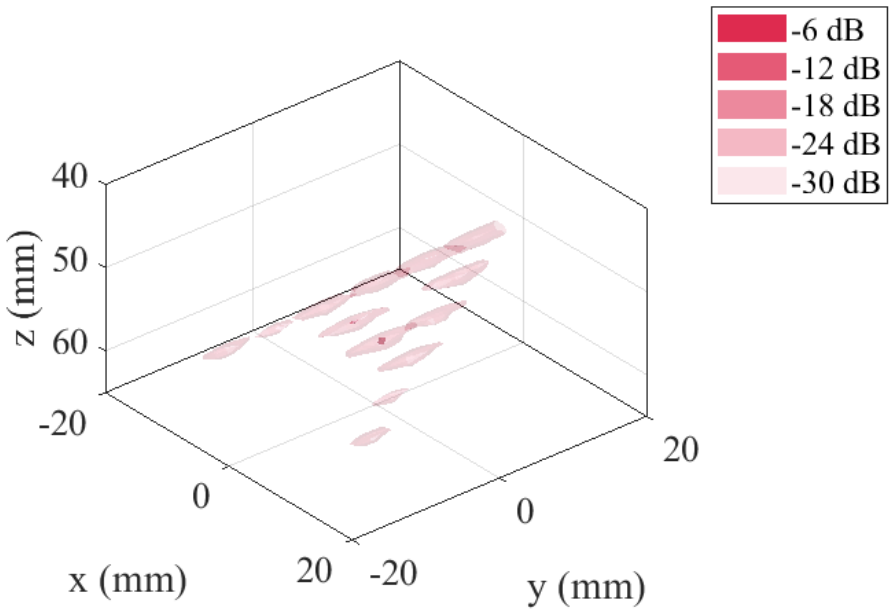

FIGURE 2.14. Immersion pseudo-3D TFM image of the *A* block using a linear array translated in the *y* direction and plotted as multiple isosurfaces at different amplitude levels. The dB scale is relative to the amplitude of the largest indication from the back wall (not shown).

2.2.3 Matrix 2D array

The result of the interior 3D TFM image calculated using in immersion is shown in Fig. 2.15.

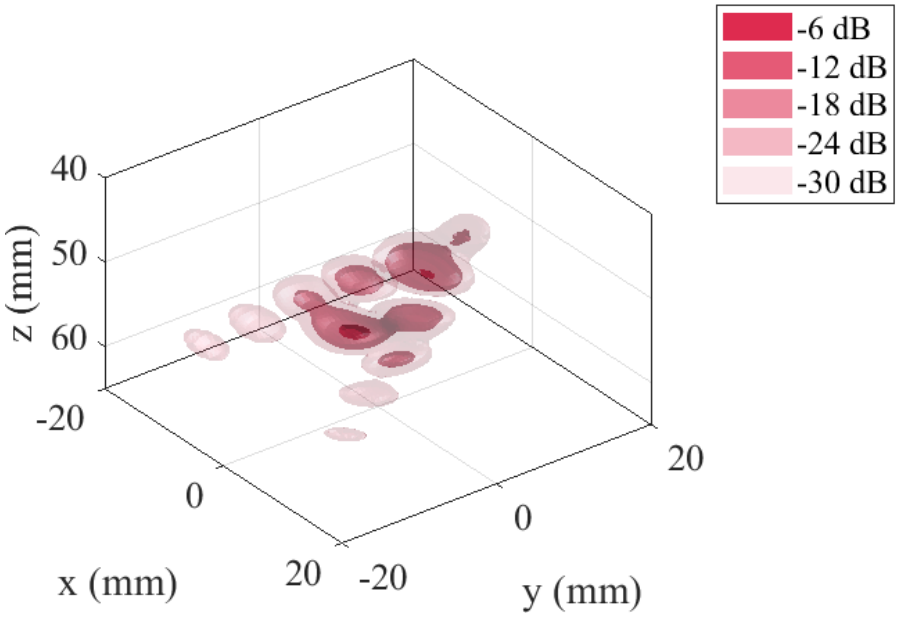

FIGURE 2.15. Immersion 3D TFM image of the *A* block using a matrix 2D array plotted as multiple isosurfaces of different amplitudes. The dB scale is relative to the maximum amplitude in the back wall (not shown).

2.2.4 Sparse 2D array

The 3D method described for discretising the surface profile by default creates a rectangular 2D plane of points. Due to the element layout of the sparse 2D array, it has a circular active region and so calculating the ToFs through each surface point would result in a significant number of unnecessary calculations. However, all surface points are considered here and a method for reducing the number of calculations will be discussed at a later stage. The result of the interior 3D TFM image using the sparse array is shown in Fig. 2.16.

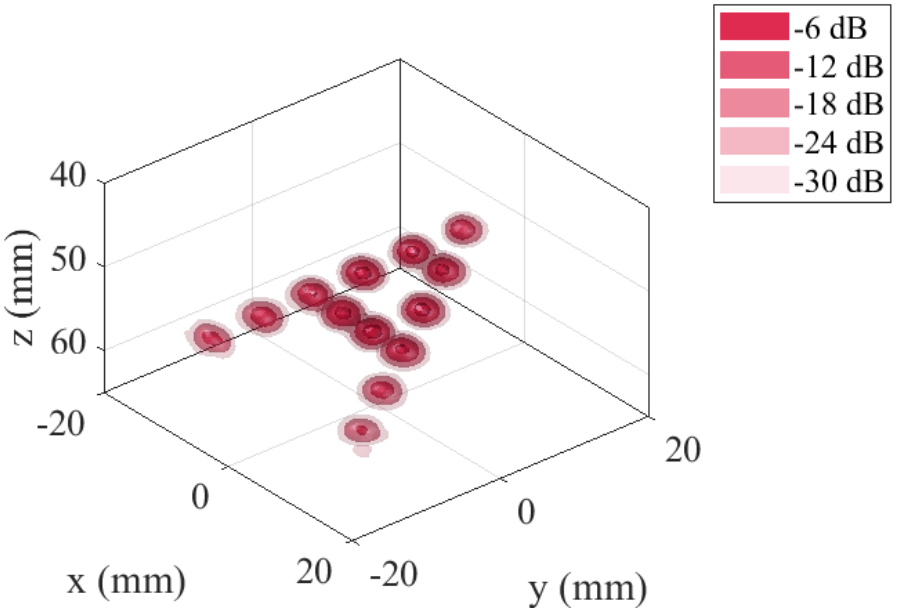

FIGURE 2.16. Immersion 3D TFM image of the *A* block using a sparse 2D array plotted as multiple isosurfaces of different amplitudes. The dB scale is relative to the maximum amplitude in the back wall (not shown).

2.2.5 Discussion

From visual comparison of the $(x-y)$ image elevations in Fig. 2.17, the 3D TFM results appear to follow the same trend as was observed in the contact case, i.e. defects imaged with the linear array are elongated and the sparse array provides best focusing power. This provides confidence that the standoff estimations are correct. The 3D TFM result obtained using the matrix array has the same merging of defect indications that was observed in the contact case, however the defect locations are still easy to distinguish visually.

The imaging performance of each array is then considered by calculating the associated $V_{\text{-6 dB}}$ values. Fig. 2.18 shows the results of this comparison, where the matrix array is not considered as either (a) the maximum defect amplitudes were so small that 6 dB below that value included voxels not corresponding to the defect, or (b) the defect indications had merged with neighbouring defects. As was found in Fig. 2.8, the $V_{\text{-6 dB}}$ values when using the sparse array begin lower than the linear array and then increase as defect depth increases. Defects 9–13 in Fig. 2.18 have a lower $V_{\text{-6 dB}}$ value when imaged using the linear array than the sparse array, which is explained by the elongation of defects and larger grid spacing in the y direction, as was illustrated in Fig. 2.9.

The SNR was also investigated for each defect and array, and the comparison is shown in Fig. 2.19. Due to the presence of water, mode conversion now occurs at the surface of the specimen and contributes to the noise level. The results show that defects imaged with the matrix array have a high SNR, however, as mentioned previously, there is a limited amount of information that can be obtained about the nature of the defects. Defects imaged with the sparse array have a higher SNR than when imaged with the linear array. When disregarding the SNR of defects imaged using the matrix array, the sparse array maintains the highest SNR levels of defects when depth into the specimen increases, as shown by Fig. 2.20.

The results obtained from imaging in immersion mirror the contact case, whereby the sparse array outperforms the other array types. It is difficult to obtain meaningful defect information when using the matrix array, while the lack of ability to focus in the y direction when using the linear array also makes volumetric measurements difficult.

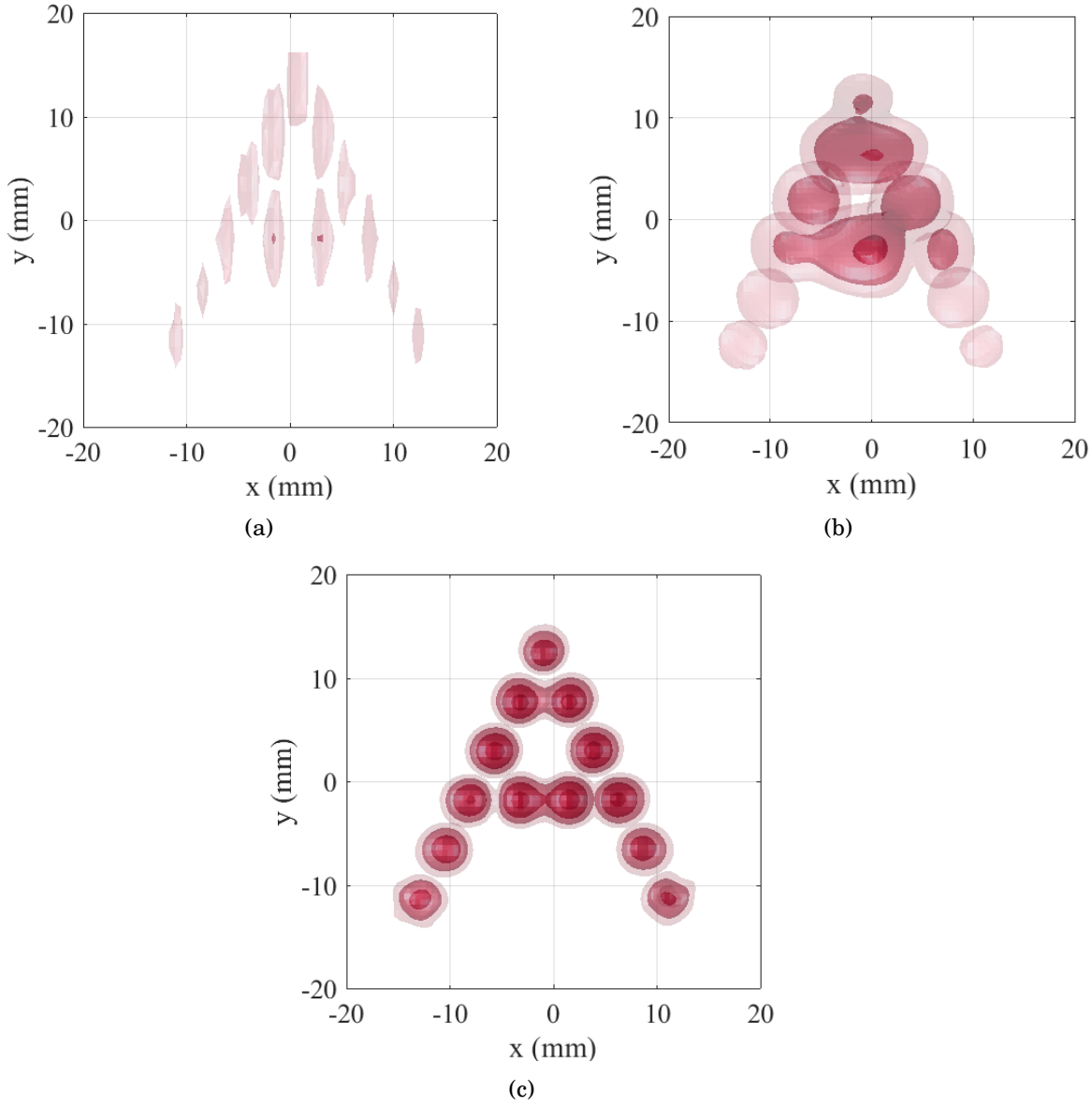

FIGURE 2.17. $(x-z)$ elevation views of the immersion 3D TFM images in (a) Fig. 2.4 using a linear array, (b) Fig. 2.5 using a matrix array and (c) Fig. 2.6 using a sparse array. Each image is plotted at multiple isosurfaces relative to their local maximum in their respective back wall.

With the inclusion of a layer of surface points the total time for the imaging process increases. This is not as noticeable when imaging with the linear array, however processing times using a 2D array drastically increases. A comparison of imaging speeds is given in Table 2.2 where it can be seen that using the same interior grid resolutions as the contact case, the addition of the layer of surface points has a significant impact on

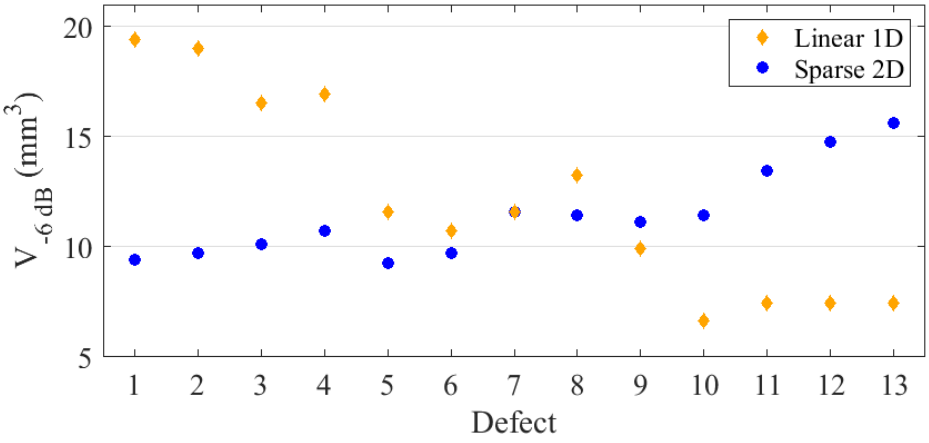

FIGURE 2.18. Comparison of $V_{-6\,dB}$ obtained from 3D TFM images generated using different arrays in immersion.

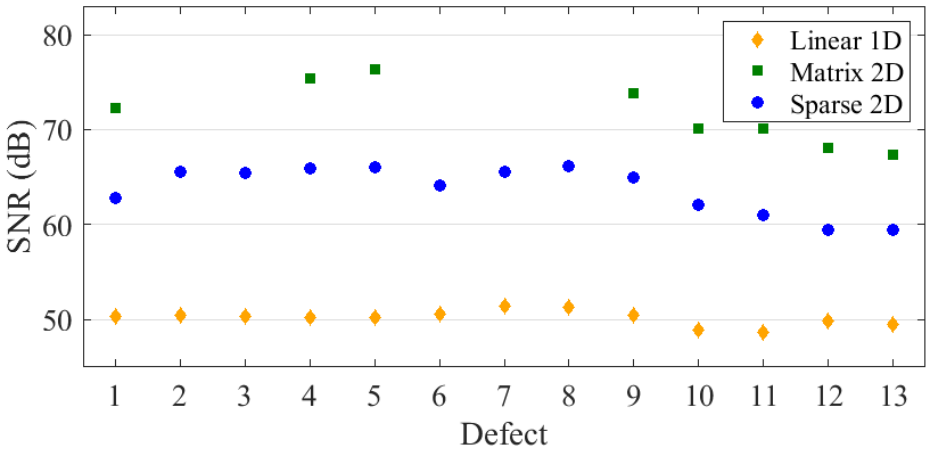

FIGURE 2.19. SNR of FBHs for each type of array in immersion.

overall calculation times. By considering the 2D arrays with equal numbers of surface points and voxels, the addition of 7 more elements in the sparse array equates to 200 extra seconds of processing time. The most significant bottleneck in the computing process is determining the minimum ToFs for element-voxel combinations. An opportunity to speed the process up therefore lies in simultaneously calculating ToF values. Speedup is necessary for producing 3D TFM images in a reasonable time frame for analysis and ultimately for real-time imaging.

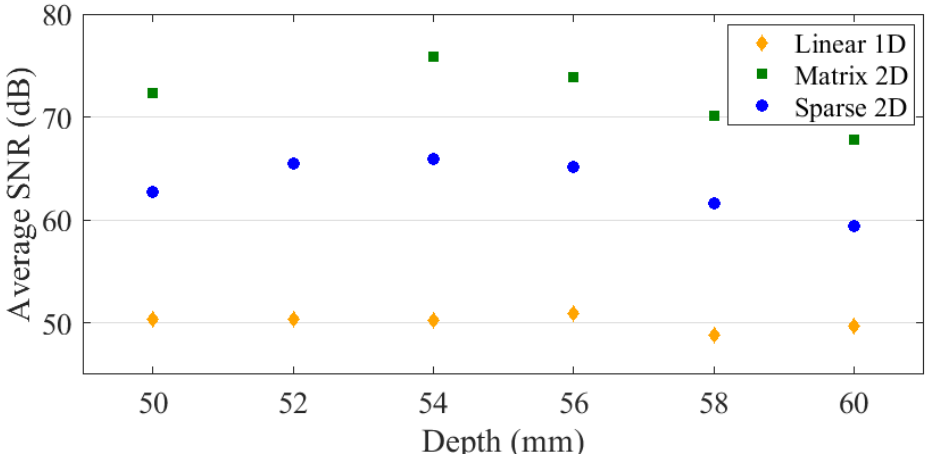

FIGURE 2.20. Average SNR of FBHs for each type of array at increasing depth in immersion.

TABLE 2.2. Processing times for immersion 3D TFM using different arrays.

	Linear 1D	Matrix 2D	Sparse 2D
Number of scans	26	1	1
Number of surface points	26 x 164	27,000	27,000
Number of voxels	26 x 6700	516,000	516,000
Processing time			
Single frame (s)	6.67	3700	3900
Total (s)	173	3700	3900

2.3 Summary

An investigative comparison of using linear and 2D arrays for 3D volumetric imaging has been investigated in this chapter. The results have shown that in order to obtain high quality, accurate images of the inside of a specimen, using a 2D array is optimal due to its ability to focus across two axes. The effect that the element layout in a 2D array has on imaging ability was also investigated; the results confirmed that the sparse array with elements arranged in a Poisson disk formation outperforms the matrix array with elements arranged in a grid. In both contact and immersion setups, the sparse array imaged defects with high SNR and low $V_{\text{-6 dB}}$ values, and will therefore be the only type of array used in the following chapters. Processing speed is a concern when generating 3D images, as ultimately real-time imaging is desirable for inspections. The results have shown that imaging in contact can be conducted in reasonable time frames, but imaging in immersion is significantly slower when using 2D arrays. Linear arrays in immersion provide faster imaging speeds, but at the cost of lower defect resolution and larger data files. When considering 3D imaging with a 2D array it is therefore necessary to optimise the calculations to complete in a reasonable time and a method used to improve imaging speeds will be discussed in the following chapter. Additionally, the surface considered here was planar and parallel to the array, so pulse-echo signals were used to determine the standoff distance. The ability of 2D arrays to focus accurately through non-planar surfaces is highly relevant to industry and is therefore also investigated in the following chapter.

Chapter 3

Imaging through a non-planar surface

In many industrial inspection scenarios, ultrasonic imaging needs to be conducted through surfaces which are non-planar. Components with non-planar geometries are commonly found in modern structures, particularly in the power generation sector where thousands of pipes are interconnected. Pipework branches and pressure vessel nozzles are of particular interest due to the high stress and risk of failure in these regions. If corrections are not made for varying surface profiles, loss of the original focus point can occur and inaccurate TFM images will be obtained [32]. Even minor surface errors can result in a significant loss of final image quality, so it is extremely important that an accurate depiction of the surface profile is obtained.

This chapter introduces a method for extracting a 3D surface profile from a non-planar specimen using a TFM-based imaging method. The discretised surface is then used to generate an internal 3D TFM image. The computational challenges associated with 3D imaging and the use of GPU programming is also discussed.

3.1 Non-planar surface compensation methods

Many factors need to be taken into account when designing the inspection setup for complex surfaces. Firstly, to maximise the transmission of sound energy, close to normal incidence of the sound wave to the surface is desirable. However, for non-planar surfaces this is not always possible and the array may need to be moved or rotated during

inspections and multiple sets of data collected. As was discussed in the previous chapter, coupling between the array and surface profile is crucial for transmission of ultrasonic energy. There are currently three main approaches to tackle this coupling problem.

The first of these involves using a liquid, such as water, to couple a rigid array to the surface of the component under inspection. The liquid acts as an acoustic couplant between the array and the component and the surface profile can be extracted from the ultrasonic data using an imaging algorithm. This is an effective method when there is no previous knowledge of the surface [5, 38, 39]. In a previous study, a 2D array was used to generate 3D images in immersion [40]; however, in this case the test specimen had a planar surface and determining the surface position from the data is straightforward. A similar method to this was used for immersion imaging in the previous chapter.

A second approach involves fitting the array with a wedge that complements the surface geometry [41], however, each wedge is only suited to a single, known surface profile and so multiple wedges may need to be constructed for the inspection of a complex component. Wedges are commonly used in industry but are unable to be applied to a wide range of imaging setups and are therefore not considered in the current work. A lesser-used hybrid method of these two previous approaches has also been considered, which involves the use of a membrane-coupled phased array device. The membrane can either be a water-filled, low-loss membrane attached to a standard linear 1D phased array which then conforms to the surface profile [42, 43], or a silicone-based coupling pad [44].

The final approach involves the use of a flexible contact array, of which there are two types: the first is a linear array where each element is able to move perpendicularly as the array is translated across the surface [45–47], while the second is constructed using flexible composite material that moulds to the surface [48]. As the first type of flexible array can only adapt in one dimension, it can not be applied to elbows and nozzles and is therefore unable to be applied to this research. Like wedges, the composite arrays are designed with a specific application in mind and are not suitable for all applications.

Throughout this thesis all non-contact inspections use the setup described in the first method, whereby water is used as the acoustic couplant.

3.2 Singly and doubly curved surfaces

The types of non-planar surfaces focused on in this thesis are smooth and curved, of which there are two categories: singly curved and doubly curved. Both represent geometries that are routinely inspected in industry and hence their relevance to the current work.

Singly curved, or developable, surfaces have zero Gaussian curvature everywhere and can be created by transforming a plane without causing stretching, cutting or wrinkling. The tangential plane touches surfaces of this type by a line. Pipes are examples of this surface as they can be 'unrolled' into a plane. As there is curvature in only one principal axis, the use of linear arrays is sufficient to obtain well-focused planar images. However, using this type of array means that resolution in the out-of-plane direction is limited. An illustration of a singly curved surface and a tangenial plane is shown in Fig. 3.1(a).

Doubly curved, or non-developable, surfaces describe the majority of smooth surfaces and have non-zero Gaussian curvature across their surface; every point on the surface has an associated tangential plane. As mentioned in the project motivation, pipework branches and pressure vessel nozzles are relevant examples of this type of surface. Linear arrays are unable to focus efficiently through surfaces of this nature due to the curvature in both principal axis, and a 2D array becomes necessary for imaging. An illustration of a pipework branch is illustrated in Fig. 3.1(b), where a surface normal point is shown on the doubly curved region.

3.3 GPU parallel computing

When considering 2D TFM imaging, the central processing unit (CPU) of a desktop PC can process data at adequate speeds; however with the inclusion of a third dimension, as is the case in 3D TFM imaging, the number of voxels in the final image increases drastically. The calculations and images in the previous chapter were processed using the MATLAB computing software, with image processing times in excess of an hour using a 2D array in immersion. This process is slow in MATLAB as the ToF calculation for each element and voxel pair is calculated in series, which is a serious limitation when 3D imaging is considered. As each calculation is independent of the others, i.e. the distance between an element and voxel does not depend on other elements or voxels, a huge opportunity to speed up the process lies in parallelisation [49].

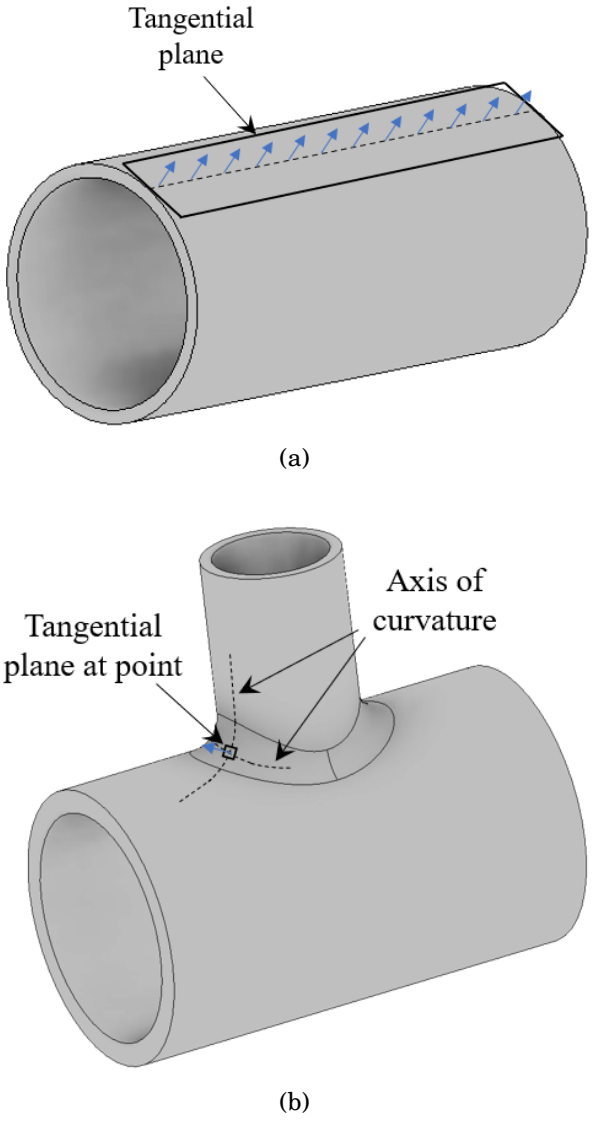

FIGURE 3.1. Illustration of (a) a singly and (b) a doubly curved surface. Surface normals corresponding to marked tangential planes are shown by blue arrows.

Within the last couple of decades, graphics processing units (GPUs) have been extensively used for general-purpose parallel computation within scientific research [50–53]. GPUs are commonly used in the gaming industry due to their ability to quickly render images by processing large blocks of data in parallel, which makes their application to the current work desirable. While CPUs are optimised for sequential serial processing using few cores, GPUs are optimised for executing massively parallel operations at once across many cores. For reference, the CPU in the PC used for this work has

4 cores, while the GPU used has 3,072 GPU cores.

To accelerate the compute-intensive imaging process, the parallel computing platform CUDA was used to parallelise the ToF and TFM calculations. CUDA is designed specifically by Nvidia for use on their GPUs and it allows developers to speed up their computations by harnessing the power of thousands of parallel threads [54]. To speed up the imaging process, a CUDA executable was written to calculate the ToF for each transmit-receieve element pair and sum the associated amplitudes at each voxel within a defined grid. The executable was called in a MATLAB script, where the data set was filtered before a binary file was written that contained all the imaging parameters. The CUDA script then produced a binary file as an output containing a matrix of amplitudes that represents the TFM image. The processing speeds for a single-medium TFM algorithm using solely the CPU (MATLAB) and GPU (CUDA) is shown in Fig. 3.2 for an increasing number of voxels and a 128-element array. The graph shows that the processing time for each platform increases linearly with an increasing number of voxels, but the MATLAB case increases significantly faster. This difference in processing time is more pronounced in the case of immersion imaging where the calculation of global minimum ToFs for transmit-receive element pairs and voxels through surface points is necessary; without GPU processing 3D imaging using a 2D array would be unfeasible.

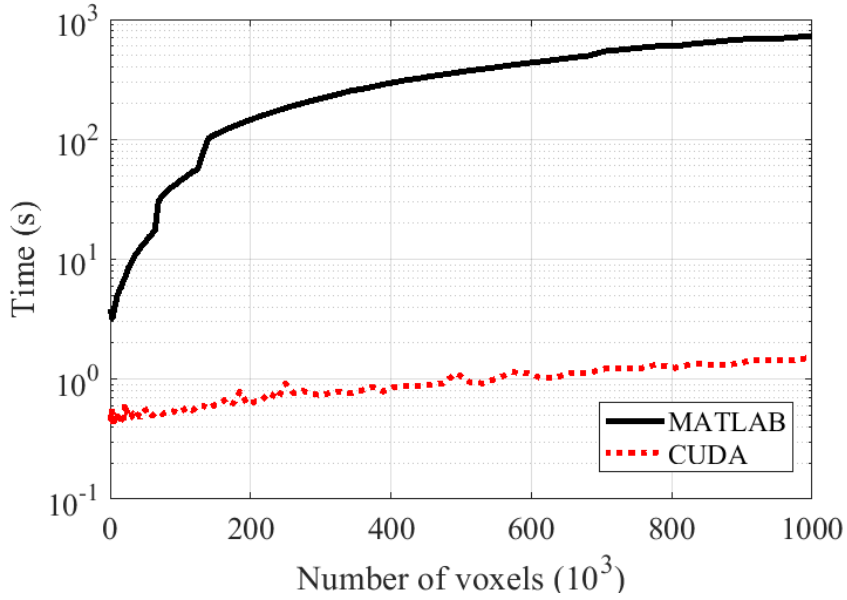

FIGURE 3.2. Single-medium TFM processing time against number of voxels using MATLAB (CPU) and CUDA (GPU).

3.4 Surface extraction

The surface compensation method presented in section 2.2.1 is only suitable for a planar surface which is constant across the x and y directions, but fails for non-planar surfaces which can vary across 3D space. A more robust method is therefore required.

The solution used here involves extracting the surface profile from a single-medium TFM image generated in the region around the expected surface location using only the acoustic velocity of water. A rough estimate of the surface location can be found from the A-scans, where the surface was assumed to be at the average location of the first reflections across all time-domain data. A 'window' can then be defined over the approximate volume that encompasses the surface to be imaged, as illustrated in 2D in Fig. 3.3, where the parameter ε determines the size of the window in the z direction. As the location and nature of the surface is unknown at this point, ε needs to be large enough to cover the potential surface region underneath the array. In the current work, ε is set to ~6 mm; this value is surface-dependent and should therefore be chosen according to the nature of the specimen being imaged.

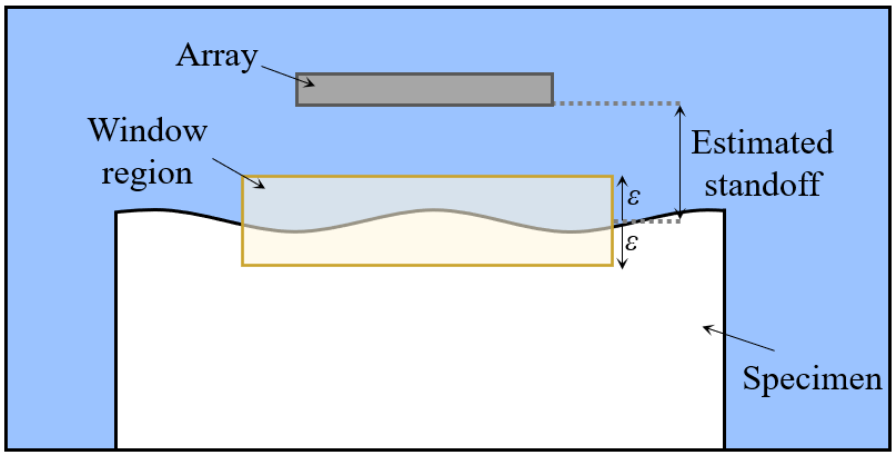

FIGURE 3.3. 2D illustration of a specimen immersed in water. The yellow box highlights the window region that a single-medium TFM is to be generated in to allow image-based surface extraction. ε determines the size of the window in z.

An illustration of a ray path for single-medium immersion imaging is shown in Fig. 3.4, where $\mathbf{E}_T$ and $\mathbf{E}_R$ are the position vectors of the transmitting and receiving elements respectively, $\mathbf{P}_1$ is the position vector of the image point and v_1 is the velocity of sound in the medium, which is water in this case. The dotted lines represent the

outline of the unknown surface of the specimen and has no part in this stage of the imaging process. For an arbitrary image point $\mathbf{P}_1$ the image intensity, $I_{surf}(\mathbf{P}_1)$, for each transmit-receive element pair is calculated using Eq. (2.1).

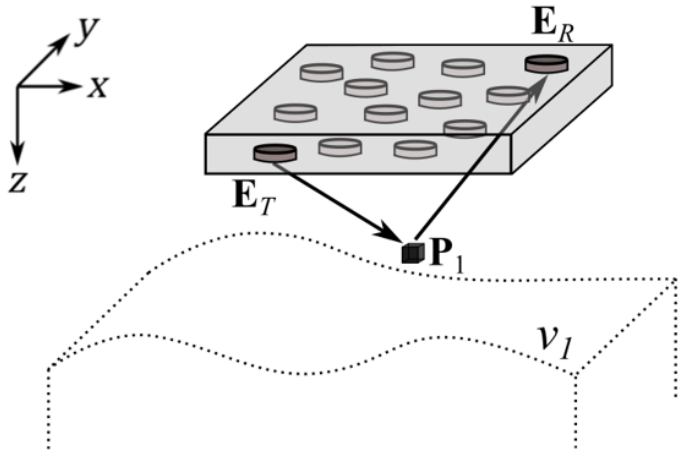

FIGURE 3.4. 3D illustration of a ray path in a single medium that yields the global minimum ToF between $\mathbf{E}_T$, $\mathbf{P}_1$, and $\mathbf{E}_R$ using a 2D phased array. The outline of the unknown surface of the specimen is shown by the dotted lines and plays no part in the calculation of the ray path in this case. v_1 represents the velocity of sound in water.

Another factor that has to be considered when imaging a non-planar surface is the frequency $h_{T,R}(\tau)$ is filtered at. When imaging in the specimen material, the A-scans are filtered at f_c, but when imaging in water to obtain a TFM image of the surface profile, it was found that by lowering the filter frequency to a fraction of f_c reduced the appearance of artefacts in the water. These artefacts are commonly observed when imaging non-planar surfaces due to the interference of sound waves when they reflect off the surface at different angles. Lowering the filter frequency reduces artefacts but consequently lowers resolution and SNR due to operating further away from f_c, so there is a trade-off that generally requires some trial and error.

Perhaps an intuitive and fast method of extracting a surface profile at this stage would be to simply take the locations of maximum amplitude in z at each (x, y) location in $I_{surf}(\mathbf{P}_1)$ as surface points. This could be a viable method if the strength of surface reflections was constant, but this is not often the case due to a combination of a complex surface profile and probe orientation. This presents an issue as simply taking the points that are above a specified threshold amplitude to define the location of the surface can result in a discontinuous surface, particularly in the presence of noise. This method

of extracting a surface was used in a previous study [38], where linear interpolation was used to bridge gaps between locations of surface image points above a threshold. However, in that work a linear array and 2D TFM image was considered, and it would be difficult to apply to the current work as the surface curves throughout 3D space. A more sophisticated, two-pass surface extraction process is therefore required. This process is outlined as follows.

A discrete point in the imaging grid is defined as $\mathbf{P}_{ijk} = \left(x_i, y_j, z_k\right)$, where x_i denotes equally spaced points in x, and similarly for y_j and z_k. The image amplitude at this point is then obtained by $I_{ijk} = \left|I_{surf}\left(\mathbf{P}_{ijk}\right)\right|$. The first step of the extraction process is to find the indices $(i,j,k) = (I,J,K)$ of the location of the maximum amplitude in the TFM image using:

$$(I,J,K) = \underset{(i,j,k)}{\operatorname{argmax}}\ I_{ijk} \tag{3.1}$$

and therefore $\mathbf{P}_{IJK} = (x_I, y_J, z_K)$ is taken as the first point of the extraction process. Let $Z_{ij}^{(1)}$ denote the 3D surface points that are to be determined. The first surface point obtained in $Z_{ij}^{(1)}$ is the value of the z coordinate at the position of the global maximum found above:

$$Z_{IJ}^{(1)} = z_K. \tag{3.2}$$

In the first pass, the primary and secondary directions are x and y respectively. The 2D $(x-z)$ plane through y_J is examined first by working out from $(i,j) = (I,J)$ in the primary direction. The next surface point in the x direction, i.e. $Z_{(I+1)J}^{(1)}$, is found by fitting a spline, $\xi(z)$, to the image amplitudes $I_{(I+1)JK}$, at k-indices that satisfy

$$Z_{IJ}^{(1)} - \delta z \ \leq\ z_k \ \leq\ Z_{IJ}^{(1)} + \delta z, \tag{3.3}$$

where δz is a predefined tolerance parameter, in this case set to approximately $1.2\lambda_1$, where λ_1 is the wavelength of sound in water that was calculated to be approximately 0.49 mm. If the maximum of $\xi(z)$ exceeds a predefined threshold, defined as 10 dB below I_{IJK}, then the z coordinate of the next surface point is defined as:

$$Z_{(I+1)J}^{(1)} = \underset{z}{\operatorname{argmax}}\ \xi(z), \tag{3.4}$$

with the procedure shown in Fig. 3.5. If no value is found in the range of Eq. (3.3) that satisfies the amplitude threshold, the surface point at $Z_{(I+1)J}^{(1)}$ is defined as absent and

the next position in the primary direction, $(i, j) = (I + 2, J)$, is considered instead. This is repeated until a valid point is found. At each absent point the value of δz is slightly increased in case there is a small gap in the surface that can be bridged. When a valid surface point is found the process is then repeated from Eq. (3.3) starting at that point. This is repeated until 10 consecutive absent points are encountered, corresponding to $6\lambda_1$, which is assumed to indicate that the edge of the measurable surface has been reached. Surface points in the negative x direction from $\mathbf{P}_{IJK}$, i.e. $Z^{(1)}_{(I-1)J}$, are then extracted until the other edge of the surface is reached. This extraction is shown in Fig. 3.6(a), where the primary direction is shown by the red arrow and the extracted points along the plane are shown by the blue dots. The values of the parameters involved in this surface extraction process are tuned to result in a fully extracted surface and are defined beforehand through trial and error. Future work can be done to automate this process to make the imaging procedure more robust (i.e. applicable to a wider range of surface profiles).

The surface is then extracted in the secondary direction. This is achieved by starting with each of the previously extracted surface points in the primary direction and applying the same process in the secondary direction. This is shown by the dashed grey arrows in Fig. 3.6(a) and $Z^{(1)}_{ij}$ is now filled with the z coordinates of the extracted surface. This concludes the first pass of the surface extraction process.

In the second pass, the entire extraction process is then repeated, only this time with y as the primary and x as the secondary direction, as illustrated in Fig. 3.6(b). This yields a second estimate of the surface profile, $Z^{(2)}_{ij}$.

The fully-extracted 3D surface of points, Z_{ij}, is then found by averaging the two extracted surfaces:

$$Z_{ij} = \frac{Z^{(1)}_{ij} + Z^{(2)}_{ij}}{2}. \tag{3.5}$$

The reasoning behind extracting the surface in two passes is to ensure reliable coverage of the surface, independent of the starting point. This would not necessarily be achieved in a single pass, as shown by the yellow regions in Fig. 3.6.

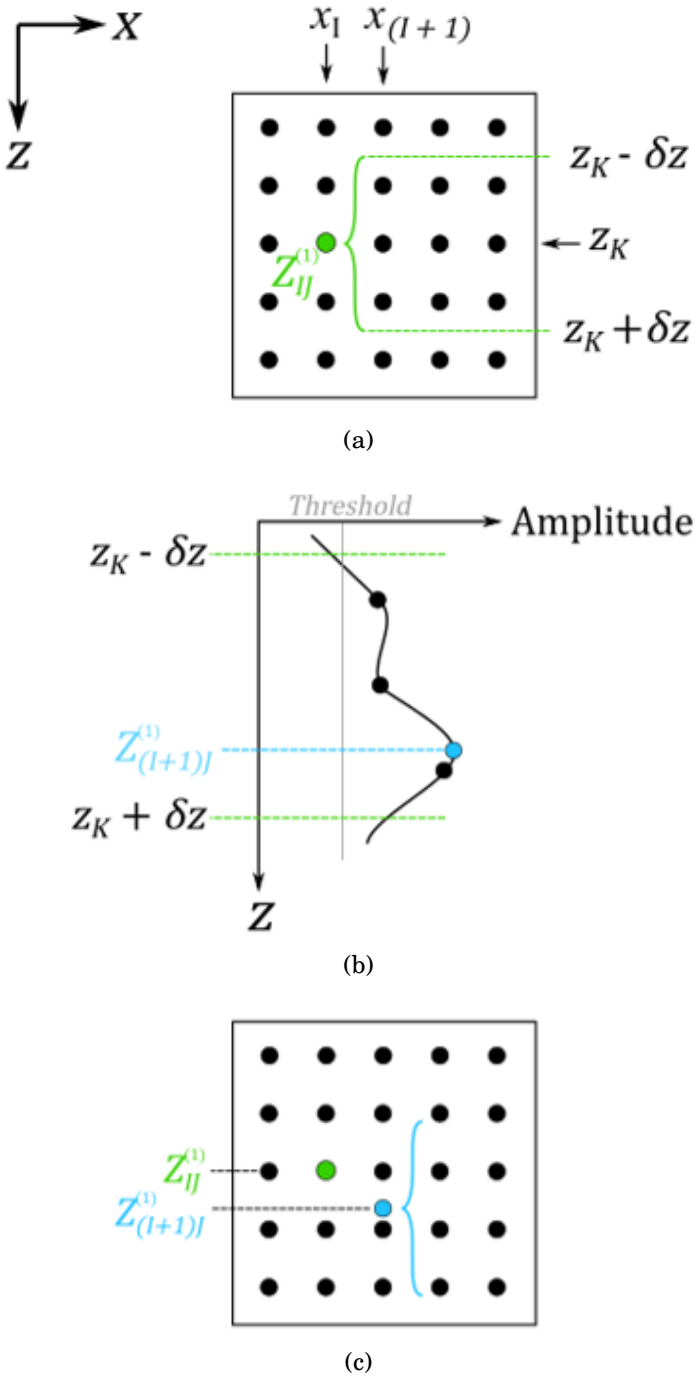

FIGURE 3.5. Illustration of the surface extraction method for a doubly curved surface. (a) shows the application of $\pm\delta z$ constraint starting from the global maximum point, $Z_{IJ}^{(1)}$, on the neighbouring x column. (b) shows the fitting of a spline, $\xi(z)$, to points in $Z_{(I+1)J}$ within the $z_K \pm \delta z$ range and the subsequent extracted surface point from the maximum of $\xi(z)$. (c) shows the location of the extracted point and illustrates the continuity of the process.

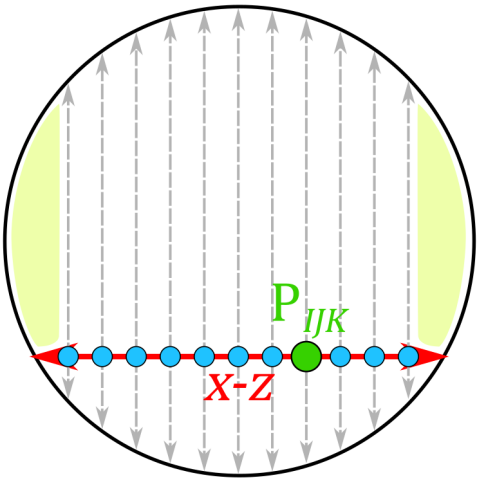

(a)

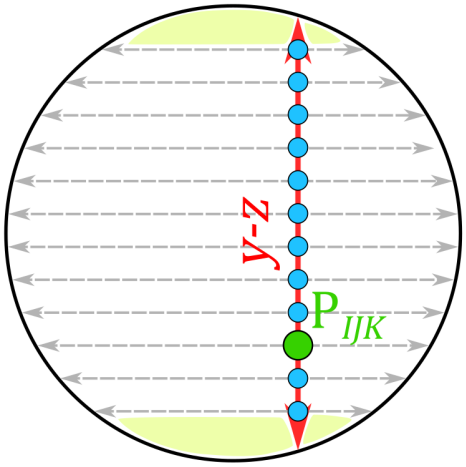

(b)

FIGURE 3.6. Illustration of a top view of the extraction process. The green dot symbolises the starting point of the extraction process, $\mathbf{P}_{IJK}$, the blue dots symbolize extracted surface points along the red primary extraction direction and the dashed grey arrows show the secondary extraction direction. (a) shows the extraction directions when the x axis is the primary direction to generate $Z_{ij}^{(1)}$, while (b) shows the result when y is the primary direction to generate $Z_{ij}^{(2)}$. The yellow regions are unable to be imaged from the relative starting points using this method.

3.5 Inspection in immersion

The extracted surface points were then used for the interior imaging process. As was mentioned when conducting immersion imaging through a planar surface in section 2.2, Fermat's principle was used to determine the overall minimum, or global minimum, ToF between element pairs and image points. An example of such a ray path that minimises the travel time between $\mathbf{E}_T$, $\mathbf{P}_2$ and $\mathbf{E}_R$ is shown in Fig. 3.7, where an additional acoustic velocity, v_2, now also needs to be taken into consideration. The path includes the surface-crossing locations, $\mathbf{A}_T$ and $\mathbf{A}_R$ and the intensity of the image, $I(\mathbf{P}_2)$, at any image point in the interior imaging grid is calculated using Eq. (2.4). This imaging process whereby two TFM images are generated (the first to extract the surface profile and the second to image inside the component) is also known as adaptive imaging [5, 39, 55].

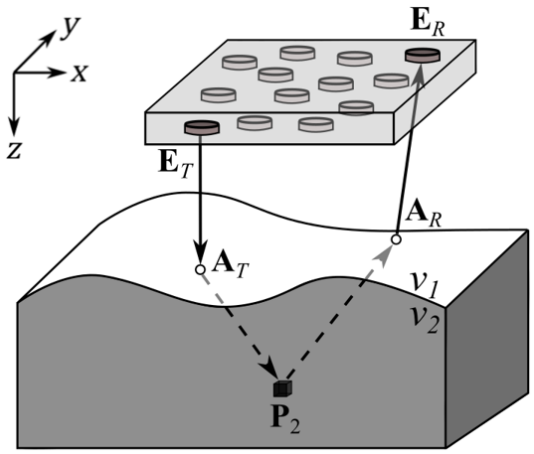

FIGURE 3.7. 3D illustration of a ray path in immersion that yields the global minimum ToF between $\mathbf{E}_T$, $\mathbf{P}_2$, and $\mathbf{E}_R$, when passing through surface-crossing locations $\mathbf{A}_T$ and $\mathbf{A}_R$ using a 2D array. Solid arrows represent rays travelling in water, while dashed arrows represent rays travelling in the specimen. v_1 and v_2 are the velocities of sound in water and the specimen respectively.

A flow diagram of the methodology of the imaging process is shown in Fig. 3.8. Solid symbols denote processes executed on the CPU using MATLAB, while dashed symbols represent processes executed in parallel on the GPU using CUDA.

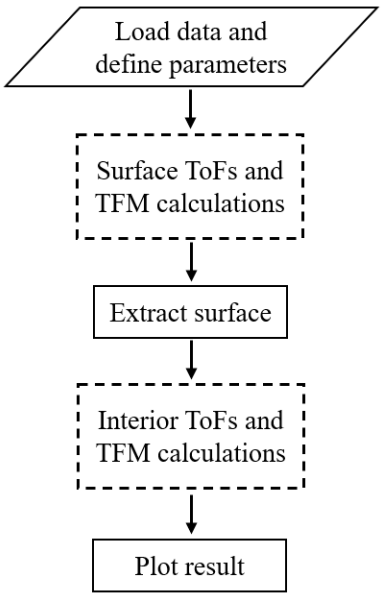

FIGURE 3.8. The flow diagram for TFM imaging in immersion through a non-planar surface using a single array position. Solid symbols are processes calculated on the CPU using MATLAB, while dashed symbols are processes calculated in parallel on the GPU using CUDA.

3.5.1 Doubly curved specimen #1

To represent a doubly curved surface geometry, an aluminium specimen with a double-curved axisymmetric surface was manufactured and shown in the side profile in Fig. 3.9(a). The surface was created with a Gaussian function centred on the peak given by:

$$H = H_0 \exp\left(-\frac{r^2}{2\sigma^2}\right) \tag{3.6}$$

where r is the radial distance from the peak, H_0 is the height of the peak and σ is the standard deviation parameter of the Gaussian function. For this specimen, H_0 was 15 mm and σ was 20 mm, resulting in a steepest angle of inclination on the surface that was approximately 24° relative to the horizontal. The longitudinal velocity of sound in the specimen, v_2, was measured to be 6360 m/s, and hence the wavelength of sound at the centre frequency of the array, λ_2, was 2.1 mm. 21 conical bottom-drilled holes (BDHs) were drilled into one side of the base of the specimen, with the tip of each hole on each radial arm from the peak at a different depth below the surface; the other side of the specimen contained four square electrical discharge machined (EDM) notches at different depths. The BDHs were drilled using a standard 120° inclusive drill bit of 3 mm diameter ($1.4\lambda_2$) and the EDM notches were machined with a wire of 0.5 mm width ($0.2\lambda_2$). A bottom-view of the specimen is shown in Fig. 3.9(b) with each defect labelled. The depth of each radial arm below the surface increases from 5 mm (corresponding to the arm containing BDHs A–E) to 25 mm (corresponding to the arm containing BDHs R–U) in 5 mm increments. A 3 mm surface notch was drilled into the top surface of the specimen to act as a reference point for surface orientation and defect positioning.

All of the machined defects will be examined in the following chapter, but this chapter focuses solely on a single array position that is located above defects K and L, as illustrated by the yellow highlighted regions in Fig. 3.10. This location was chosen as any region with a larger surface inclination would result in a large portion of the reflected sound energy missing the array, as depicted in Fig. 3.11. To prevent this from happening, the standoff distance can be reduced or the array can be rotated so it is parallel with the surface tangent. As the defects to be imaged are directly beneath the array, which is aligned parallel to the back wall of the specimen, this effect needs to be avoided and so a suitable standoff distance needs to be determined. It is important to note that the array in this position could be used to image other parts of the surface or defects, depending on the geometry of the surface and refraction of ray paths, but for simplicity only the defects located underneath the array footprint were imaged here.

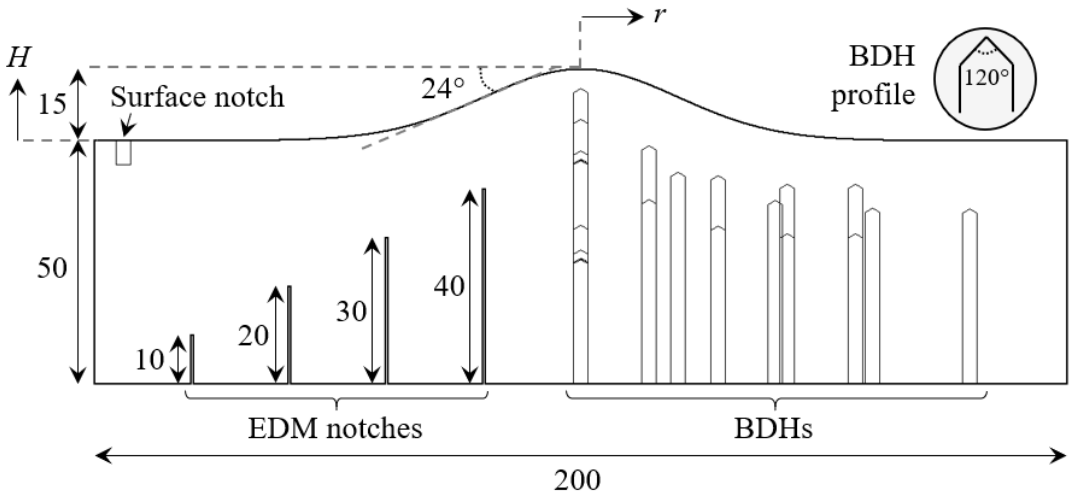

(a)

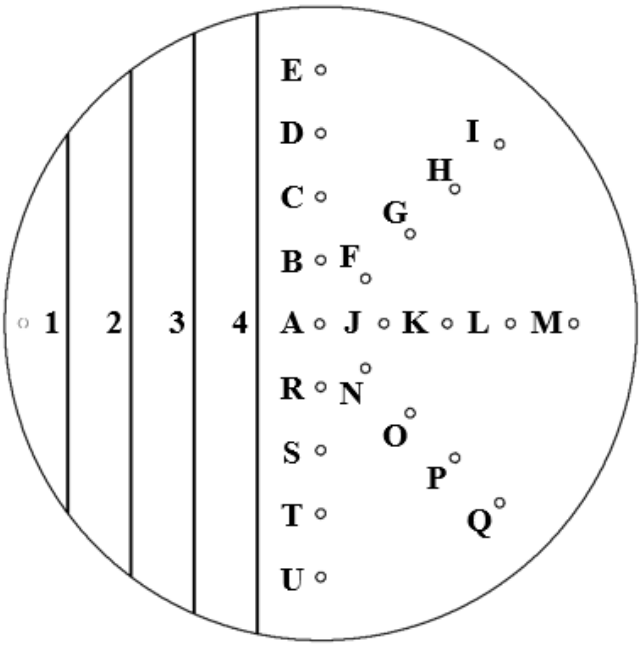

(b)

FIGURE 3.9. Illustration of doubly curved specimen #1 with machined defects. (a) shows the side profile and (b) shows the base view with the defects labelled. Units in mm.

A schematic diagram of the experimental setup is shown in Fig. 3.12, where the array mounting has three degrees of freedom and is connected to a motor. Firstly, the velocity of sound in water, v_1, was measured to be 1470 m/s which corresponded to a wavelength, λ_1, of 0.49 mm. To initialise the scan, the specimen was submerged in water and the array was mounted and aligned parallel to the back wall of the specimen using a B-scan image obtained over the flat region of the surface. The array was then set to a standoff distance of 13 mm above the peak of the specimen, before being moved to the correct location for imaging defects K and L. A HMC data set was captured with 10 averages, then filtered and Hilbert transformed using a Gaussian window function centred at $f_c/3$ with a -40 dB half bandwidth of 90% of $f_c/3$.

3.5.2 Results

The result of applying the single-medium 3D TFM algorithm to the captured data set is shown in Fig. 3.13(a) as multiple isosurfaces plotted relative to the maximum surface amplitude, where the array is located at $z = 0$ mm. The method described in section 3.4 is then applied to extract a discretised estimate of the surface profile, shown in Fig. 3.13(b) as a surface plot.

The interior 3D TFM image obtained by using Eq. (2.4) is shown in Fig. 3.14. Fig. 3.14(a) shows defects K and L and the back wall of the specimen, while Fig. 3.14(b) shows a zoomed in region around the defects. Defect K is located in positive y and defect L is in negative y.

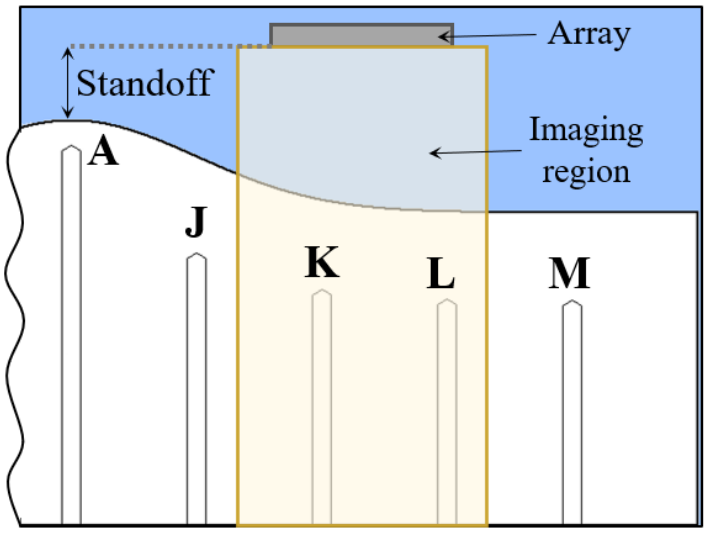

(a)

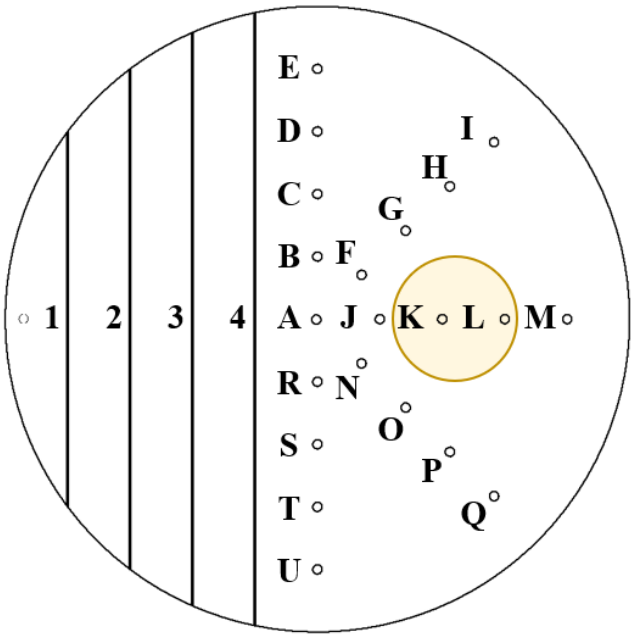

(b)

FIGURE 3.10. Reduced region of doubly curved specimen #1 that is used to investigate 3D TFM imaging through a non-planar surface. (a) shows the side view and (b) shows the base view. BDHs K and L are within the imaging region highlighted in yellow.

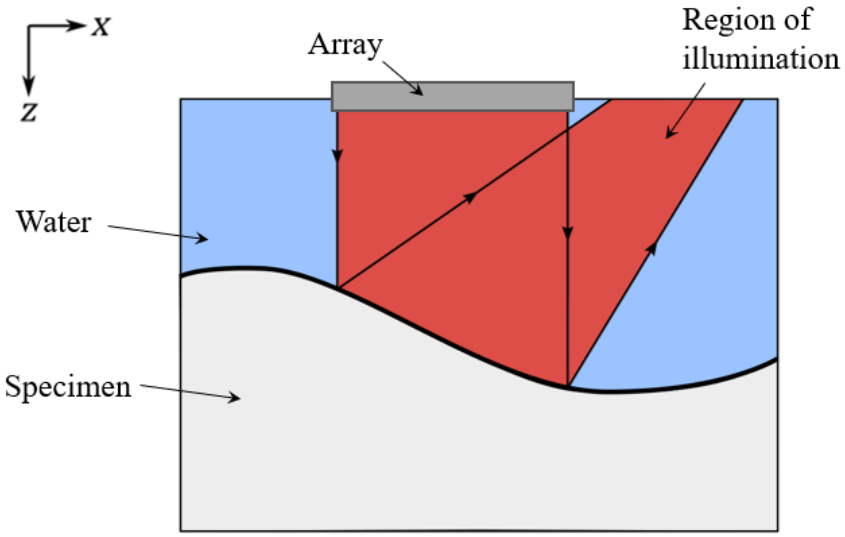

FIGURE 3.11. Schematic showing the reflection of a sound pulse from a non-planar surface.

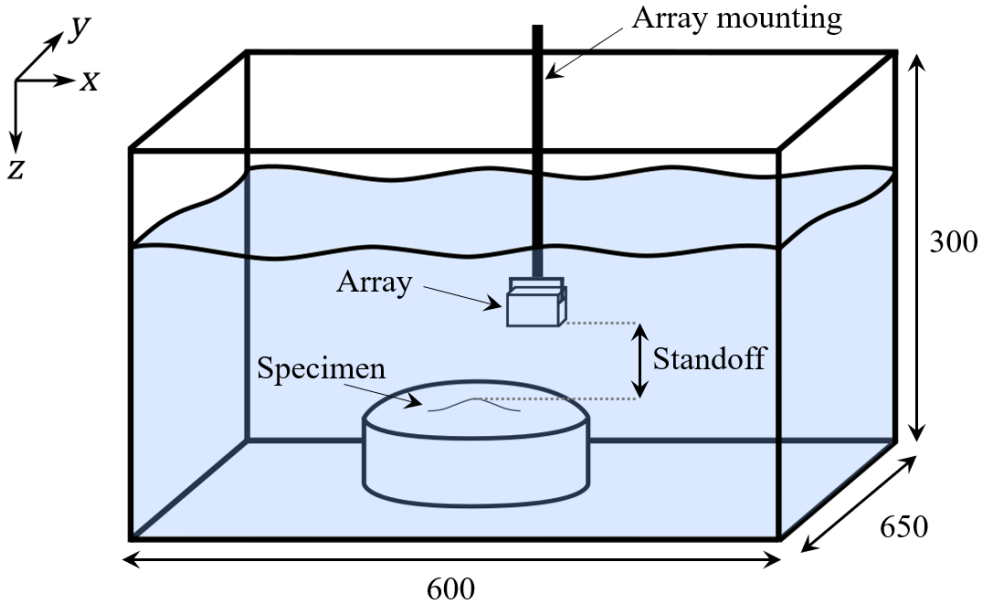

FIGURE 3.12. Illustration showing the experimental setup used to image a non-planar surface in immersion. The standoff between the peak of the specimen and the array was 13 mm. Units in mm.

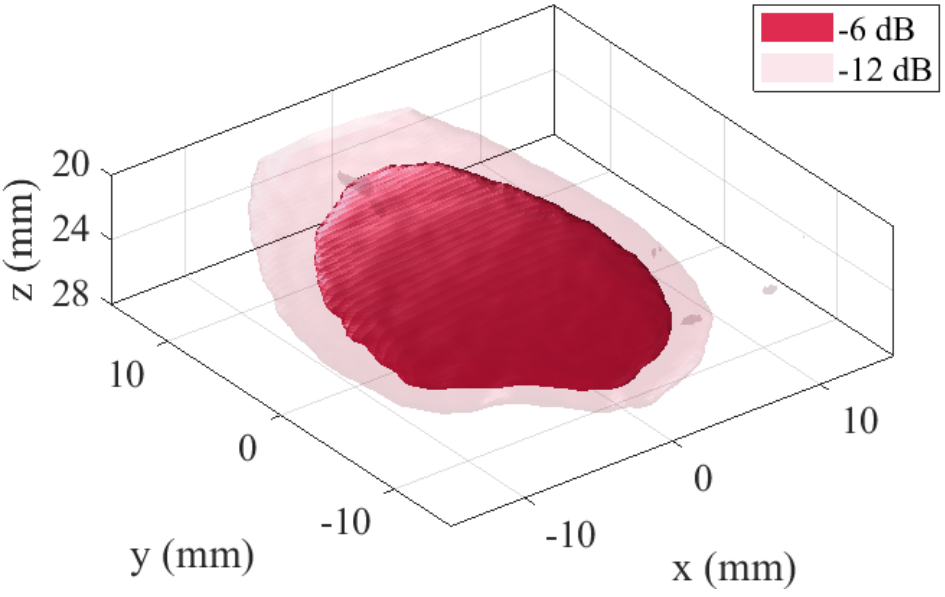

(a)

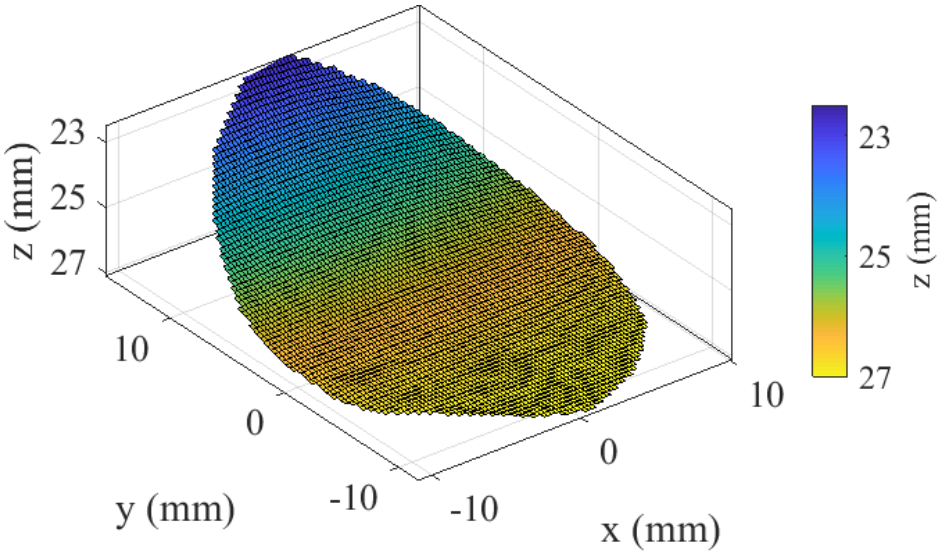

(b)

FIGURE 3.13. Surface results for a single array position over a non-planar surface. (a) Shows the 3D TFM image plotted as isosurfaces at two amplitude levels, and (b) shows a surface plot of the extracted surface points that are coloured according to depth in z. The isosurfaces in (a) are plotted relative to the maximum amplitude in the surface.

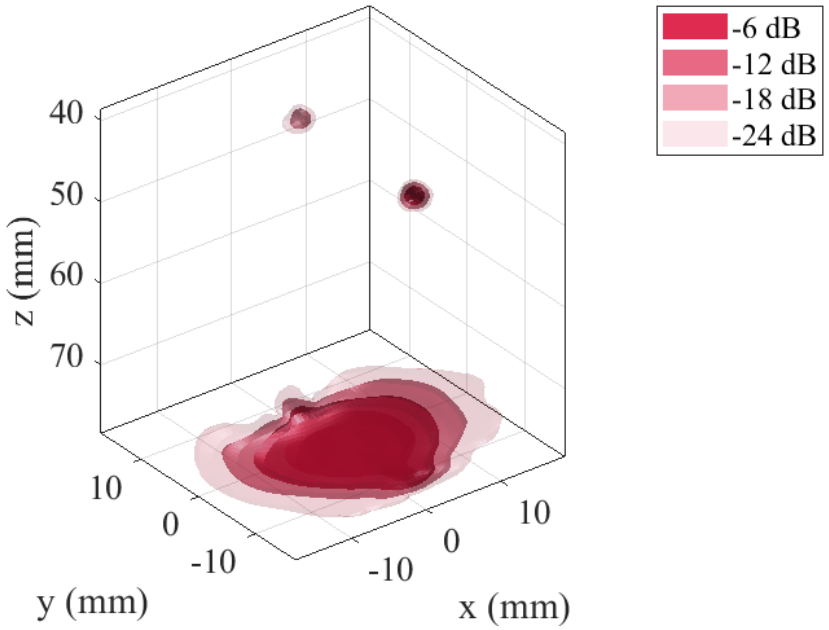

(a)

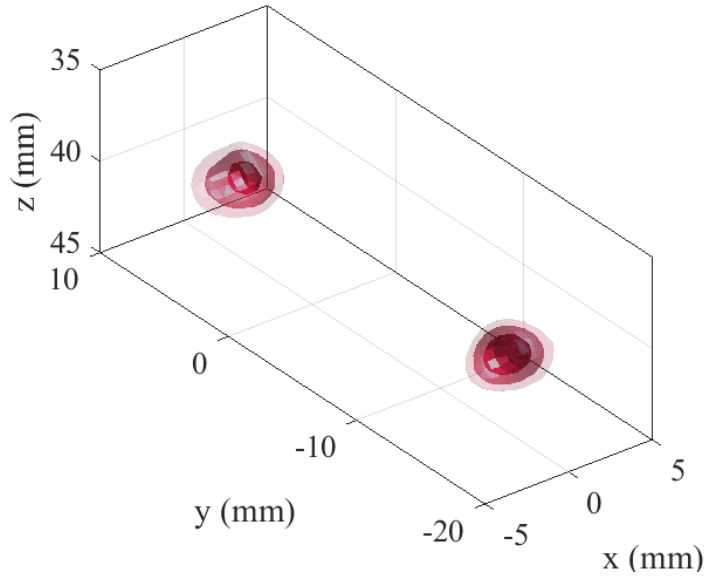

(b)

FIGURE 3.14. Interior 3D TFM results for a single array position over a non-planar surface. (a) Shows the position of the defects relative to the back wall, while (b) a zoomed in plot of the defects. Defect K is positive in y, while defect L is negative in y. The dB scale is relative to the maximum amplitude in the back wall.

3.5.3 Discussion

By examining Fig. 3.13(a), the single-medium TFM image in water has successfully produced an image of the surface of the specimen. The data was filtered at $f_c/3$ as this value was found to reduce surface noise while preserving adequate SNR for surface extraction. The difference in z for each (x, y) location of the extracted surface when compared with Eq. (3.6), ΔZ, is shown in Fig. 3.15. The comparison shows a gradual increase of ΔZ from $(-x, -y)$ to the $(+x, +y)$ region, which is indicative of Eq. (3.6) not being in the same reference frame as the specimen. Although the array was aligned parallel to the back wall of the specimen, the specimen's frame of reference is not the same as the equation's, as illustrated in Fig. 3.16. However, the root-mean square error (RMSE) of ΔZ was found to be 0.099 mm, which provides confidence that the surface extraction algorithm is correct. In the following chapter a method for aligning the coordinate systems is introduced to allow a more accurate surface comparison.

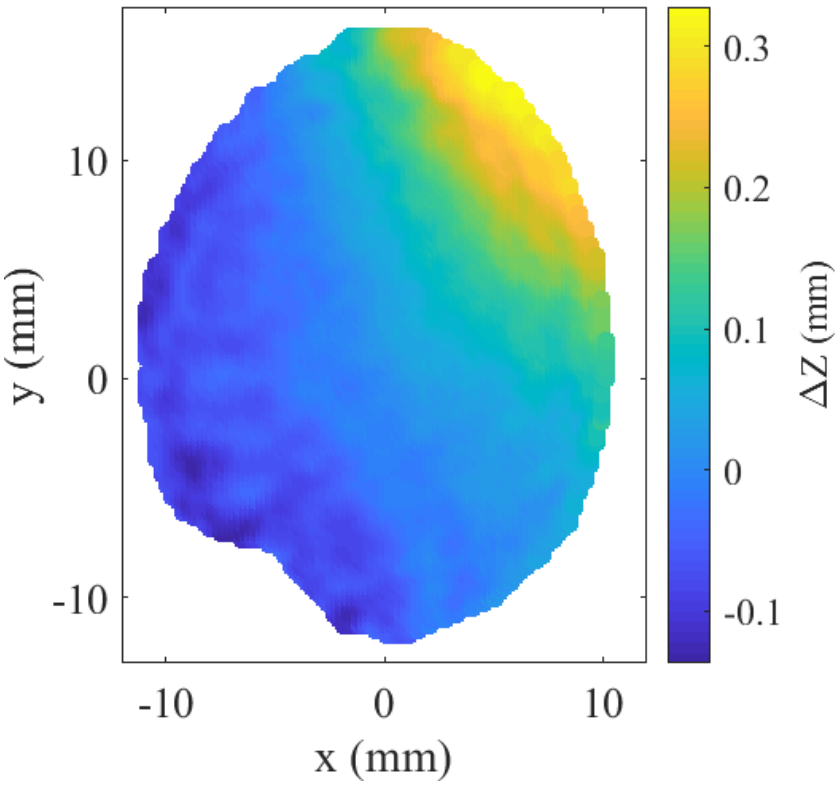

FIGURE 3.15. The difference between z values at each (x, y) location of the extracted surface profile with the values obtained from Eq. (3.6).

.

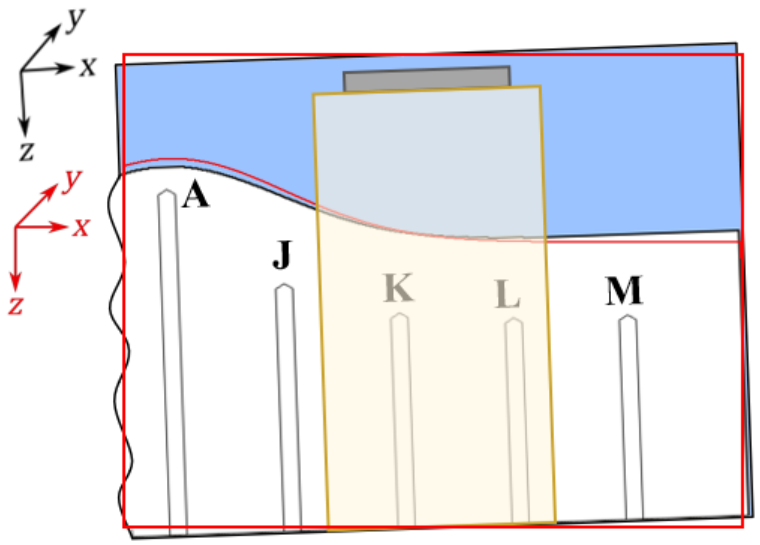

FIGURE 3.16. Unequal alignment of the reference frames for Eq. (3.6) (in red) and the experimental setup (in black).

The interior 3D TFM results in Fig. 3.14 show well focused defects and a clear back wall indication. By using the z location of the back wall, Table 3.1 shows a comparison between the measured and machined depths of the imaged defects. The back wall location was found by averaging the z locations of all image points with an amplitude greater than 6 dB below the maximum back wall signal. The results show that the measured positions agree with the machined distances within an error of $\pm 0.15\lambda_2$, with the measured depth of defect L being closer to the machined depth than defect K. The $V_{\text{-6 dB}}$ values of the defects were then investigated, with the results presented in Table 3.2. Again, defect K was imaged slightly better than defect L as evidenced by a smaller measured defect volume. Fig. 3.17 shows the locations of each defect relative to the surface described by Eq. (3.6) and the array position, located at $z = 0$ mm. As defect K is located beneath a more inclined region of the surface than defect L, it logically follows that the imaging quality here would be lower as less energy is being transmitted into the specimen. However, as the defect is focused and it was able to be positioned accurately, the overall effect of the surface curvature is minimal in this case.

TABLE 3.1. Comparison of measured and machined defect locations using a non-planar surface. Units are in mm.

Defect	**Measured z depth**	**Machined z depth**	**z difference**
K	36.35	36.67	0.32
L	34.89	35.08	0.19

TABLE 3.2. API values for imaged defects K and L through a non-planar surface profile.

Defect	$V_{-6\,dB}$ (mm^3)
K	7.52
L	6.08

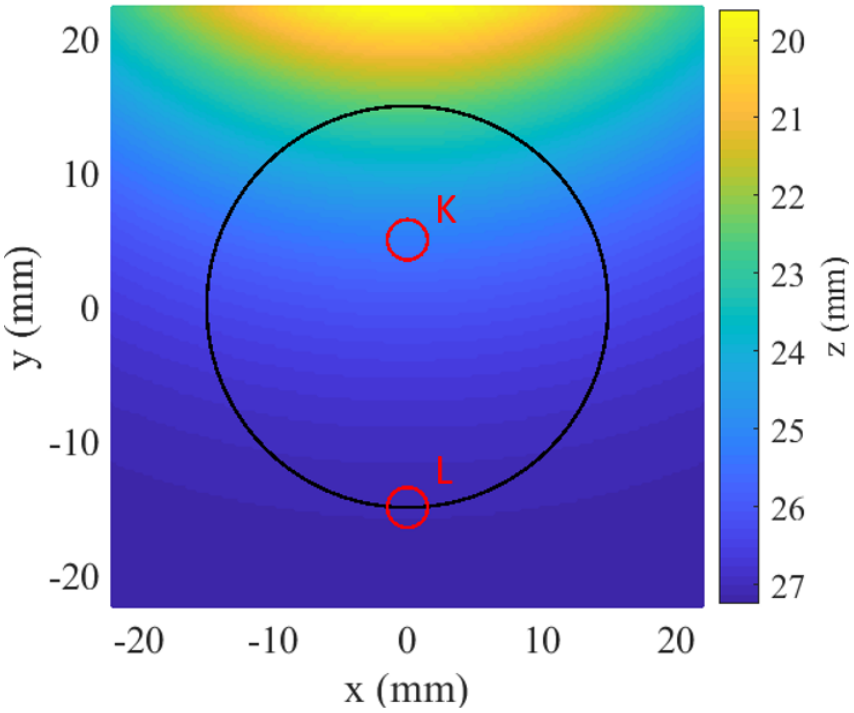

FIGURE 3.17. Surface location described by Eq. (3.6) with the positions of defects K and L labelled and the outline of the array position in black. The colourbar represents surface distance below the array, which is located at $z = 0$ mm.

When imaging in immersion, a concern raised in the previous chapter is the large number of calculations required and the accompanying long processing times. In this case, the first stage involving the generation of a single-medium TFM image of the surface required imaging a volume containing 5.4 million voxels. As the location of the surface was unknown, the volume had to be large enough to cover a substantial region below the array; in this case it was 1.5 times the diameter of the sparse array (30 mm) in x and y, and $\varepsilon = 10$ mm using a grid spacing of $\lambda_1/2$. The relationship between the processing time and number of pixels using the CPU in Fig. 3.2 can be described as:

$$\tau = 0.725 \cdot N \tag{3.7}$$

where τ is time in seconds and N is the number of voxels in units of a thousand. Using this equation, a volume containing 5.4 million voxels would take $\approx$ 3900 s to process, whereas the measured time to compute this using CUDA was found to be 7.2 s. With CUDA completing the calculations at a speed of more than 500 times faster than MATLAB for a single-medium scenario, it is clear that parallel programming is essential for immersion imaging as the number of calculations only increases with the inclusion of a layer of surface points. For completeness, imaging 700,000 voxels at a $\lambda_2/4$ grid spacing within the specimen using 7300 surface points took 17.1 s, yielding a total imaging time of approximately 24 s.

3.6 Summary

This chapter has discussed 3D imaging of defects through an unknown, doubly curved surface and presented a method for extracting a discretised 3D surface using an image-based approach. The inspection of doubly curved surfaces in industry is usually conducted using single-crystal transducers, which is time consuming and difficult, or potential hazardous radiographic methods. By demonstrating that 2D phased arrays have the ability to quickly and safely image through surfaces of this nature, inspections can be conducted faster, easier and with higher accuracy. The extracted surface was validated by comparing it with the equation of the surface and the defects were focused and accurately positioned. As the number of calculations increases drastically when imaging a 3D volume, the parallel computing platform CUDA was implemented to speed up the imaging process. The following chapter expands on these results to a scan of the entire specimen to further highlight the benefits of 2D phased arrays.

Chapter 4

Large, complex specimen inspection

All modern-day industrial structures contain large components that require regular inspection, such as large diameter pipes and turbine blades. Due to the size of these components and their integral role in a larger structure, inspections must occur *in situ* and therefore require a shutdown of the immediate area while an operator collects data; the motivations for this can include to reduce temperature, internal access to the pipe is required or the requirement to inspect turbine blades while they are stationary. Any inspection design therefore needs to consider how to collect the data as quickly and safely as possible in order to minimise costs. This is of particular importance in nuclear power plants where security access is strictly controlled and exposure to radiation is a huge concern. It is worth noting that continuous monitoring of thickness measurements by permanently installed sensors have become popular in recent years, particularly in plant regions where corrosion and fatigue cracking is of concern [56]. However, beam steering is not yet possible with these sensors and inspections are limited to pulse-echo.

Scanned arrays have become more popular within the last decade as a solution to not only speed up the data collection process, but also to conduct inspections in environments which pose a safety threat to humans [57–59]. The process involves fixing an array to a jig or motor-controlled system which can mechanically translate the array along a desired axis at a predetermined scan pitch. Data is collected at each position and can then be processed offline. Further benefits of using a scanned array include increased coverage, resolution and defect characterisation performance [60]. By scanning the array over the surface, the effective aperture and range of probing angles are increased which makes its use relevant to specimens with complex surfaces. Currently in industry

mainly linear 1D arrays are used in such scans, but implementing scanned 2D arrays is beneficial for improving the performance of ultrasonic inspections on large components.

In this chapter, the doubly curved test specimen described in the previous chapter is submerged in a water tank and an array is mechanically scanned across its surface. Individual data sets are collected at predefined array positions and combined to produce a single, large 3D surface TFM image of the entire specimen. The surface profile is then ultrasonically extracted using the method introduced in section 3.4, and a single, large 3D TFM image of the specimen's interior is produced. The accuracy of the extracted surface profile and subsequent performance on defect imaging is investigated.

4.1 Data acquisition

The experimental setup used to scan the specimen is the same as was illustrated in Fig. 3.12. The scanning tank has three translational degrees of freedom that were utilised to perform a 2D scan over the entire surface of the specimen. Before scanning, the velocity of sound in water, v_1, was measured as 1470 m/s which corresponded to a wavelength, λ_1, of 0.49 mm. To initialise the scan, the specimen was submerged in water and the array was mounted and aligned parallel to the back wall of the specimen using a B-scan image obtained over the flat region of the surface. The array was then set to a standoff distance of 13 mm above the peak of the specimen, before being moved to the scan start location.

A previous study investigating scanned arrays considered two methods of data collection using a linear 1D array [60]. The first involved translating the array by a fixed amount and collecting a data set at each location, while the second involved translating the array by a distance equal to the element pitch and populating a single data set using the last element of the array as a transmitter. As the sparse 2D array used here has randomly distributed elements, the second method cannot be applied to the current work, so therefore the first method is used in this chapter.

The total scanned area was (240×240) mm^2 using a total of 225 individual array positions at a pitch of 15 mm in x and y, resulting in an array aperture overlap of 50% between adjacent positions. An $(x-y)$ plane view illustrating the specimen location and individual array positions is shown in Fig. 4.1, where r_1 is the radius of the active region of the array and r_2 is the radius of the specimen. Time data was captured at each position with 10 averages, over a total scan time of approximately 1 hour.

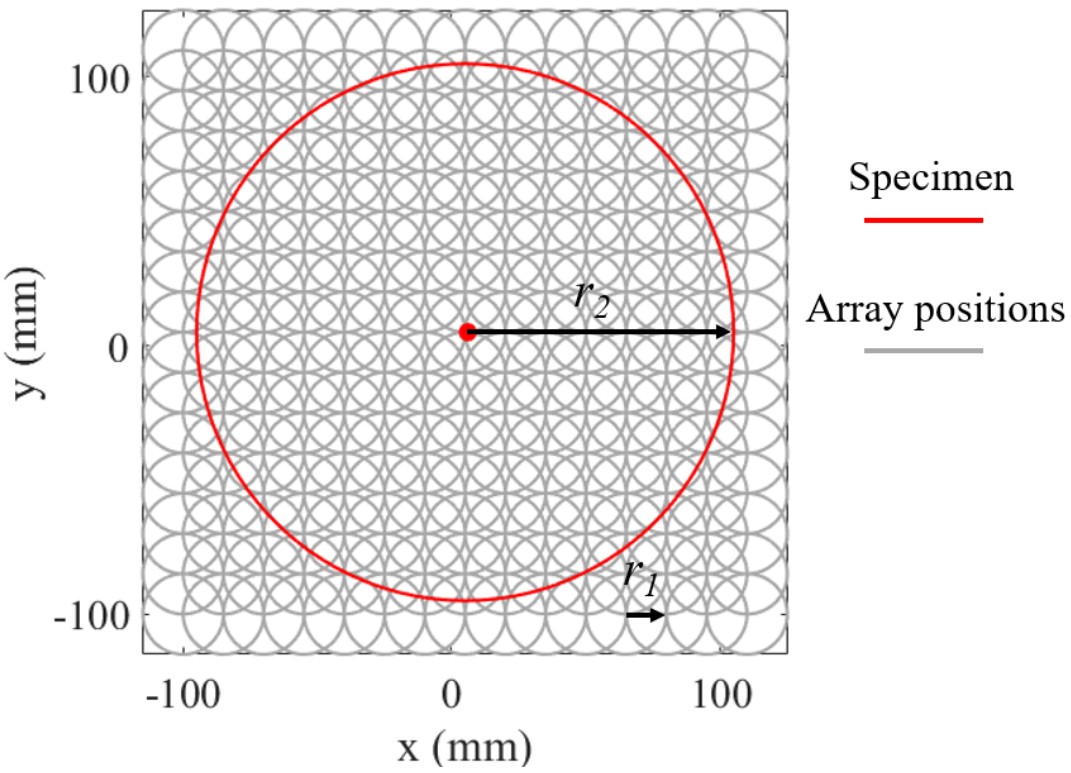

FIGURE 4.1. Scanned array positions with 50% overlap relative to the specimen location. r_1 and r_2 are the radii of the active region of the array and specimen respectively and the red dot represents the location of the peak of the specimen.

From Fig. 4.1 it is clear that some array positions are redundant; the scanning pattern results in a rectangle area being covered, so array positions at the corners of the scanned area that are not located over the specimen would therefore not produce any meaningful results. For this reason, only array positions which satisfy the condition

$$\text{distance} < r_1 + r_2 \tag{4.1}$$

are considered, where the distance is the separation between the centres of the array location and specimen. This reduces the number of data sets by roughly 20% to 185.

4.2 Post-processing analysis

When considering the task of processing the data sets, there are two methods of generating a single image that covers the entire volume of the specimen. The first involves

simply processing each data set to generate internal 3D volumetric TFM images independently, i.e. by applying the procedure outlined in Fig. 3.8 a total of 185 times, before combining the final interior TFM images into a single image. Using this method, only surface locations that are of near normal incidence to the array can be extracted. A consequence of this is potential loss of focus of regions within the specimen where ray paths travel through surface points that are not at near normal incidence to the array. The second method involves firstly generating 185 surface TFM images, combining them into a single, larger image before extracting a complete surface profile of the entire specimen. A subsection of surface points are then defined for each array position, which are used to generate the associated internal TFM images. An arbitrary limit of 1,000 points in the surface subsection is imposed in order to avoid using data collected from array positions which are mostly on the edge of the specimen, and hence are unlikely to produce useful images in the region directly beneath the array footprint. The final step involves combining the individual TFM images into a single, larger 3D volumetric TFM image. The associated methodology is outlined in Fig. 4.2. The second method is favoured as the surface profile under a given array position does not have to have been generated using the data acquired at that position. The process of combining individual TFM images into a single, larger TFM image will henceforth be referred to as 'stitching'.

4.2.1 Stitching TFM images

As the scan pitch was set to the radius of the array, some regions of the specimen were imaged multiple times, as illustrated in 2D for simplicity using 50% array overlap in Fig. 4.3. The regions imaged from array position 1 and array position 2 are coloured blue and orange respectively. The region of overlap in the middle where image points are viewed in both imaging region 1 and 2 therefore have two amplitude values associated with them. In this case, the assumed amplitude for each point is taken as the maximum value across both images. This method of combining individual images into a single, larger image is used for its simplicity and ease of implementation. A similar stitching method was used in the context of 2D imaging using a linear 1D array [38], whereby multiple small TFM images with overlapping regions were stitched to produce an image that was larger in size than the individual images. However, in that work the assumed amplitude of each image point was taken as the average of the individual amplitudes in each constituent image. The average amplitude is not used in the current work to avoid potentially diminishing the amplitude of a defect if it is imaged well from one

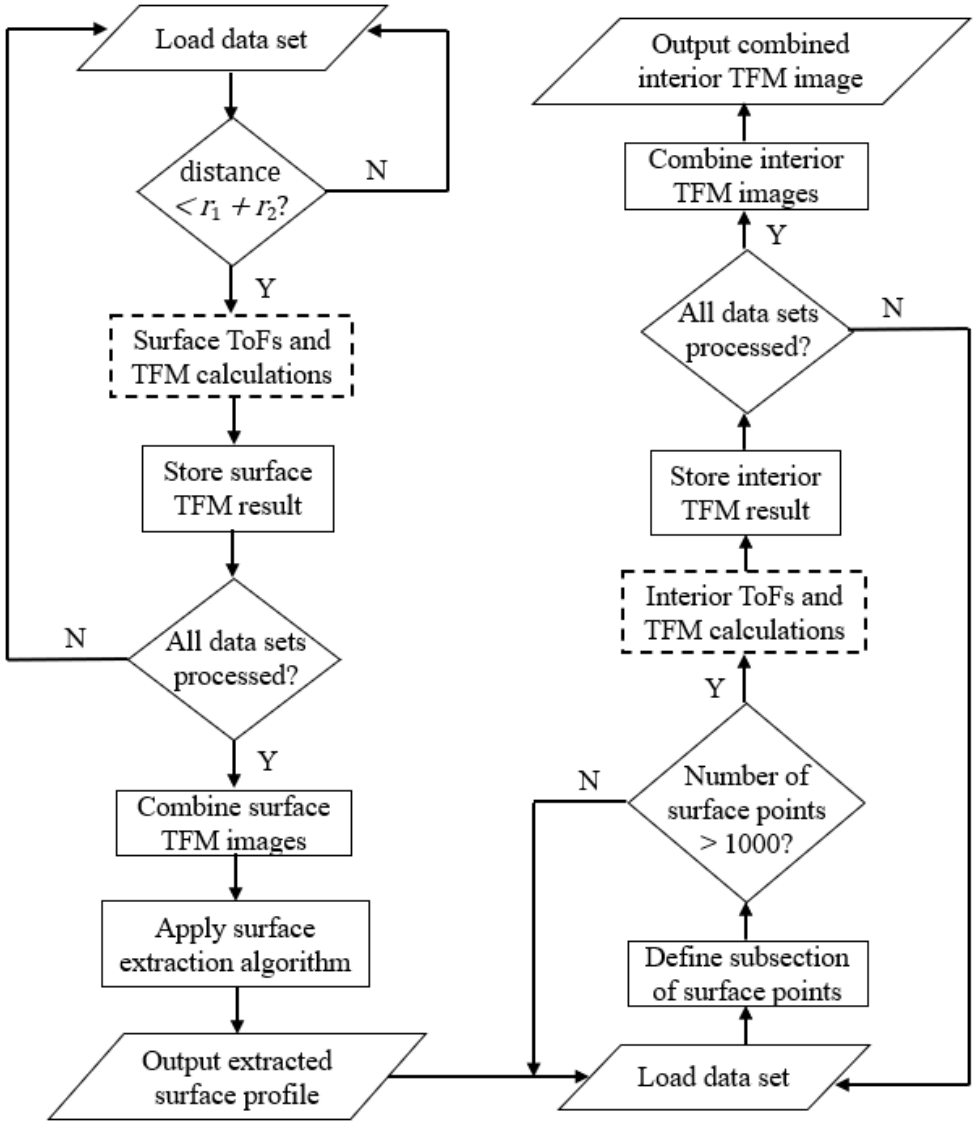

FIGURE 4.2. The flow diagram showing the methodology for generating a TFM image using a scanned array and multiple data sets. Solid symbols are processes calculated on the CPU using MATLAB, while dashed symbols are processes calculated in parallel on the GPU using CUDA.

array position and poorly from the next. However, taking the maximum amplitude can result in increased noise if there is an image artefact or high amplitude noise present in one image and not in the other. This method also does not take into account element directivity and implicitly assumes the energy emitted by the array is uniform in all directions, which is not reflective of reality.

When stitching TFM images together, a decision has to be made on whether to stitch the images before or after normalisation. Stitching unscaled images is desirable to enable the stitched image to be normalised to a single value, however in the case of surface imaging where the amplitude of the inclined region is low compared to planar regions, stitching the unscaled images results in a loss of signal around the peak and steeply inclined regions. When considering interior imaging, unscaled images must be stitched to ensure defects are on the same amplitude scale to allow accurate characterisation to take place.

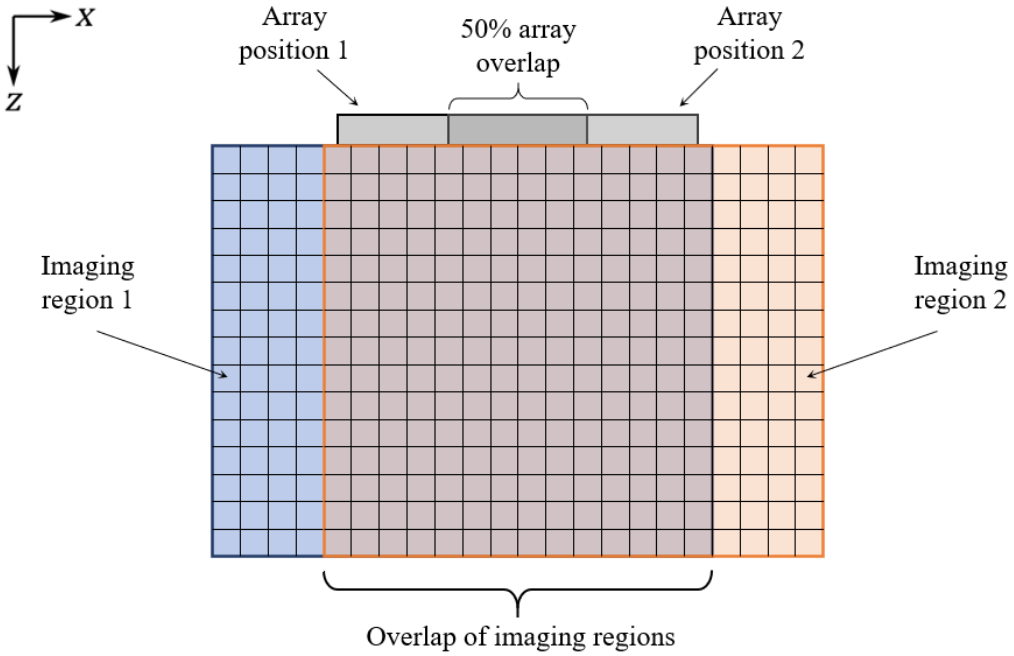

FIGURE 4.3. 2D schematic of overlapping imaging regions for two array positions using 50% array overlap.

4.2.2 Surface validation

Comparison of the extracted surface with Eq. (3.6) is valid only so long as the machined surface is actually represented by the equation. This issue was investigated by taking a laser scan of the surface of the specimen using a FARO ScanArm and directly comparing it to the surface equation. The ScanArm is able to obtain micron-level precision 3D measurements, and is therefore a useful tool in this comparison. A point-cloud scan of the specimen's surface was obtained and then compared to the surface equation. However, before a comparison could be done, the misalignment of reference frames that

was mentioned in the previous chapter needed to be addressed. This challenge was overcome by using an evolutionary algorithm to translate and rotate the scanned surface points to a position that minimises the RMSE between the surface and Eq. (3.6).

Evolutionary algorithms are metaheuristic optimisation algorithms which aim to solve a problem by applying mechanisms inspired by the theory of evolution by natural selection [61]. These types of algorithms work by iteratively trying to improve a candidate solution to a problem by evaluating the performance of a population of solutions, selecting the most successful solutions for reproduction and breeding them through mutation, recombination and selection. The offspring solutions are then evaluated and the process repeats until a set criterion is met. There are many types of evolutionary algorithms, but the one chosen to implement here is termed differential evolution (DE) and a detailed overview of how it is implemented is given in Appendix A. DE is best suited to numerical optimisation using vector differences which makes it desirable for obtaining the solution that minimises the RMSE [62].

The DE algorithm takes a vector input containing defined lower and upper bounds for each parameter of the problem and outputs another vector, termed the agent vector, that yields the best values of each parameter that minimises the RMSE between the scanned surface and Eq. (3.6). In this case the parameters are translations in the x, y and z directions, in addition to rotations around the x and y axes. Rotation around the z axis is ignored as the surface is symmetric around z at the peak. After implementing the DE algorithm and applying the agent vector to the laser scanned surface, the accuracy of the machined surface compared to Eq. (3.6) can be investigated. Fig. 4.4 shows the associated positional error in z, ΔZ, between the surfaces. The surface notch is visible at $(0,95)$ mm, and in order to avoid it and spurious signals around the perimeter of the specimen skewing the results, when calculating the RMSE only surface points within a 90 mm radius, outlined by the red dashed line, from the peak were considered. The RMSE between the surfaces was found to be 0.053 mm, which is sufficiently small enough to confidently allow the extracted surface profile to be directly compared to Eq. (3.6). The machining marks that are visible in Fig. 4.4 are also able to be seen by eye on the specimen. By comparing directly to the equation, the chances of introducing errors from the laser scanned surface are eliminated as no interpolation is required to align the point-clouds of the ultrasonically extracted and laser scanned surfaces.

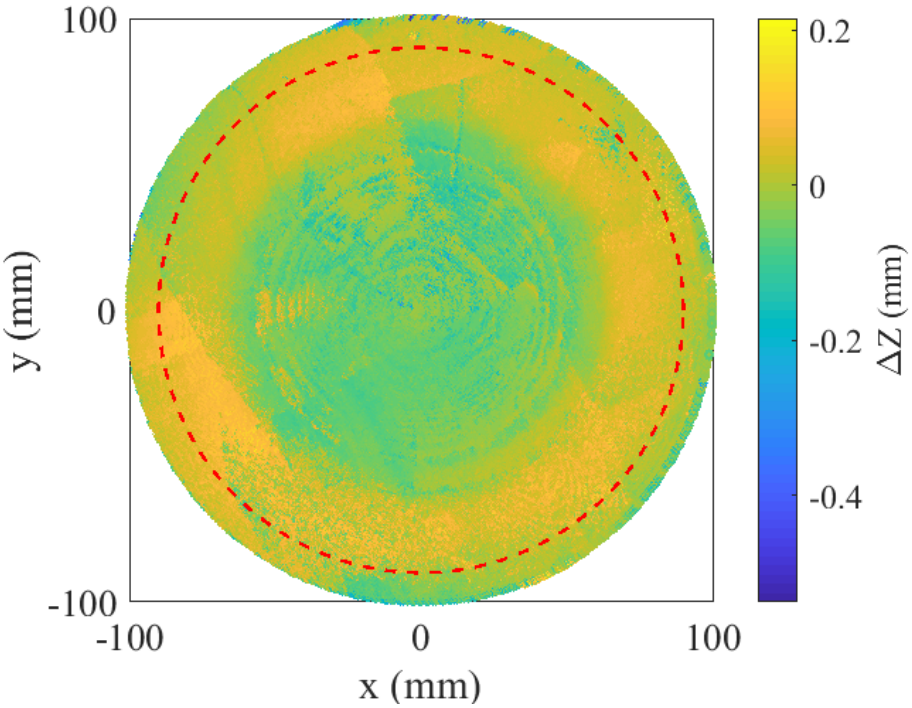

FIGURE 4.4. Associated position errors in z, ΔZ, between the equation of the surface and a laser scan of doubly curved specimen #1. The dashed red line is plotted at a radius of 90 mm from the peak.

4.3 Surface imaging and extraction

After each data set was processed for surface imaging using Eq. (2.1) and normalised using localised maxima in the front wall signals, the next step involved stitching the 3D TFM images together using the method outlined in section 4.2.1. The result is plotted in Fig. 4.5 as an isosurface at –10 dB and coloured according to z depth beneath the array, which was located at $z = 0$ mm. The visible gridded appearance in the plot is due to the stitching algorithm, whereby the maximum amplitudes of image points in the overlapped regions are taken as the true amplitudes. The x and y lengths of the imaging region for each array position were twice the diameter of the array, and so the presence of imaging artefacts in overlapped regions results in a slightly distorted image. Each data set was filtered at $f_c/3$, and a small amount of surface noise is shown in the $(x-z)$ image of the stitched surface that is viewed along $y = -100$ mm in Fig. 4.5(b). This filter frequency was chosen through trial and error to reduce the appearance of artefacts in the water, while maintaining a strong front wall response in the TFM image to allow surface extraction.

The surface extraction method implemented on the stitched 3D TFM image is the same as was described in section 3.4 for a single array position. As the resolution of surface points is $\lambda_1/2$ = 0.25 mm, the extracted surface looks almost identical to Fig. 4.5(a) and is therefore not shown. The accuracy of the surface extraction algorithm was then compared using Eq. (3.6) after applying the DE algorithm to align the reference frames by minimising the RMSE. The result of this comparison for each surface location is shown in Fig. 4.6(a) where ΔZ is the difference in z locations between Eq. (3.6) and Z_{ij} for each (x, y) surface point. The gridded appearance is visible but has not affected surface extraction. The RMSE within the 90 mm radius of the peak was found to be 0.042 mm and a histogram of ΔZ values is given in Fig. 4.6(b). This shows a normal distribution of ΔZ values around a mean of 0.89 µm with a standard deviation, σ, of 0.042 mm, which implies the surface has been accurately extracted.

Using a surface resolution of $\lambda_1/2$, the time to process all data sets was 1520 s, or approximately 8 s per data set including transfer time with 4.8 million voxels in each TFM image.

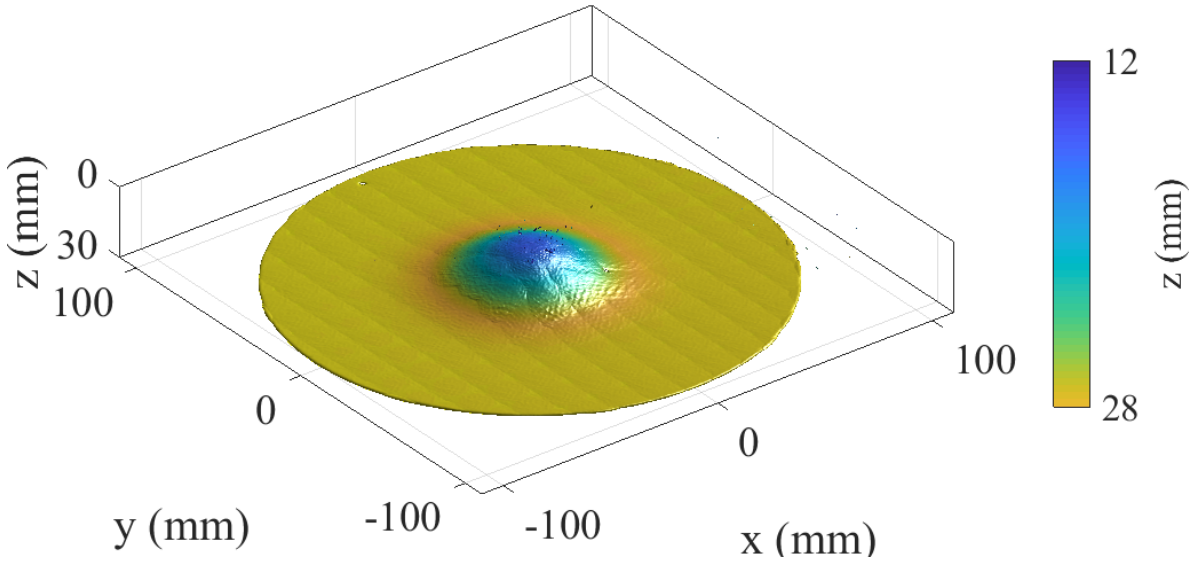

(a)

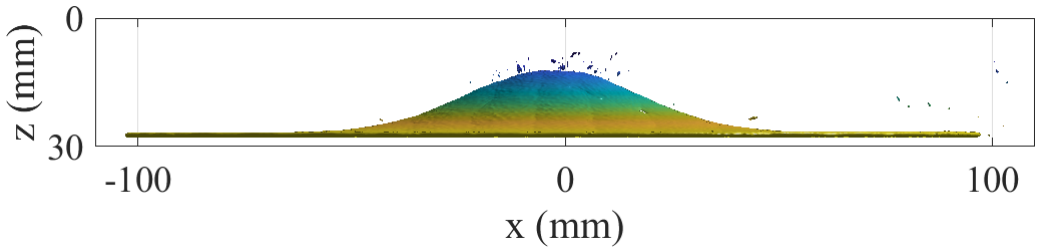

(b)

FIGURE 4.5. Stitched 3D surface TFM image of doubly curved specimen #1 plotted as an isosurface at -10 dB realtive to the maximum amplitude in the surface. (a) shows a 3D view while (b) shows the $(x-z)$ plane viewed along $y = -100$ mm.

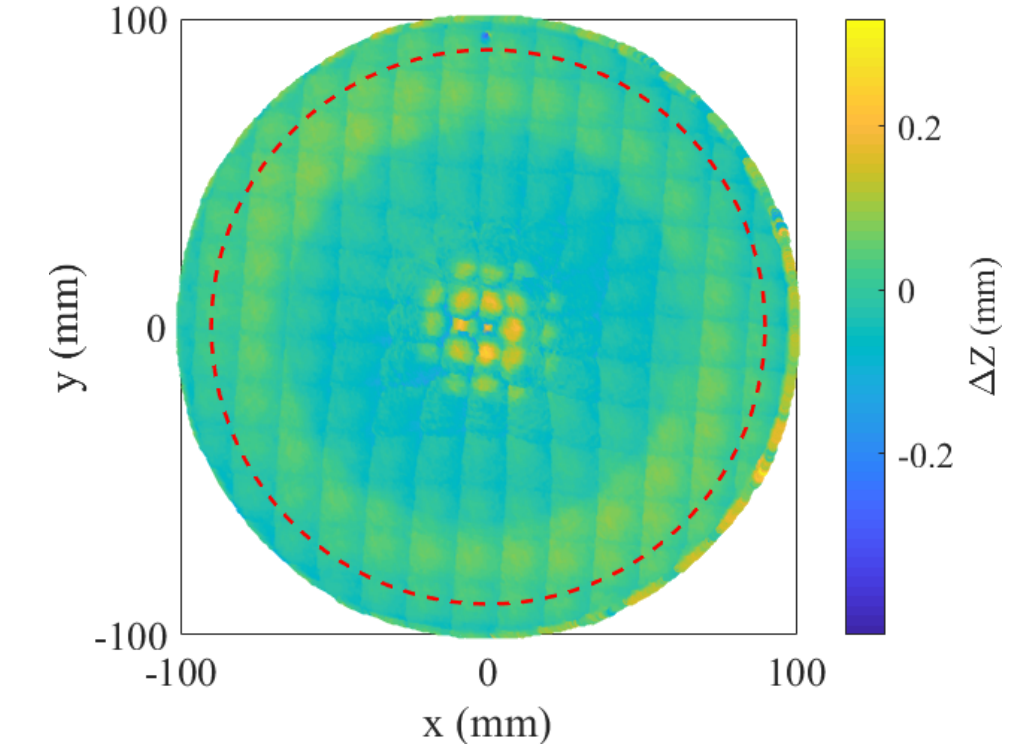

(a)

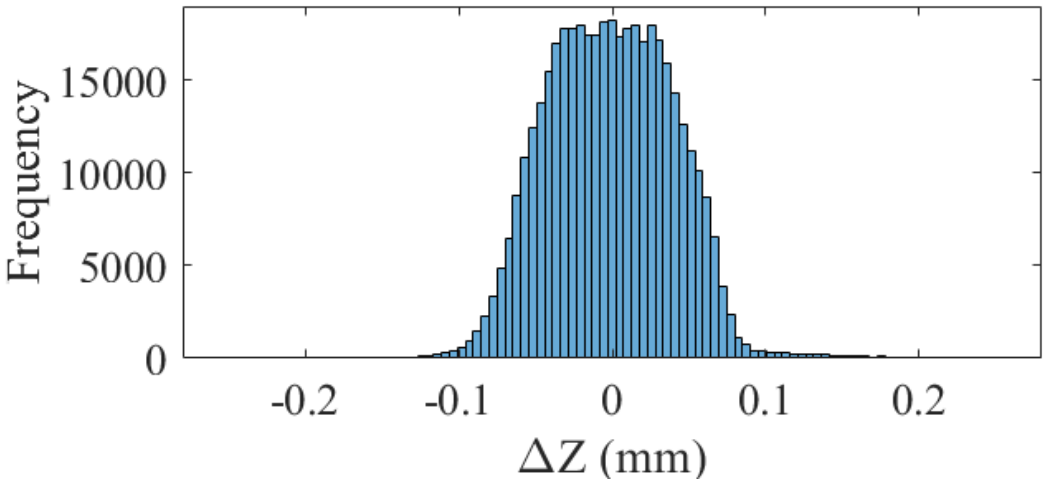

(b)

FIGURE 4.6. Comparison of the ultrasonically-extracted surface of doubly curved specimen #1 with the equation of the surface is shown in (a). (b) is a histogram showing the spread of ΔZ. Only ΔZ values within a 90 mm radius from the peak, shown by the red circle, are considered when calculating the RMSE.

4.4 Interior imaging

When tackling interior imaging using such a large surface, it would be impractical to consider every surface point as a potential surface-crossing location when determining minimum ToFs. The shortest ray paths from an array positioned at $(0,-100,0)$ mm are clearly not going to travel through surface points in the $(0,100,Z_{0,100})$ mm region when imaging a grid of points directly beneath the array, so an additional step needs to be included to reduce the number of surface points considered when determining the surface-crossing locations. An illustration of this is given in Fig. 4.7, whereby the array position outlined by the black dashed circle (covering an area of $15^2\pi$ mm^2) only considers the 47,000 surface points contained within the red circle ($30^2\pi$ mm^2) when imaging directly beneath the array instead of all 524,000 points in the entire extracted surface ($100^2\pi$ mm^2). The area enclosed by the red circle is 4 times larger than the area of the array footprint (and 9% of the total specimen surface area) in order to include surface points that do not lie directly below the array footprint and to allow for surface variations; depending on the relative height of the surface in a particular area and interior volume to be imaged, the optimal ray path could travel through a surface point that would not be considered if only surface points in an area equal to and directly beneath the array footprint area was considered. The radius of the red circle was taken to be double the radius of the array footprint to allow more surface points to be included without significantly slowing down the imaging process. The surface points are coloured according to distance in z below the array (located at $z = 0$ mm). The subsection of surface points considered should be selected according to the location to be imaged.

Interior TFM images are then generated using Eq. (2.4) with subsections of the extracted surface. The interior imaging volume contained 1.8 million voxels at a resolution of $\lambda_2/4$, or half the diffraction limit, and each array position used an average of 35,000 surface points. The imaging grid length in x and y was set to twice the array diameter, centered on the mean element location, as for some array positions the elements are more sensitive to locations not directly beneath them, or because the array-surface orientation reflects the majority of the energy from the surface instead of transmitting it. This behaviour is explored in further detail in the next chapter. For this reason the imaging grid is large, but any larger would result in significantly slower processing times. The processing time for this stage was 6 hours including transfer times, which equates to approximately 2 minutes per array position. It is important to note that the method described here is a brute force approach, whereby every surface point is considered when

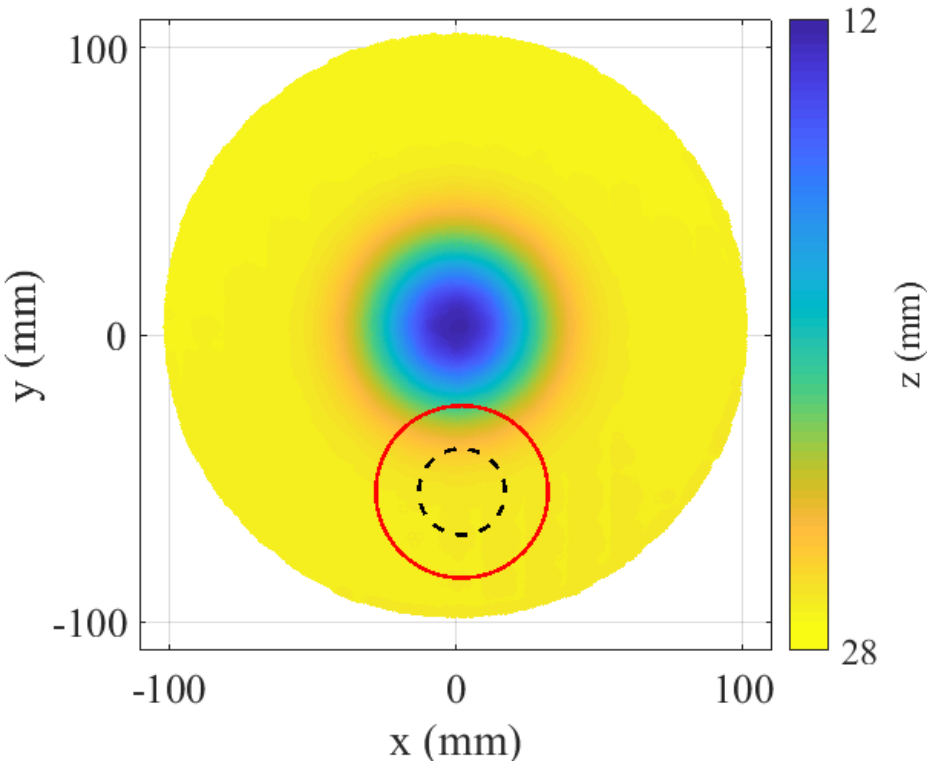

FIGURE 4.7. Illustration of a subsection of the extracted surface points, enclosed by the red circle, used when imaging beneath the array position shown by the dashed black circle. Surface points are coloured according to distance in z below the array.

calculating ToFs. This approach relies on sheer computing power to process all possible paths rather than employing advanced techniques to make the imaging more efficient. A potential solution to reduce the number of image voxels would be to firstly image a coarse grid using randomly selected surface points; over a set number of iterations, the regions of higher amplitude in the images can be honed in on and can be imaged again with a finer resolution. However, the coarse grid will still have to be fine enough to guarantee a defect is not missed.

The interior TFM images are stitched using the procedure described in section 4.2.1 before being normalised using the maximum amplitude across all back wall signals. The resulting stitched 3D interior TFM image is shown in Fig. 4.8 plotted at –24 dB relative to, or approximately 6% of, the maximum amplitude in the back wall and coloured according to distance in z below the array. The peak of the surface is not visible as the isosurface is plotted at a single contour level and due to the surface inclination

angle and the orientation of the array, the amplitude of the inclined surface regions are much lower than that of the flat regions. Snapshots of individual defects can also be obtained by creating a window around volumes in the TFM image. Snapshots of BDHs K, L and M are shown in Fig. 4.9 and EDM notches 4, 3 and 2 are shown in Fig. 4.10. It was found that the defects located under the region of steep inclination are unable to be imaged at any reasonable amplitude level, as is evident by the gap in the isosurface plots of EDM notches 3 and 4. For this reason, BDHs B, F, J, N and R are excluded from the results. BDHs A and C are also excluded as their SNR is too low for imaging. The central location of each BDH and EDM notch was found by taking the mean location of points whose amplitudes were greater than 6 dB below the local maximum amplitude. Each defect is plotted at its central location using isosurfaces at different amplitude levels relative to the maximum amplitude in the back wall.

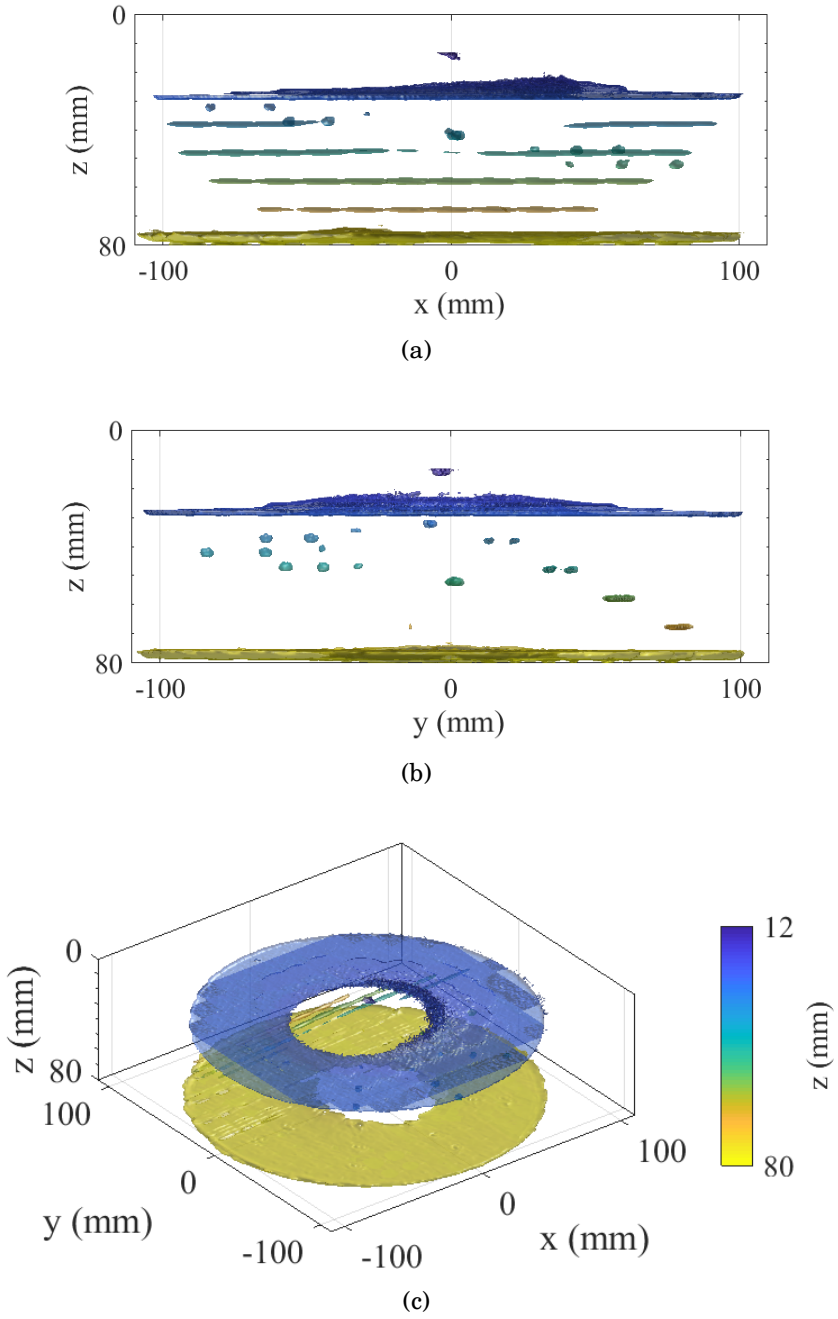

FIGURE 4.8. Stitched 3D interior TFM image of the doubly curved specimen #1 plotted as an isosurface at –24 dB relative to the maximum amplitude in the back wall and coloured according to distance in z. (a) and (b) show elevations, while (c) shows a 3D view.

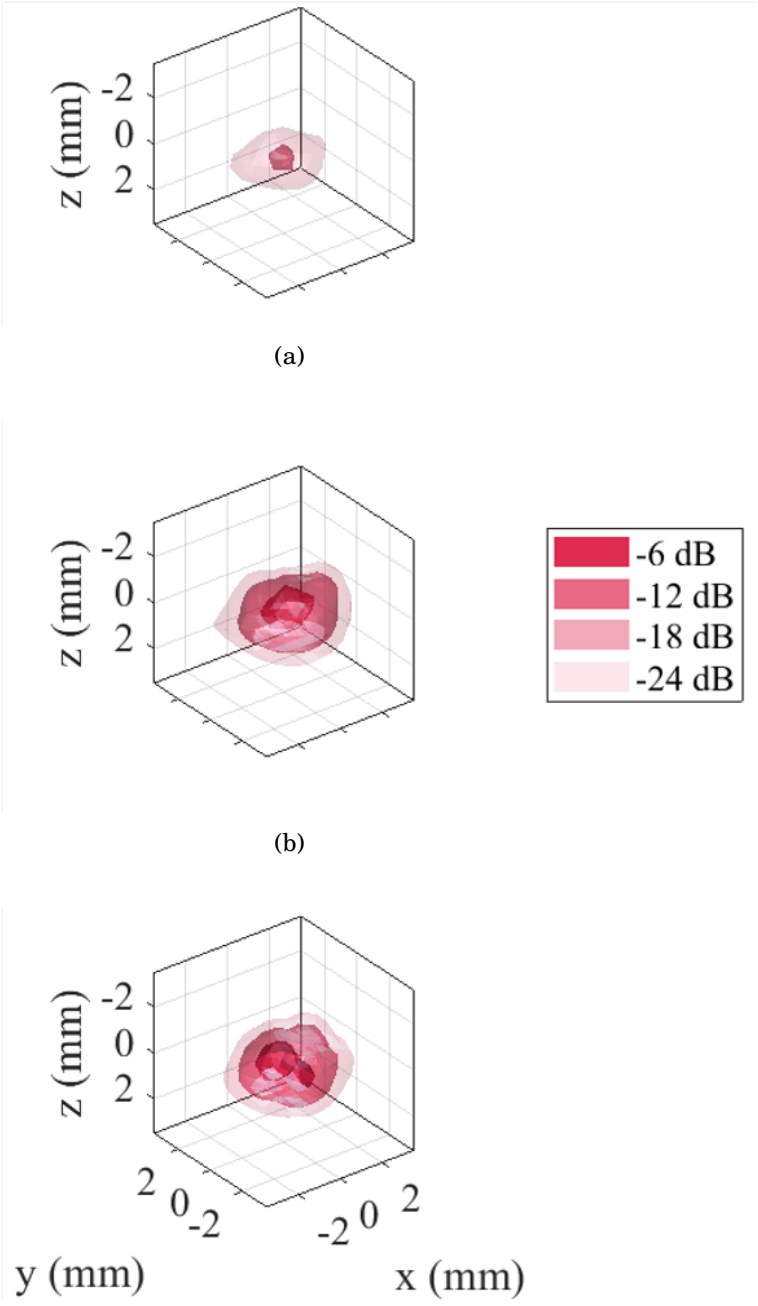

FIGURE 4.9. Zoomed in snapshots of BDHs (a) K, (b) L and (c) M plotted at nominal positions. dB scale relative to the maximum amplitude in the back wall.

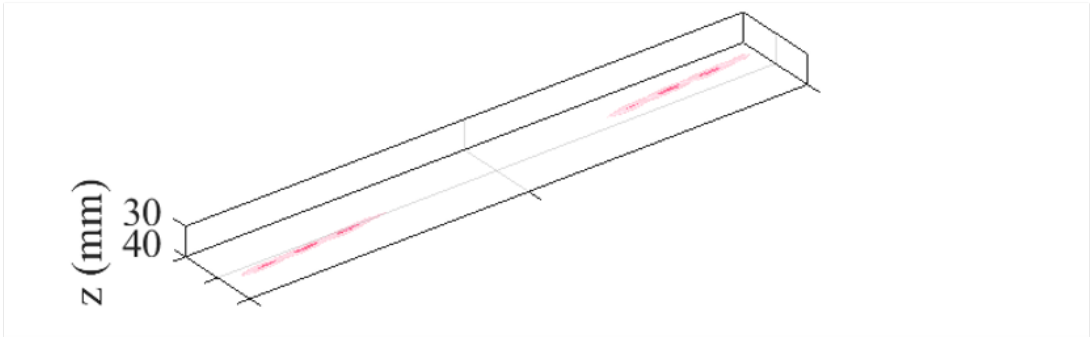

(a)

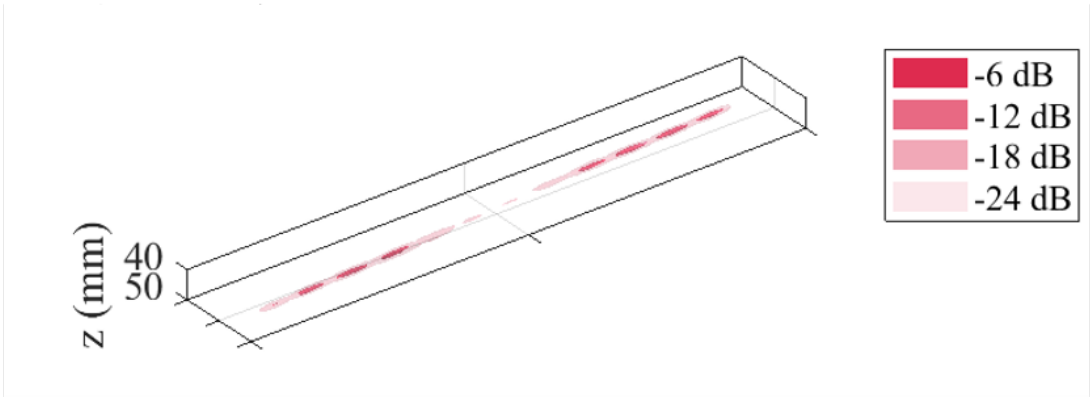

(b)

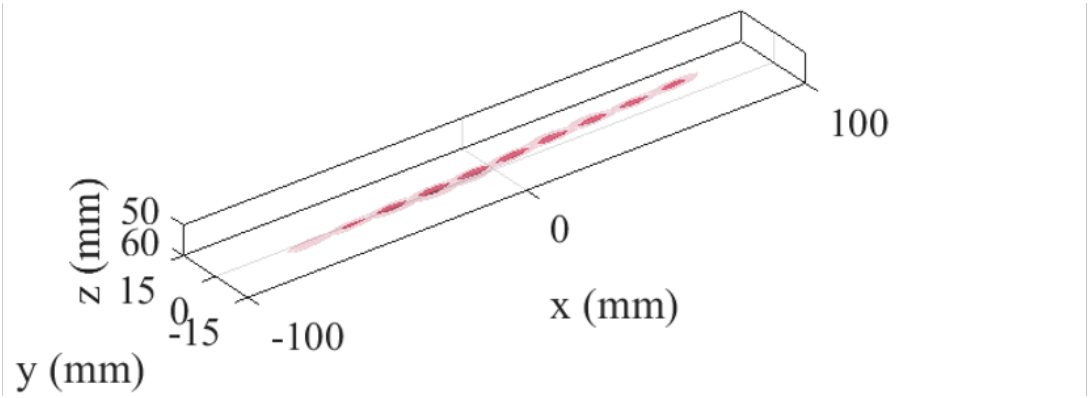

(c)

FIGURE 4.10. Zoomed in snapshots of EDM notches (a) 4, (b) 3 and (c) 2 plotted at nominal positions. dB scale relative to the maximum amplitude in the back wall.

Of the defects that were able to be imaged, their positions were investigated and compared to the machined locations using their centre points. This was achieved using two metrics: the first is the depth above the back wall and the second is the lateral distance from the surface notch. These distances are then compared to the true values from the specimen design file, with the results shown in Fig. 4.11. It was found that σ of the depth and lateral distance comparisons were 0.571 mm and 1.01 mm respectively. Both values are comparable to $\lambda_2/2$ = 1.05 mm and so the measured defect locations are in good agreement with the true positions.

From observing the result in Fig. 4.8, it is evident that some defects are visible, while others are not; Fig. 4.11 shows that the defects that *are* able to be imaged appear in their intended locations and the surface is being accounted for correctly. Further investigation into why some defects were unable to be imaged is as follows. Fig. 4.12 shows the surface inclination across all surface points along with the machined positions of defects; the visible defects are coloured red, while the defects that were unable to be imaged are shown in white. The figure shows defects under the region of the surface with an approximate inclination larger than the longitudinal critical angle for a wave travelling from water to aluminium, $\theta_c = 13.4°$, proved impossible to image using this setup orientation. EDM notch 4, shown in Fig. 4.10(a), illustrates this as there is a gap in the isosurface as part of the notch is underneath the region of highest inclination. The BDHs that were unable to be imaged include BDHs B, F, J, N and R, along with BDHs A and C due to their low SNR and are coloured white in the figure. BDH A is excluded as it is 5 mm directly under the peak and interior reflections in this area have buried the defect response in noise. The reason for low SNR on BDH C is due to it lying on the radial arm that was drilled at the smallest depth below the surface. The reason for the other defects not being imaged is due to several factors.

Firstly, consider the surface to be an inclined plane with a steepest angle of 24° and the array positioned directly above it, as depicted in Fig. 4.13. In the region of the sample directly under the array, the majority of the incident energy is reflected due to the surface angle being larger than θ_c. To the side of the array further up the plane, there is a region where rays from the array are incident on the surface below θ_c, shown in red in Fig. 4.13 where $\theta_i < \theta_c$. However, the directivity amplitude of the elements in the array means that there is low transmission and reception sensitivity in these directions as they are at relatively large angles relative to the array normal. Fig. 4.14 shows the directivity, $D(\phi)$, of a 1.7 mm diameter circular element radiating into

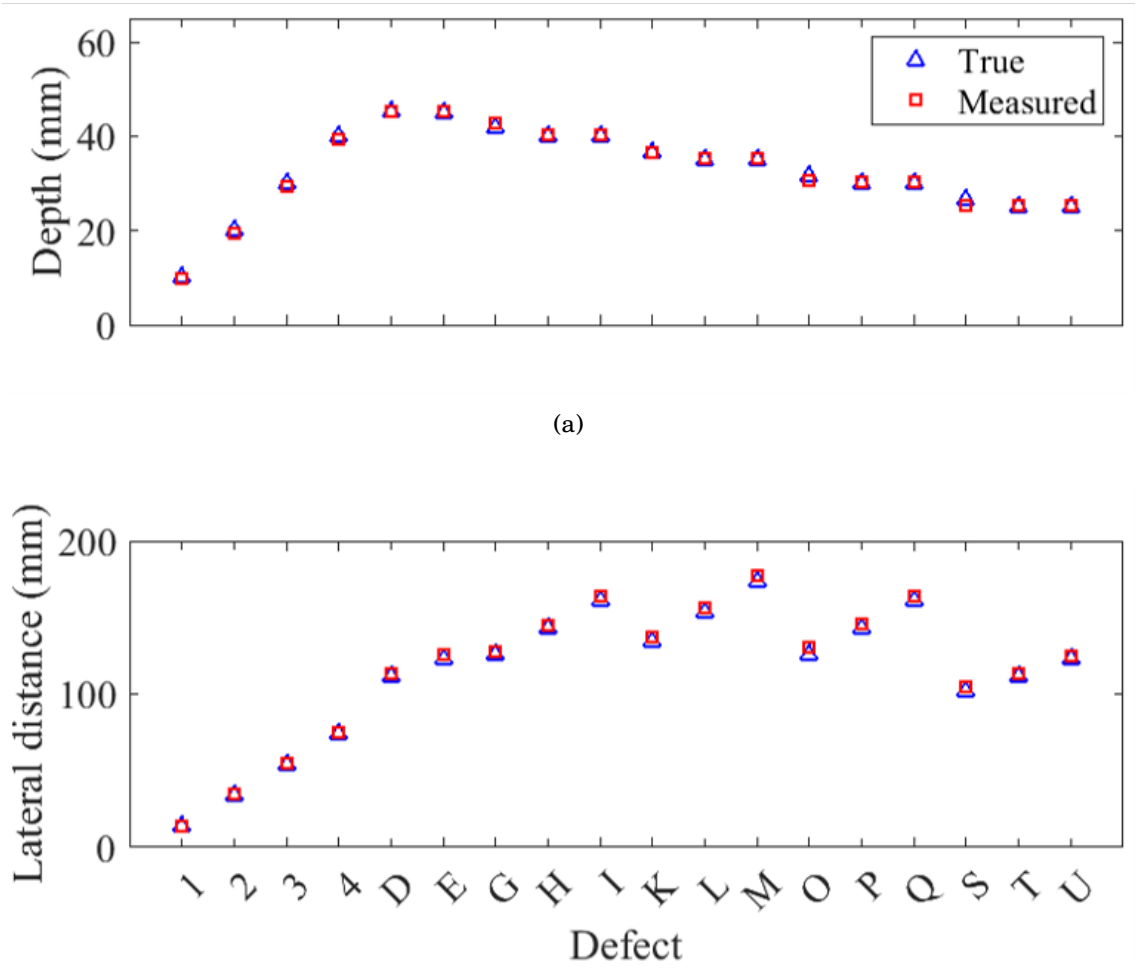

FIGURE 4.11. Comparison of measured and true defect positions. (a) Shows the comparison of the depth of the defects above the back wall of the specimen and (b) shows the comparison of lateral defect distance from the surface notch.

water at 3 MHz, calculated using

$$D(\phi) = \frac{2J_1\left(kb\,\sin\phi\right)}{kb\,\sin\phi} \tag{4.2}$$

from [63] where J_1 is the 1st order Bessel function, k is the wavenumber, b is the element radius and ϕ is the elevation angle relative to the element normal. As the element emits radiation equally in all azimuthal directions, the directivity pattern is symmetric around

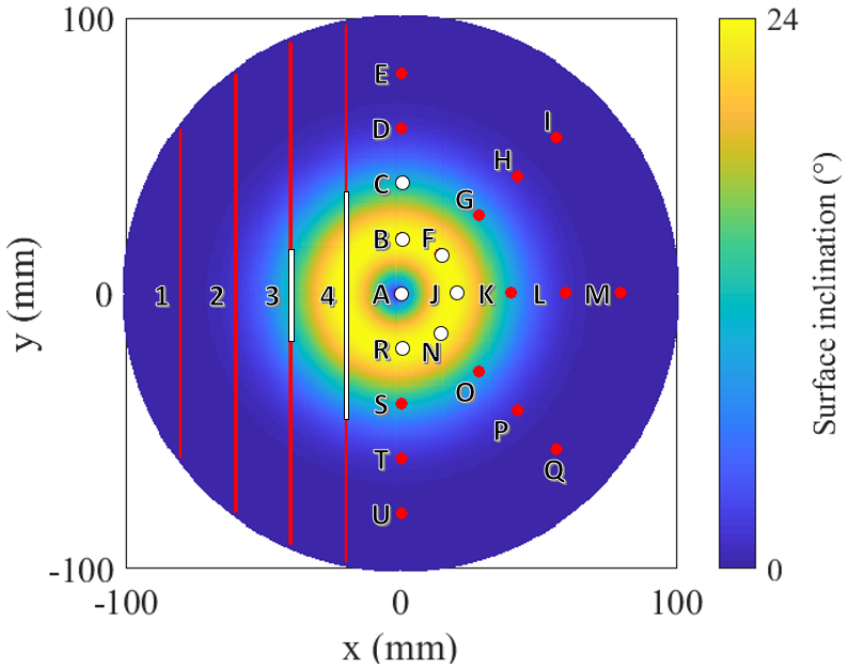

FIGURE 4.12. Surface inclination with the locations of the EDM notches and BDHs marked. White circles represent defects that were unable to imaged and white lines represent portions of EDM notches that were unable to be imaged.

the element normal. $D(\phi)$ represents the directivity on transmission and reception, so to obtain the total directivity for a transmit-receive element pair their individual directivities at the respective angles are calculated and multiplied together. The array elements' highest sensitivity is at 0°, which corresponds to the direction directly beneath the element. For a planar surface parallel to the base of the array, the directivity of the elements is therefore the highest, as shown in the $\pm\,\theta_c$ range by the solid blue line in Fig. 4.14. However, for a surface inclination of 24°, as shown by the dashed red region of the graph, the directivity within the 24° $\pm\,\theta_c$ range is much lower. For this surface inclination the elements have reduced sensitivity to any signals entering or leaving the specimen. The ratio of the average directivity in the parallel surface case when compared to the inclined surface case is approximately 20:1. By examining BDHs K, L and M in Fig. 5.8(a), 5.8(b) and 5.8(c) respectively, this effect is evident as the average amplitude in BDH K is approximately 10 dB, or 33%, lower than that in BDHs L and M, illustrating that defects located under the inclined region have lower amplitudes when compared to defects located under a planar surface parallel to the array.

It is important to note that this imaging limitation is due to the experimental setup, whereby the array was aligned parallel to the back wall of the specimen. If the array was rotated to align with a tangent to the inclined region then in theory imaging ability would increase. This would require a scanning system with 2 more degrees of freedom; inspections with six-axis robots which are able to accomplish scans like this are becoming increasingly common in NDT [57, 64–66].

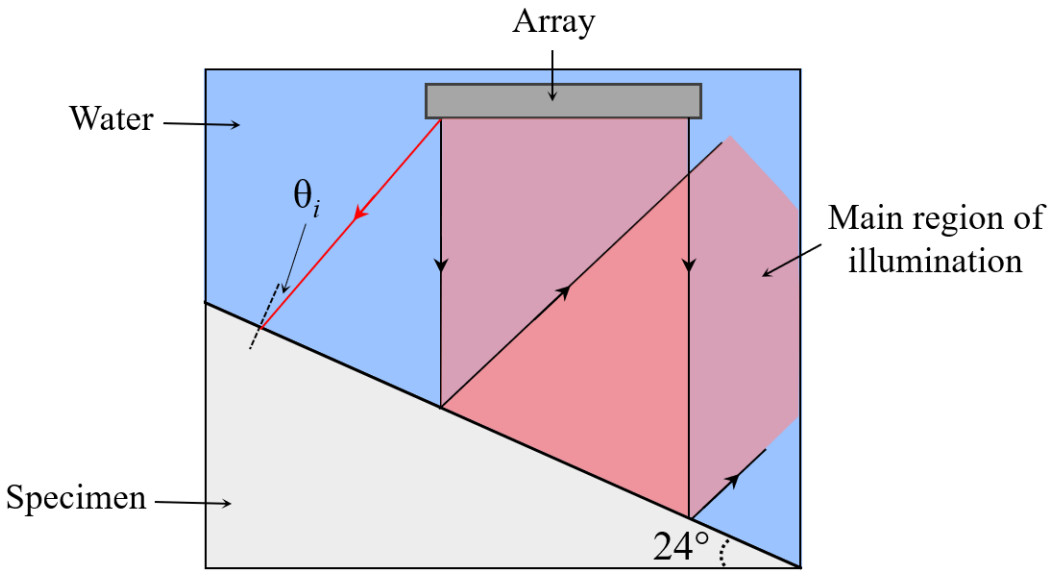

FIGURE 4.13. Illustration of reflection of sound energy when incident on a plane greater than the critical angle, θ_c. The red line represents a wave incident on the plane at θ_i, where $\theta_i < \theta_c$.

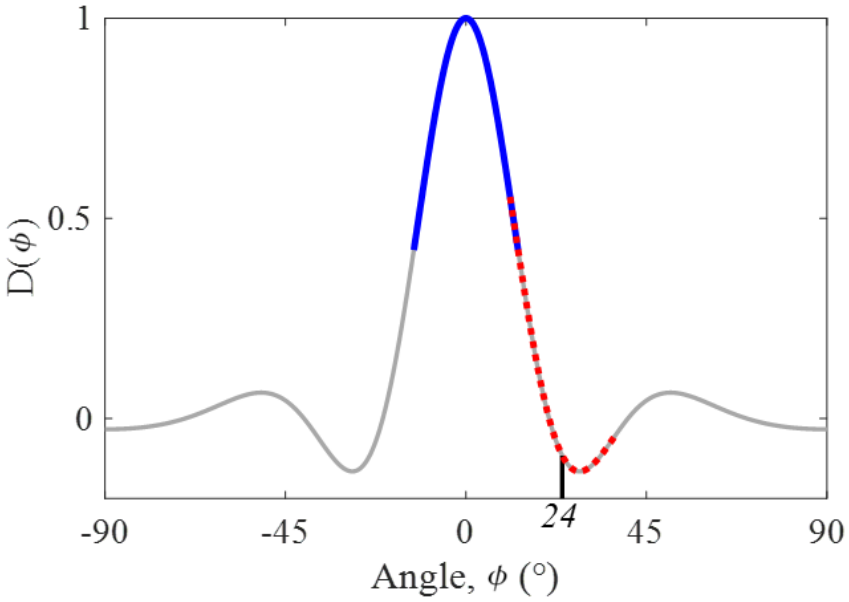

FIGURE 4.14. The directivity of a 1.7 mm diameter circular element radiating into water at 3 MHz as a function of angle relative to the element normal direction. The solid blue region is the range $\pm\theta_c$ and the dashed red region is the range $24° \pm \theta_c$.

4.5 Summary

Scanned arrays are becoming more popular in industry due to their ability to quickly scan large components and potentially improve the characterisation of defects by probing from an increased number of angles. In this chapter, a sparse 2D array was scanned over the surface of a specimen with a doubly curved surface profile that was unknown *a priori*. A stitching method was implemented to combine the surface images generated from each array position into a single, larger 3D TFM image before a surface extraction algorithm was applied. By comparing the ultrasonically-extracted surface with the true equation of the surface, it was found that the surface extraction algorithm produced a surface that was in excellent agreement with the machined surface. Subsections of the extracted surface points were then used to generate interior TFM images to avoid excessive processing times. The positioning of machined defects within the specimen was then investigated; defects that were able to be imaged appeared in the correct locations, while defects located under relatively steep inclined surface regions proved impossible to image with the current setup. Up to this point the elements in the sparse 2D array have be assumed to act as ideal point sources, which is not representative of their true nature. The energy of the ultrasonic beam excited by the array transducer at different angles is not uniform, so as the relative geometrical position between a defect and the array aperture is different, different amplitude results will be obtained for identical defects. This effect was pronounced when defects beneath steep surface angles were unable to be imaged, even though some ray paths were able to pass through the surface at larger angles relative to the element normals. This will be the focus of the following chapter.

Chapter 5

3D sensitivity images

When a sound wave is incident on the surface of a specimen, the nature of the interaction is complex due to surface geometry, incident angle, and relative material impedance. This means that the amplitude and angle of energy transmitted into a specimen differs as an array is scanned across a non-planar surface. Consequently, a region of the interior of the specimen may be viewed well from one array position, and poorly from the next. This effect is termed the sensitivity of the region of interest to an array position and can be displayed in a sensitivity image [67]. Sensitivity images can quantitatively determine which array positions yield a strong amplitude for a given setup and are therefore a useful tool when processing data from a scanned array. They have been used in multi-view array inspection, whereby each combination of wave modes have different sensitivities depending on angle and amplitude [68], and data fusion, which aims to combine valuable information from numerous multi-view images into a single image [69].

In the previous chapter, the true amplitudes of voxels imaged from more than one array position were obtained by taking the maximum amplitude values across all images. The method assumes uniform sensitivity throughout the TFM images, and so if there is an artefact in a region of low sensitivity, the signal from the artefact can be misidentified as a defect signal and result in an inaccurate final image. An alternative stitching method is proposed in this chapter, whereby the amplitude of a voxel is the sum of the individual weighted TFM amplitudes obtained from each array position. This chapter focuses on the generation of sensitivity images and their implementation in an alternative stitching algorithm.

5.1 Sensitivity image generation

A 2D model developed in [68] provides an estimate of the TFM intensity a particular defect would yield for a specific setup. By assuming the sound energy is incident at a single frequency, ω_0, and the amplitude at the defect centre is representative of the true peak amplitude (as is the case for small defects), a time efficient method was introduced when compared to a multi-frequency model or a finite element analysis implementation. The contributions to the model can be separated into three main sections for an immersion setup: the first considers the transmit path from the element to the scatterer through the surface, the second is the calculation of the scattering and the final section is the receive path from the scatterer to the receiving element through the surface. The incident pulse amplitude on the scatterer is always less than the initial amplitude emitted from the source element due to amplitude loss through geometrical attenuation effects and transmission across an interface. Additional amplitude is lost during the scattering stage, where the scattering is dependent on the nature of the defect and the incident angle. Furthermore, the amplitude of the reflected signal is decreased by returning across the specimen's surface to the receiving element. The model accounts for these losses of signal amplitude, along with the contribution of the element directivity. Effects from material attenuation are assumed here to be negligible, although they can easily be included in the same framework if they are significant. The equation to generate a sensitivity image intensity, $E(\mathbf{P})$, is defined for small defects located at vector positions $\mathbf{P}$ by:

$$E(\mathbf{P}) = \left| \sum_T \sum_R a_{T,R}(\mathbf{P}) C_{T,R}(\omega_0, \mathbf{P}) \right|, \tag{5.1}$$

where T and R are the transmitting and receiving element indices respectively, $a_{T,R}$ is the optional weighting factor that is used in the TFM imaging algorithm in Eq. (2.4) (unused in the current work, so therefore set equal to 1) and

$$C_{T,R}(\omega_0, \mathbf{P}) = B_T(\mathbf{P}) B'_R(\mathbf{P}) D_T(\omega_0, \mathbf{P}) D'_R(\omega_0, \mathbf{P}) \Gamma_T(\mathbf{P}) \Gamma'_R(\mathbf{P}) S_{T,R}(\omega_0, \mathbf{P}), \tag{5.2}$$

where

- B_T and B'_R represent the geometrical attenuation, or beamspread, for the transmit and receive paths;

- D_T and D'_R represent the element directivity functions for the transmit and receive paths;
- Γ_T and Γ'_R describe the transmission coefficients of the transmitted and received waves when passing through the surface;
- $S_{T,R}$ is the angular-dependent response, or scattering matrix, of the imaged defect.

Note the similarity of Eq. (5.1) with Eq. (2.4); the time-domain signal $h_{T,R}$ has been replaced with a prediction of the amplitude of the response from a scatterer at position $\mathbf{P}$. Further descriptions of the terms in Eq. (5.2) are given below.

5.1.1 Ray tracing

The nature of a non-planar surface means that the surface normal and array normal are not parallel, so care must be taken when determining incident angles on the surface.

Consider the transmit path shown in Fig. 5.1. When computing ray-tracing for TFM imaging, only the position of the surface-crossing point, $\mathbf{A}_T$, is needed to determine the minimum ToF. However, when considering the effects of beamspread and transmission, more information needs to be known. Specifically, the angles of incidence and transmission for an incoming ray. In the case of a planar surface where the array is parallel to the surface, determining the angle of incidence, θ_i, is straightforward using trigonometry and equal to the transmitted angle from the element, ϕ. However, when a non-planar surface is considered, or when the array is tilted with respect to a planar surface, the surface and array normals are no longer parallel and the normal vector to the surface at $\mathbf{A}_T$, $\mathbf{N}_T$, needs to be determined.

In 2D, it is relatively straightforward to estimate the surface normal at a point on a surface defined by a line of points. By using i to denote the index in the x direction of $\mathbf{A}_T$, a straight line can be defined between the two neighbouring surface points at $(i-1)$ and $(i+1)$. The equation of the line normal to this is easily obtained. In 3D, determining the normal to a surface is more complex. The method involves averaging the surface normals calculated using $\mathbf{A}_T$ and its 8 nearest neighbours, as illustrated in Fig. 5.2. By denoting j as the surface-crossing point index of $\mathbf{A}_T$ in the y direction and ignoring the z axis for now, $\mathbf{A}_T$ is defined to be located at (i,j). Starting with the surface point at $(i-1,j-1)$, the associated vector between this point and $\mathbf{A}_T$ is found. Travelling

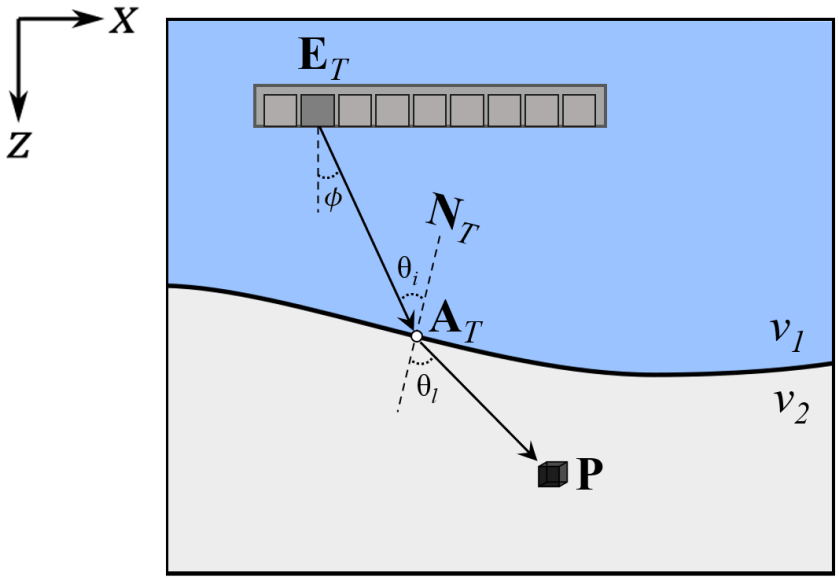

FIGURE 5.1. Illustration of an incident and transmitted angle on a non-planar surface between element $\mathbf{E}_T$ and image point $\mathbf{P}$. $\mathbf{N}_T$ is the vector of the normal to the surface at surface-crossing location $\mathbf{A}_T$, ϕ is the transmitted angle from the element normal, θ_i is the angle of incidence on the surface and θ_l is the longitudinal angle of transmission in the specimen. v_1 and v_2 are the velocities of sound in water and the specimen respectively.

clockwise, the vector between $\mathbf{A}_T$ and the surface point at $(i-1, j)$ is found, and so on. The process is repeated until the vector between $(i, j-1)$ and $\mathbf{A}_T$ is determined. Then, going clockwise again around the nearest neighbours, the cross-product of the vectors $\mathbf{a}$ and $\mathbf{b}$ of each sequential pair of neighbouring points are calculated using

$$\mathbf{a} \times \mathbf{b} = ||\mathbf{a}||\ ||\mathbf{b}||\ \sin(\theta_{ab})\ \hat{\mathbf{k}}, \tag{5.3}$$

where θ_{ab} is the angle subtended between $\mathbf{a}$ and $\mathbf{b}$, and $\hat{\mathbf{k}}$ is a unit vector perpendicular to the plane containing $\mathbf{a}$ and $\mathbf{b}$. This results in 7 values of $\mathbf{k}$, which are then averaged to give $\mathbf{N}_T$. In the case where $\mathbf{A}_T$ is an edge point in the surface, only neighbouring points which exist are considered, i.e. the surface is not expanded using extrapolation. The angle of incidence, θ_i, can then be calculated by using the dot product of the incident ray, $\boldsymbol{u}$, and $\mathbf{N}_T$ using

$$\cos(\theta_i) = \frac{\boldsymbol{u} \cdot \mathbf{N}_T}{||\boldsymbol{u}||\ ||\mathbf{N}_T||}, \tag{5.4}$$

and the longitudinal transmitted angle, θ_l, is calculated using Snell's law:

$$\sin(\theta_l) = \frac{v_{2_l}}{v_1} \sin\theta_i, \tag{5.5}$$

where v_{2_l} is the longitudinal velocity of sound in the specimen. Only longitudinal wave modes are considered throughout this chapter, but the angle of the transmitted transverse wave mode, θ_t, can be considered by substituting v_{2_t} for the transverse velocity of sound in the specimen.

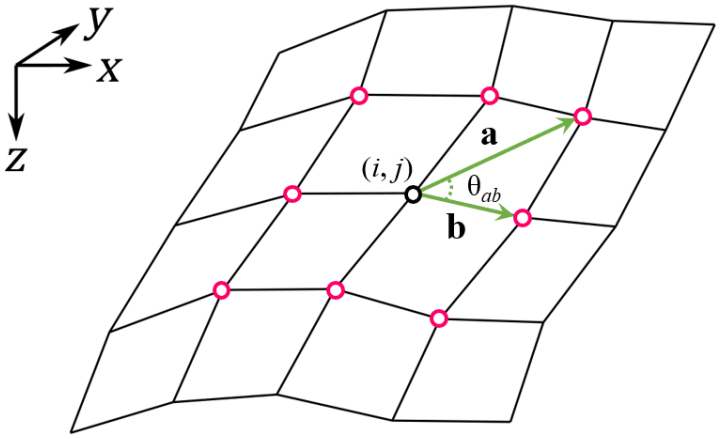

FIGURE 5.2. Surface crossing point, $\mathbf{A}_T$, shown by black dot at indices (i, j) and nearest neighbours, shown in red, that are used to calculate the surface normal in 3D. **a** and **b** are the vectors between $\mathbf{A}_T$ and surface points at indices $(i+1, j+1)$ and $(i+1, j)$ respectively. θ_{ab} is the angle subtended between **a** and **b**.

5.1.2 Beamspread coefficient

The beamspread coefficient is representative of the geometric spreading of sound energy as a result of expanding wavefronts. Ignoring attenuation effects, when an ultrasonic beam is excited from an element, assumed to be a point source in 3D, the beam spreads out in all directions equally as a spherical wave with increasing time. A 2D method for obtaining the beamspread coefficient after one transmission using a linear element is given in [68]; the 3D beamspread coefficient when using a point source was adapted from [70] and obtained through private correspondence with N. Budyn, and is calculated at point **P** by

$$B_T(\mathbf{P}) = \sqrt{\frac{1}{\left(\alpha_1 + \frac{v_{2_l}}{v_1}\alpha_2\right)\left(\alpha_1 + \frac{v_{2_l}}{v_1}\frac{\cos^2(\theta_i)}{\cos^2(\theta_l)}\alpha_2\right)}} \tag{5.6}$$

with

$$\alpha_1 = ||\mathbf{E}_T - \mathbf{A}_T|| \qquad \text{and} \qquad \alpha_2 = ||\mathbf{A}_T - \mathbf{P}||.$$

The beamspread coefficient for the return path to element R, $B'_R(\mathbf{P})$, can be obtained by making the following substitutions in Eq. (5.6):

$$\begin{aligned} \alpha_1 &\longrightarrow \alpha_2 \\ \nu_1 &\longrightarrow \nu_{2_l} \\ \nu_{2_l} &\longrightarrow \nu_1 \\ \theta_i &\longrightarrow \theta_l \\ \theta_l &\longrightarrow \theta_i. \end{aligned}$$

5.1.3 Element directivity

The directivity of a circular element in 3D can be modelled as a plane circular piston emitting radiation. In the far field approximation, the directional factor is represented by Eq. (4.2).

5.1.4 Transmission coefficient

When a ray is incident on a boundary between two media, a fraction of the energy is reflected back in the same medium as the incident wave travelled, while the rest of it gets transmitted into the other medium. Depending on the incident angle, some energy can travel on the surface of the specimen as a Rayleigh wave. The transmission coefficient, Γ, describes the amplitude of the transmitted wave with respect to the incident wave; similarly, the reflection coefficient describes the amplitude of the reflected wave in relation to the incident wave. Derivations of the transmission coefficient calculations for different conditions can be found in [71] and the key equations are given here. For a water–specimen boundary with an incident longitudinal wave in water, the transmission coefficient of the acoustic pressure is calculated using:

$$\Gamma_T = \frac{2}{M} \cos(2\theta_t) \tag{5.7}$$

with the abbreviation

$$M = \left(\frac{\nu_{2_t}}{\nu_{2_l}}\right)^2 \sin(2\theta_l) \sin(2\theta_t) + \cos^2(2\theta_t) + \frac{\rho_1 \nu_1}{\rho_2 \nu_{2_l}} \frac{\cos(\theta_l)}{\cos(\theta_i)}, \tag{5.8}$$

where ρ_1 and ρ_2 are the densities of water and the specimen respectively, and all other symbols have been previously defined.

In the case of a specimen-water boundary, as is encountered on the return path from the scatterer to the receiving element, the transmission coefficient using an incident longitudinal wave is found using:

$$\Gamma'_R = \frac{2}{M} \frac{\rho_1 v_1}{\rho_2 v_{2_l}} \frac{\cos(2\theta_t)\cos(\theta_l)}{\cos(\theta_i)} \tag{5.9}$$

where all symbols have the same meanings as before and M is from Eq. (5.8).

5.1.5 Scattering amplitude

The scattering of an ultrasonic wave by a defect is influenced by a number of factors including wave frequency, incident angle and defect size, shape, orientation and roughness. The scattering amplitude can be measured over a range of angles in what is termed a scattering matrix, or S-matrix, which is dependent upon wave frequency, incident angle and reflected angle [72]. S-matrices can be used to accurately determine the size and orientation of small, crack-like defects in 2D [73], but have yet to be fully explored in 3D. S-matrices will be discussed further in the following chapter.

With no prior knowledge about the nature of the defects expected, the most appropriate assumption is that the scatterer is assumed to behave as a point reflector with $S_{T,R} = 1$ and so only beamspread, directivity and transmission coefficients need to be considered when modelling the sensitivity image.

5.2 Single-frame application

Consider the inspection scenario described in section 2.2, where an array is used to image a specimen with a planar surface in immersion. By using the parameters of this setup (i.e. array and surface locations) and combining the contribution of B, D, Γ and S at each voxel in a defined imaging grid, Eq. (5.1) can be used to generate a sensitivity image, $E(\mathbf{P})$. Fig. 5.3 shows the 3D sensitivity image obtained of the interior of the specimen, where the amplitudes have been normalised between 0 and 1. The array is positioned at $z = 0$ mm. Individual $(x-z)$ 2D planes of $E(\mathbf{P})$ at increasing steps along the y axis are also shown in Fig. 5.4. The figures show that sensitivity is not uniform throughout the imaging region; the array is most sensitive to the the region directly beneath it. For all z distances, as the x and y distances increase or decrease, the expected amplitude from a point target is minimised. If the dominant source of noise is uniform

amplitude uncorrelated random noise throughout the raw HMC data, then the resulting TFM image with $a_{T,R} = 1$ will also have uniform noise. Therefore, the 3D TFM image has non-uniform sensitivity but uniform noise. The normalised TFM image, $I'(\mathbf{P})$, is obtained using

$$I'(\mathbf{P}) = \frac{I(\mathbf{P})}{E(\mathbf{P})}. \tag{5.10}$$

Weighing a TFM image makes the sensitivity uniform throughout the imaging region, but at the expense of non-uniform noise. This effect is from noise in areas of weak signal being amplified. The 3D TFM image in Fig. 2.6 is normalised and the result is shown in Fig. 5.5 where the dB scale is relative to the maximum amplitude of FBH 1 (the defect at the apex of the letter *A*). The time taken to generate $I'(\mathbf{P})$ using an imaging grid with 516,000 voxels and 32,800 surface points was approximately 18 s with parallel implementation on the GPU using CUDA. Processing times would be significantly longer if the calculations were conducted in series on the CPU using MATLAB.

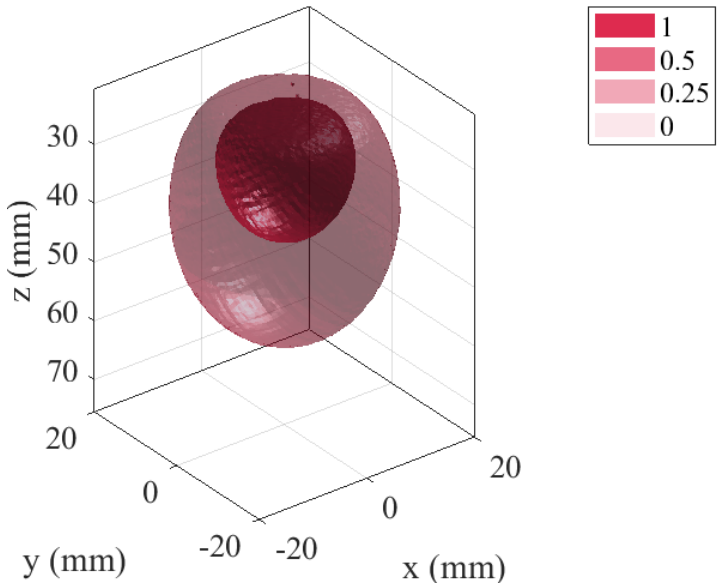

FIGURE 5.3. Normalised 3D sensitivity image using the data from section 2.2 for the sparse array. dB scale normalised between 0 and 1 using maximum amplitude in the image.

The effect of normalising the TFM image by its associated sensitivity image is then investigated. The maximum defect amplitude for each FBH is shown in Fig. 5.6(a) and 5.6(b) in the standard, $I(\mathbf{P})$, and normalised, $I'(\mathbf{P})$, TFM cases respectively; both TFM amplitudes were normalised using the maximum amplitude in FBH 1. The solid

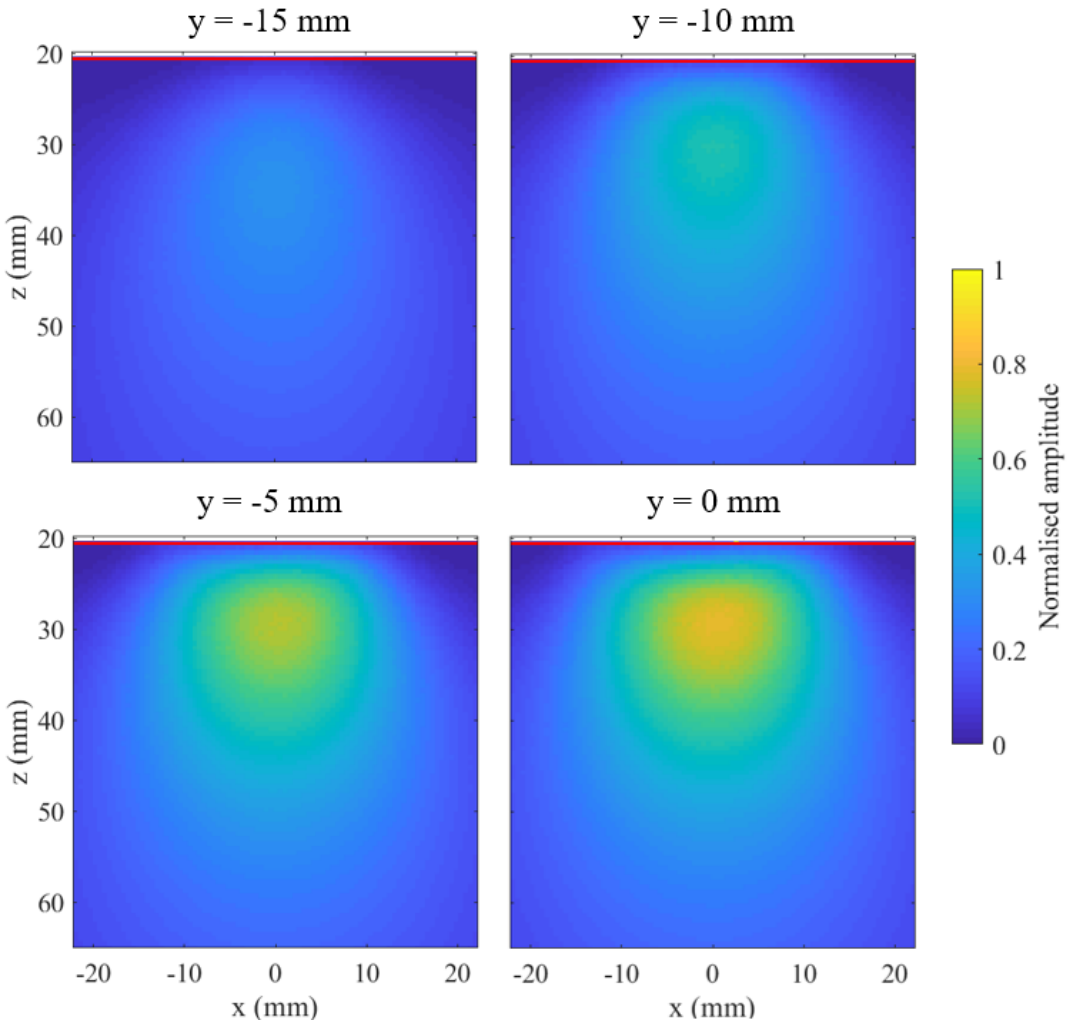

FIGURE 5.4. 2D $(x-z)$ slices of 3D sensitivity image in Fig. 5.3 at increasing steps along y. The red line represents the location of the surface.

lines represent the average maximum defect amplitude, while the dashed lines show $\pm\sigma$ around the mean maximum defect amplitude values. The results show that normalising the TFM image reduces the variability of the defect amplitudes; σ of $I(\mathbf{P})$ and $I'(\mathbf{P})$ are 2.35 dB and 0.92 dB respectively. As defect depth below the array increases, the maximum defect amplitude in the standard TFM decreases. However, in the normalised image all defects are on a comparable amplitude level. This is desirable for defect characterisation, as it logically follows that identical defects should yield identical results in an image, even at increasing distances from the array. When integrating sensitivity images to the process of combining multiple TFM images together, a modified approach is taken to include a weighting term for each individual TFM image.

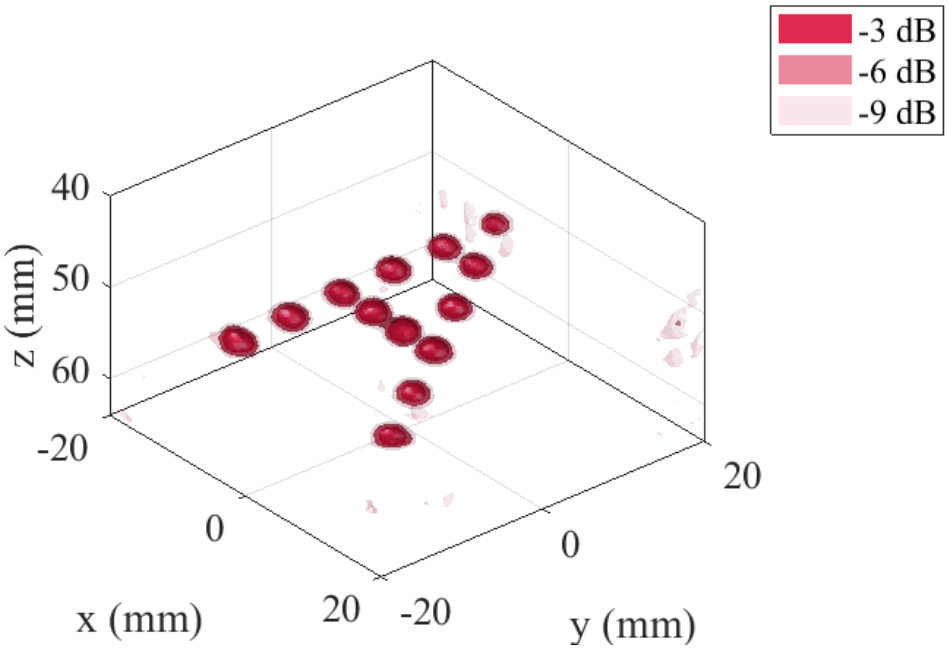

FIGURE 5.5. Weighted immersion 3D TFM image of the A block described in Fig. 2.2. dB scale relative to the maximum amplitude in FBH 1.

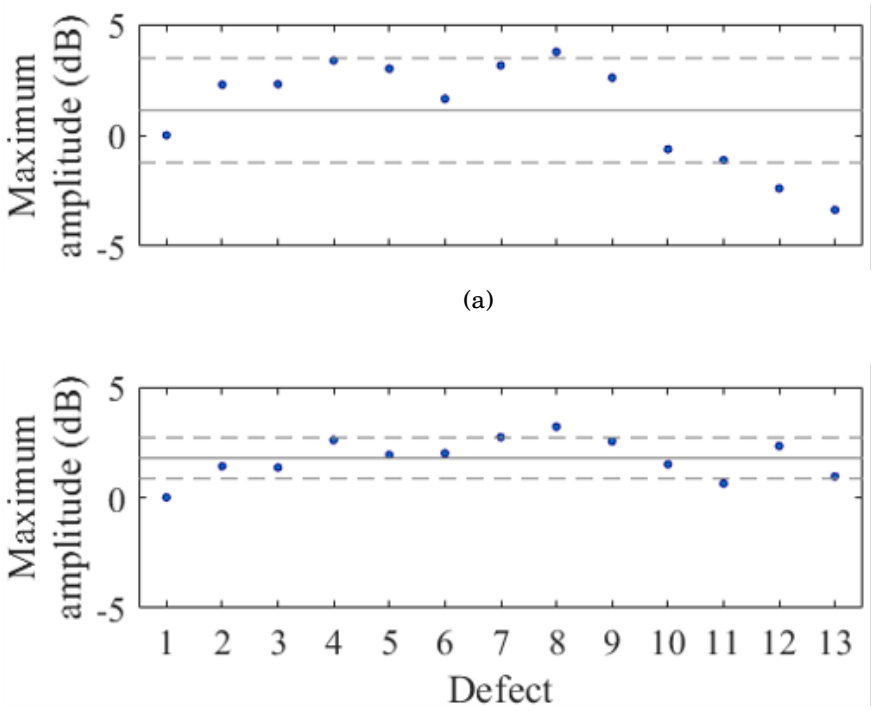

FIGURE 5.6. Comparison of maximum amplitude of defects in the (a) standard, $I(\mathbf{P})$, and (b) normalised, $I'(\mathbf{P})$, 3D TFM images. Solid lines represent average maximum defect values and dashed lines represent $\pm\sigma$ for each case.

5.3 Multi-frame application to doubly curved specimen #1

A flaw of the stitching method described in the previous chapter is the lack of uniform sensitivity throughout the TFM image. In the case of a voxel that is imaged from two array positions, the true amplitude of the voxel in the stitched image is taken to be its maximum value across the two constituent images. If the highest signal present in the overlapping region in either image is due to noise or artefacts then this will appear as the true value in the final image. Furthermore, the response to a given defect in the stitched image is hard to predict as the sensitivity maps of the contributing images are non-uniform. Alternatively, a second stitching method is proposed in this section using sensitivity images, whereby the amplitude at each voxel is the sum of the weighted TFM contributions from each array position.

The final combined TFM image, $I'_{\text{final}}(\mathbf{P})$, can be written as the sum of the weighted individual contributions from each array position by:

$$\begin{aligned} I'_{\text{final}}(\mathbf{P}) &= \sum_k w_k \, I'_k(\mathbf{P}) \\ &= \sum_k w_k \cdot \frac{I_k(\mathbf{P})}{E_k(\mathbf{P})} \end{aligned} \tag{5.11}$$

where k is the scan index, w_k is a weighting factor and the substitution for $I'_k(\mathbf{P})$ is from Eq. (5.10). The values of w_k should be chosen to maximise the overall SNR of $I'_{\text{final}}(\mathbf{P})$, and this is achieved by using a matched filter. A matched filter is chosen as it is the optimal linear filter for maximising the SNR of a signal in the presence of stochastic noise [74]. From [75], if a measured signal has expected signal amplitude s_k and RMS noise μ_k, then the associated weights, w_k, are calculated using:

$$w_k = \frac{s_k}{\mu_k^2}. \tag{5.12}$$

Applying Eq. (5.12) to the case of a measured signal in a standard TFM image, $I_k(\mathbf{P})$, s_k is defined as the sensitivity image $E_k(\mathbf{P})$ and μ_k is the constant uniform noise present across all TFM images, so is represented by μ. For the case of the weighted TFM images obtained by Eq. (5.10), s_k is obtained by dividing the expected signal amplitude in $I_k(\mathbf{P})$ by $E_k(\mathbf{P})$, hence it is given by $E_k(\mathbf{P})/E_k(\mathbf{P}) = 1$. It therefore follows that the RMS

noise in $I'_k(\mathbf{P})$ is $\mu/E_k(\mathbf{P})$. Combining these results with the associated weights in Eq. (5.12), the optimal weighting is defined by:

$$\begin{aligned} w_k &= \frac{1}{\mu^2 / E_k^2(\mathbf{P})} \\ &= \frac{E_k^2(\mathbf{P})}{\mu^2} \end{aligned} \tag{5.13}$$

Combining Eqs. (5.11) and (5.13) therefore yields:

$$\begin{aligned} \sum_k w_k \cdot \frac{I_k(\mathbf{P})}{E_k(\mathbf{P})} &= \sum_k \frac{E_k^2(\mathbf{P})}{\mu^2} \cdot \frac{I_k(\mathbf{P})}{E_k(\mathbf{P})} \\ &= \frac{1}{\mu^2} \sum_k E_k(\mathbf{P})\, I_k(\mathbf{P}) \end{aligned} \tag{5.14}$$

which in theory gives optimal SNR at every point, but the sensitivity to defects will not be spatially uniform. To obtain uniform sensitivity with an ideal reflector at every point, $I_k(\mathbf{P}) = E_k(\mathbf{P})$ and hence each scan should be normalised by $E_k^2(\mathbf{P})$ to give the final expression:

$$I'_{\text{final}}(\mathbf{P}) = \frac{\sum_k I_k(\mathbf{P}) E_k(\mathbf{P})}{\sum_k E_k^2(\mathbf{P})}, \tag{5.15}$$

where the scaling factor $1/\mu^2$ is ignored.

5.3.1 Results

To investigate stitching using sensitivity images, the same data set that was used in the previous chapter is used here. Again, the surface is assumed to be unknown and therefore needs to be extracted. As the method of stitching TFM images that was used in the previous chapter allowed an accurate surface to be extracted, it is used in the surface extraction stage here for speed. Using subsections of the extracted surface as before, the internal 3D TFM image is then generated using Eq. (5.15) and normalised to the maximum amplitude within a patch of the back wall unobstructed by the presence of defects. The interior 3D TFM image is shown in Fig. 5.7 as an isosurface at –24 dB relative to the maximum amplitude in the back wall patch. The defect positions are easily identified, along with large amplitude noise signals around the perimeter of the specimen caused by normalisation using sensitivity images.

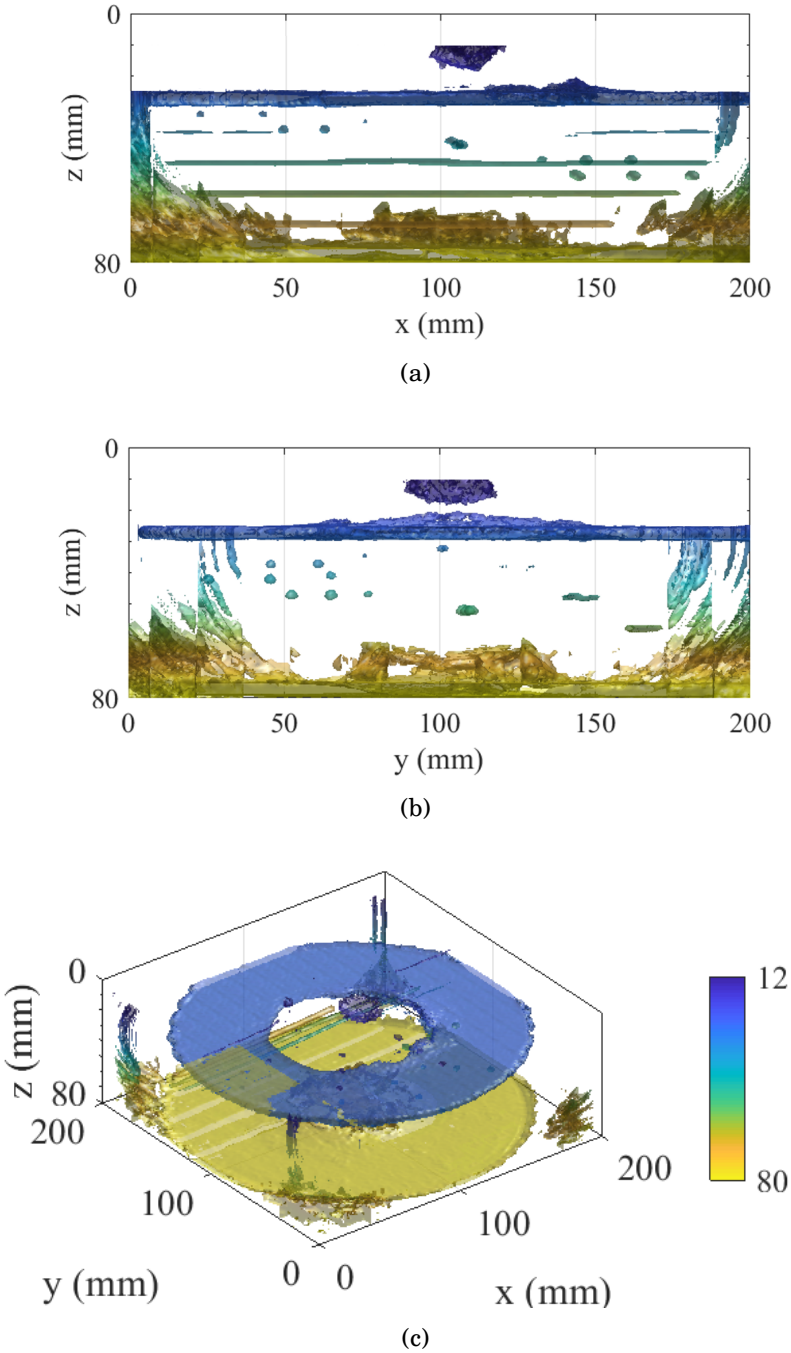

FIGURE 5.7. Stitched 3D interior TFM image of doubly curved specimen #1 obtained using sensitivity images, plotted as an isosurface at –24 dB relative to the maximum amplitude in a region of the back wall. (a) and (b) show elevations, while (c) shows a 3D view.

As was examined in chapter 4, zoomed in windows around BDHs K, L and M are shown in Fig. 5.8, where the defects are circular and well-focused. Snapshots of EDM notches 4, 3 and 2 are also shown in Fig. 5.9; EDM notch 4 has low amplitude as a result of normalisation using the maximum amplitude in the back wall patch, however in all EDM notches the variation of amplitude that was visible in Fig. 4.10 along each notch is not apparent due to the summing of weighted amplitudes at each image point.

One noticeable difference between stitching methods is the ability to view BDH C; this defect was buried in noise in the previous chapter, but is able to be distinguished through weighing, although it has an amplitude approximately 10 dB lower than the second smallest defect signal. BDHs A, B, F, J, N, and R still remain unable to be imaged using the current setup for the reasons described in section 4.4. Of the defects that were able to be imaged, their positions were investigated and compared to the machined locations using their centre points. This was achieved using the same two metrics as in section 4.4: the first is the depth above the back wall and the second is the lateral distance from the surface notch. These distances are then compared to the true values from the specimen design file, with the comparison shown in Fig. 5.10. It was found that σ for the depth comparison was 0.66 mm and 0.92 mm for the lateral distance comparison. Both values are comparable to $\lambda_2/2$ and are also in close agreement with the values obtained using the other stitching method.

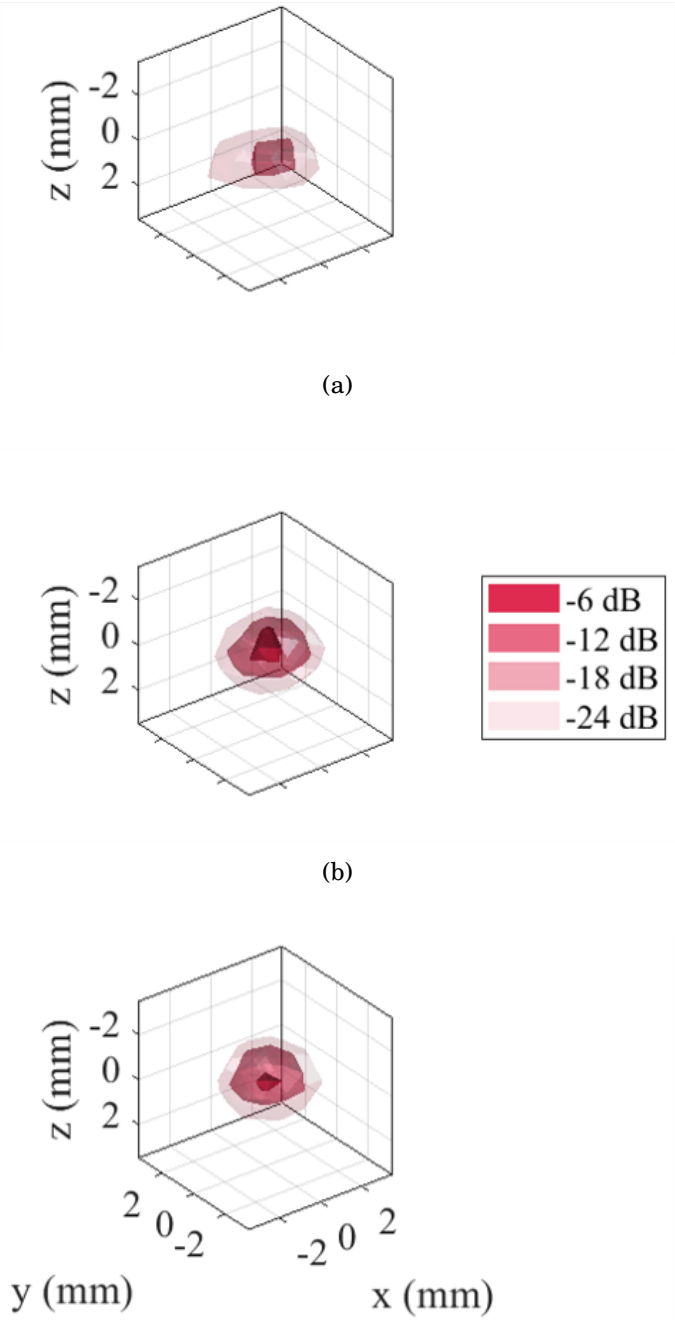

FIGURE 5.8. Zoomed in snapshots of BDHs (a) K, (b) L and (c) M plotted at nominal positions. dB scale relative to the maximum amplitude in a patch of the back wall.

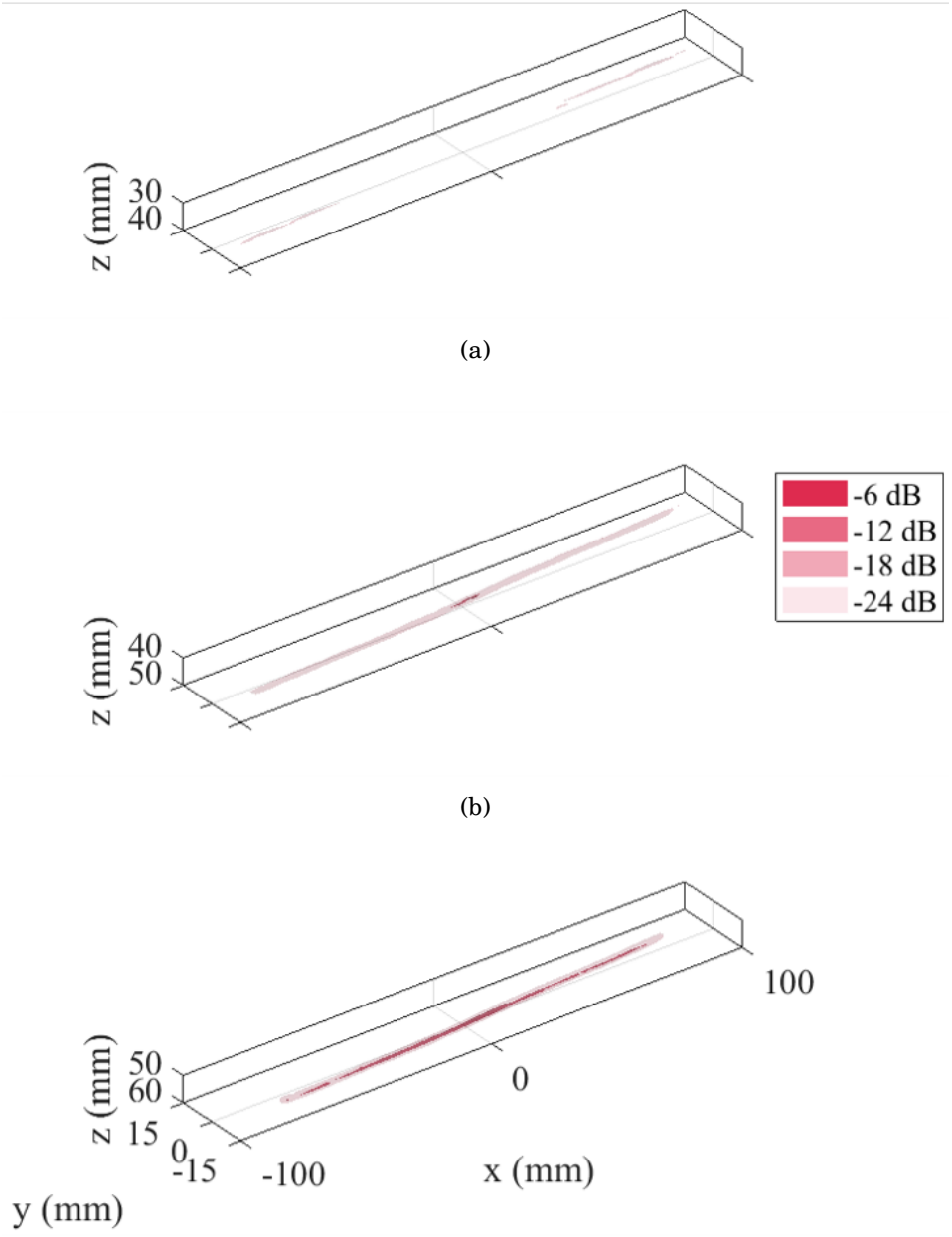

FIGURE 5.9. Zoomed in snapshots of EDM notches (a) 4, (b) 3 and (c) 2 plotted at nominal positions. dB scale relative to the maximum amplitude in a patch of the back wall.

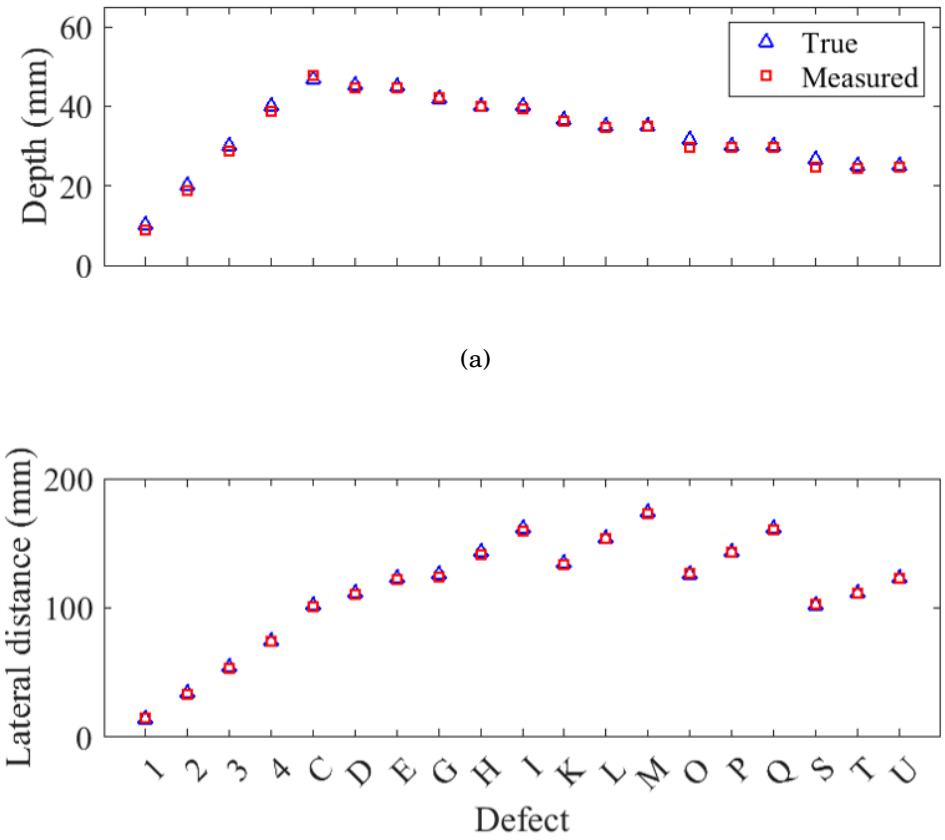

FIGURE 5.10. Comparison of measured and true defect positions using the stitched surface obtained by sensitivity images. (a) Shows the comparison of the depth of the defects above the back wall of the specimen and (b) shows the comparison of lateral defect distance from the surface notch.

A comparison of the maximum defect amplitudes was then investigated using only the BDHs in the specimen for both stitching methods described. Fig. 5.11 shows the maximum defect amplitude for each BDH; Fig. 5.11(a) shows the values obtained in the standard stitched TFM image, $I(\mathbf{P})$, while Fig. 5.11(b) shows the associated values obtained from stitching the individual TFM images using sensitivity images, $I'_{\text{final}}(\mathbf{P})$. The solid lines represent the average maximum defect amplitude, while the dashed lines show $\pm\sigma$ and the amplitude values are relative to the maximum amplitude in BDH L. Although BDH C is able to be imaged in $I'_{\text{final}}(\mathbf{P})$, it is excluded from the results here as its maximum amplitude value is small compared to the others (-21.41 dB). The results show that stitching individual TFM images together by summing the weighted contribution from each TFM image using its associated sensitivity reduces the variablility of defect amplitude, as was observed in the single-frame application. σ of $I(\mathbf{P})$ and $I'_{\text{final}}(\mathbf{P})$ are 4.25 dB and 3.86 dB respectively. In the standard stitched TFM image, as the surface inclination increases above a defect the maximum amplitude is reduced when compared to defects under relatively flatter surfaces. This effect is due to a reduced amount of energy entering the surface and being reflected back to the array from the defect and is evident by the reduced maximum amplitude values of defects G, K, O and S. However, when accounting for the reduced sensitivity of a region within the specimen for a given array position, these defects are imaged to have a comparable maximum amplitude value with the other defects. The exception is defect G, which has a low amplitude value in the images generating using both stitching methods. This is likely due to it lying on the second shallowest radial arm of defects.

With surface and interior resolutions of $\lambda_1/2$ and $\lambda_2/4$ respectively, the time to process all data sets was approximately 36,000 s, or 10 hours. As weighing by the sensitivity requires more time to generate the sensitivity image, it takes approximately twice the time to image a region using the same resolution and number of pixels as when stitching images using maximum voxel values. The code could, however, be optimised to speed up processing times.

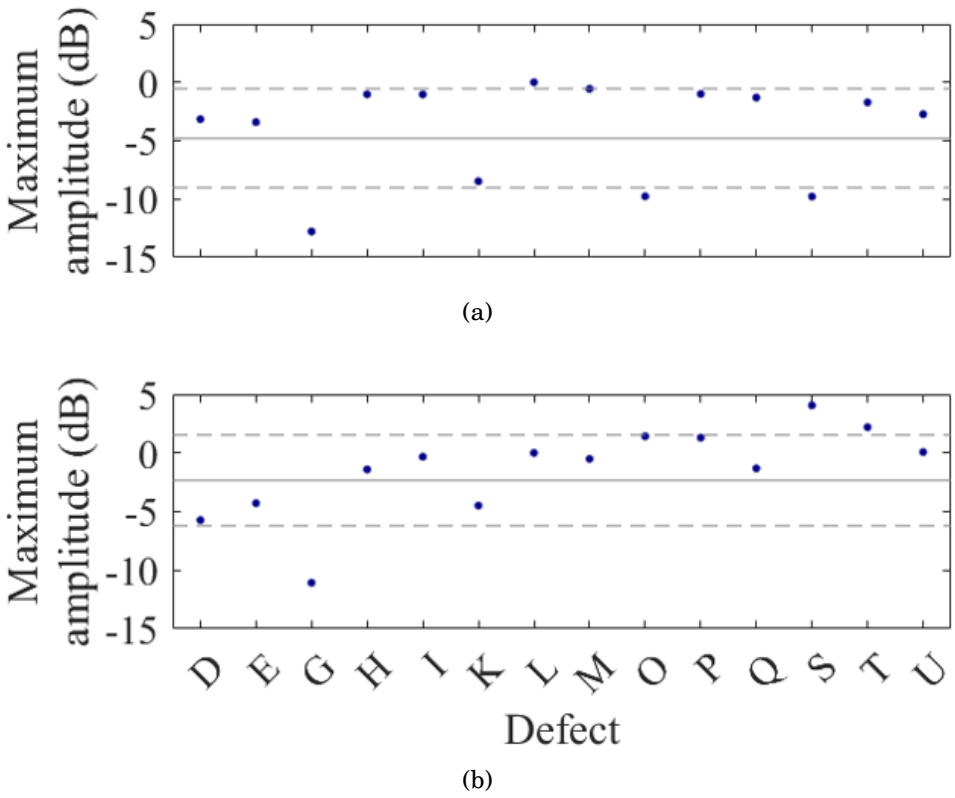

FIGURE 5.11. Comparison of maximum amplitude of BDH defects in the (a) standard stitched TFM image, $I(\mathbf{P})$, and (b) stitched 3D TFM images using sensitivity images, $I'_{\text{final}}(\mathbf{P})$. Solid lines represent average maximum defect values and dashed lines represent $\pm\sigma$ for each case.

5.4 Summary

3D sensitivity images have been introduced in this chapter for optimising TFM imaging using a single frame and multiple data sets captured from a scanned array. The sensitivity image represents an estimate of the TFM intensity that would be measured from a defect at a specific location, and is a useful tool for determining regions in a specimen that can be optimally imaged using a particular inspection setup. Using a single frame application, a TFM image that was normalised by its sensitivity image has resulted in less variability of maximum defect amplitudes of identical defects at increasing depths, as the sensitivity has become uniform in the image. However, normalising a TFM image by its associated sensitivity image produces non-uniform noise in the resulting image. In a standard TFM image, sensitivity is non-uniform and so defects located further away from the array have lower amplitude responses compared to an identical defect located closer to the array. An alternative method for stitching multiple TFM images has also been introduced, whereby the true amplitude of a voxel is the sum of weighted contributions from normalised TFM images at each array position. Defects in the stitched 3D TFM image obtained using sensitivity images were able to be accurately positioned, however defects located under a relatively steep inclined surface region remain impossible to image in the current setup. To assess the stitching methods, the following chapter focuses on the characterisation of defects.

Chapter 6

Defect characterisation

After a defect has been successfully detected, the next step of a thorough inspection involves characterisation whereby defect parameters such as size, shape and orientation can be determined. Knowledge of these parameters allows the defect type to be identified, which is crucial for determining the integrity of a system as planar defects with sharp edges (e.g. cracks and lack of fusion) are more likely to grow and cause failure when compared to volumetric defects (e.g. voids and inclusions). Engineering specifications for a component normally have a requirement that any detected defect must be below an allowable size for continued operation; considering the high-cost structures in which NDT is routinely implemented, accurate characterisation of defects can be the difference between safe operation and failure. Additionally, characterisation on end-of-life components can influence the decision between remanufacturing or scrapping. Remanufacturing is viewed as an advantageous solution when deciding what to do with used components as it is environmentally friendly and cost efficient [76]. The component must, however, meet certain standards before it is reused, which are determined using NDE methods.

3D characterisation of a defect is important for determining its nature. As defects can appear in arbitrary orientations in 3D, it is desirable to insonify the defect from as many directions as possible to obtain the maximum amount of information. Inspection with a linear array means insonifying the defect in a single plane; 3D information about the defect therefore cannot be obtained without translation or rotation of the array. As was mentioned in earlier chapters, a consequence of this means that resolution is limited in the out-of-plane direction, thus making accurate characterisation challenging. As a 2D array can probe a defect over a larger range of solid angles from a single position, its

use is therefore beneficial in the defect characterisation process.

In this chapter, the characterisation of defects is investigated using two specimens. The first is an aluminium specimen with a planar surface containing a variety of machined holes and slots, and the second is a doubly curved specimen with machined holes of different diameters, depths and types. Both specimens are scanned and the resulting 3D TFM images are combined using the two stitching methods described in the previous chapters before characterisation is investigated.

6.1 Defect sizing

In the current work, the size of a hole refers to its diameter as the defect is assumed circular, and the size of a notch or a slot corresponds to its longest length. In industrial applications, however, all dimensions are important for accurate characterisation. The sizing method used is dependent upon the size of the defect relative to the wavelength of sound in the component [77], λ_2. For defects larger than λ_2, direct image-based sizing from the TFM image can be used as an accurate measure of defect size. Image-based sizing is typically achieved using the 6 dB drop method, whereby the size of the defect corresponds to the distance where the amplitude of the defect is greater than 6 dB below the maximum peak amplitude [78]. Fig. 6.1(a) shows an example 2D TFM image of a bottom drilled hole, along with the associated amplitude distribution along x at the z depth corresponding to the location of maximum amplitude. The length of the red arrow in Fig. 6.1(b) corresponds to the estimated diameter of the defect, d. When considering 3D image-based sizing of a volumetric defect, the diameter can be calculated as the maximum Euclidean distance between all voxels greater than 6 dB below peak amplitude [44].

When defects are comparable to λ_2, image-based sizing algorithms become ineffective as the diffraction limit is approached. A proposed method for imaging defects of this size is by using a scattering matrix, or S-matrix [72, 73]. When a defect, or scatterer, scatters energy from an incoming wave, the scattered field contains information unique to that defect such as size, orientation and location. Measurement of the scattered field in the far-field of the defect as a function of incident angle, scattered angle and frequency yields the S-matrix. Therefore, defect classification using S-matrices is most successful if a certain angular region around the specular direction of the defect can be

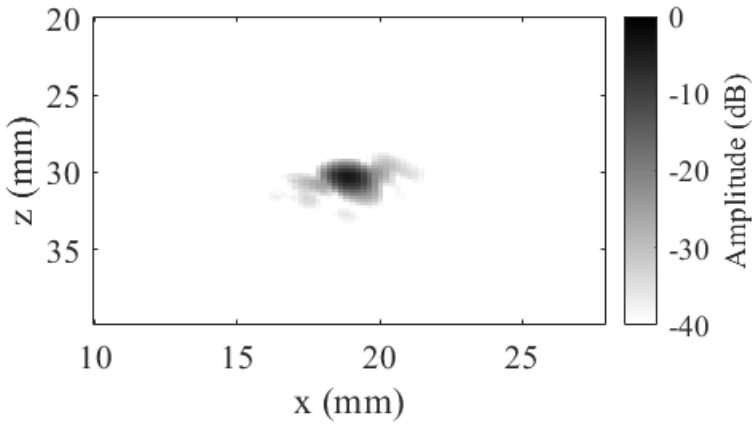

(a)

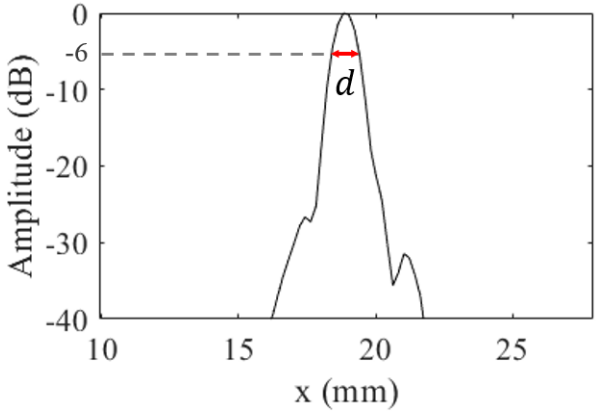

(b)

FIGURE 6.1. Illustration of the 6 dB drop method for defect sizing in 2D. (a) shows the TFM image of a bottom drilled hole and (b) is the associated amplitude distribution along the line passing through the maximum defect amplitude. d is the measured diameter of the hole.

insonified. Once the S-matrix of a defect is known, the maximum amplitude can be used to determine the defect size, or it can be compared to a database of S-matrices of known defects [79]. Previous studies in 2D have shown S-matrices are promising for improved characterisation of small crack-like defects [80], but have yet to be fully implemented in 3D due to their complexity and computationally expensive calculations [11]. It is for this reason that 3D S-matrices are not considered as a sizing method in the current work. However, if there is prior information about the types or orientations of potential defects, the relevant S-matrices can be included in the sensitivity model described in section 5.1.

When defects are very small, or less than half of λ_2, the performance of S-matrix characterisation breaks down and amplitude-based sizing is the only sizing method available [81]. This is where the peak defect amplitude is used to deduce the size; this method requires a reference defect of known size and amplitude and a modeled relationship between the two is needed. It also implicitly requires an assumption to be made on the type and orientation of defect that is potentially present. This method only works when the peak defect amplitude is greater than the noise level in the image.

As the defects in both specimens to be considered here are comparable to or greater than λ_2, only direct image-based sizing from a 3D TFM image using the 6 dB drop method is used in the current work.

6.2 Defect orientation

The orientation of a defect refers to its angle of inclination. A circular crack or tip of a FBH has an orientation defined by its normal vector, which requires two independent quantities to describe it: azimuth and elevation angles. In general, a 3D defect of a certain shape with no rotational symmetry, such as an elliptical crack, needs three independent angles to completely describe its orientation: azimuth, elevation and rotation around the normal. Only spherical defects, e.g. voids or inclusions, are symmetric and are therefore not associated with an inclination value.

Defect orientation is investigated in the current work using a range of angled slots. In 2D, the orientation of an angled slot can be described by a single angle from a reference axis, as illustrated in Fig. 6.2(a). Specular reflection from the slot falls outside the angular measurement range of the array, which results in only the crack tip signals being observed. Fig. 6.2(b) shows the amplitude distribution along the angled dashed line passing through the points of maximum amplitude in each crack tip. In [77], the length and angle of a 2D crack-like defect was determined by fitting a rectangle to enclose all points in a defect that are greater than 6 dB below the maximum amplitude value. The longest dimension of the rectangle corresponds to the length, while the angle is calculated using trigonometry. A slightly different approach is taken in the current work, where the length of the slot, l, is taken as the distance between 6 dB drop measurements in the crack tips, and the inclination angle, θ, is measured using the line which passes through the crack tips.

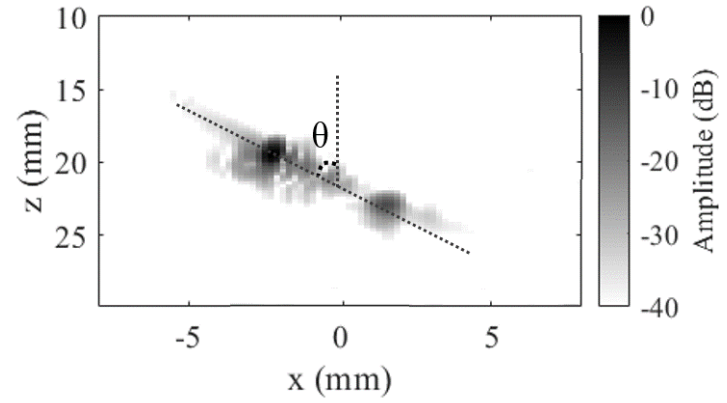

(a)

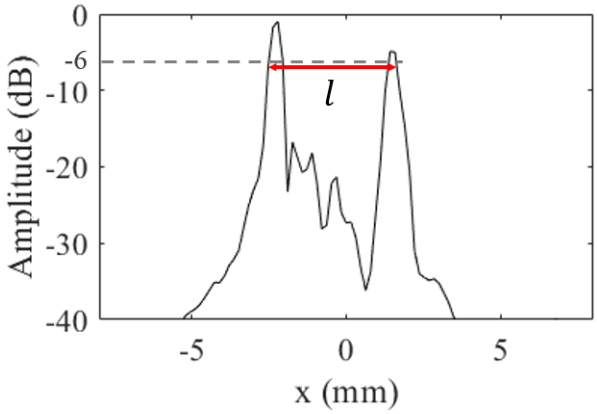

(b)

FIGURE 6.2. Illustration of the 6 dB drop method for slot sizing and orientation in 2D. (a) shows the TFM image of a 45° angled slot and (b) is the associated amplitude distribution along the angled dashed line passing through the maximum amplitudes in each crack tip. l is the length and θ is the inclination angle.

When characterising an arbitrarily oriented crack in 3D, three angles have to be considered: azimuth, elevation and rotation around the normal direction. However, in the current work only through-slots are considered, i.e. there is no variation in the slot along y, which simplifies the sizing process as only a single inclination angle is needed for characterisation. Starting with the stitched 3D TFM image, all amplitude values corresponding to voxels along the y direction are summed for each (x,z) location. This collapses the 3D image to a 2D TFM image, so the length and angle of the slot can be determined as shown in Fig. 6.2.

6.3 Processing method

Defect characterisation is investigated using stitched 3D TFM images. Method 1 stitches scanned data sets using the procedure outlined in chapter 4, where the amplitude value of a voxel that is imaged from more than one array position is taken as the maximum voxel amplitude across all frames. Method 2 stitches the data sets using sensitivity images, as described in chapter 5. Fig. 6.3 shows a flow diagram of the key steps in both methods, where the surface TFM images were stitched using method 1 and excluded from the flowchart. Method 1 was used to stitch the surface TFM images as it was demonstrated to allow accurate surface extraction at a faster speed than using method 2. The surface profile was assumed to be unknown and was extracted using the method outlined in section 3.4. Only data sets with subsections of surface points greater than 1,000 were considered but this stage has also been excluded from the flowchart for ease of reading. The ability to characterise each defect type is then investigated.

Two test specimens with a range of defects and different surface profiles are imaged, and their descriptions are given in the following sections along with the results. In both cases, the specimen was placed in an immersion tank and the sparse 2D array was scanned across its surface using 50% array overlap, collecting a HMC data set at each position.

6.4 Case #1 – Planar surface

The first case to be examined is the sizing and orientation of defects through a planar surface. The array was scanned in 15 mm increments along the x axis to yield a total of 11 data sets.

6.4.1 Specimen description

An illustration of the specimen is shown in Fig. 6.4, and Table 6.1 contains parameters of the machined defects. The specimen is a $(50 \times 200 \times 50)$ mm block of aluminium containing 3 FBHs of increasing diameter, 4 further FBHs of constant diameter at different depths, 4 horizontal slots of increasing length and 4 angled slots of increasing length at 45°. The slots in this specimen extend the entire way through the specimen, i.e. they are constant along y. Before the scan, v_1 and v_2 were measured to be 1480 m/s and 6360 m/s respectively.

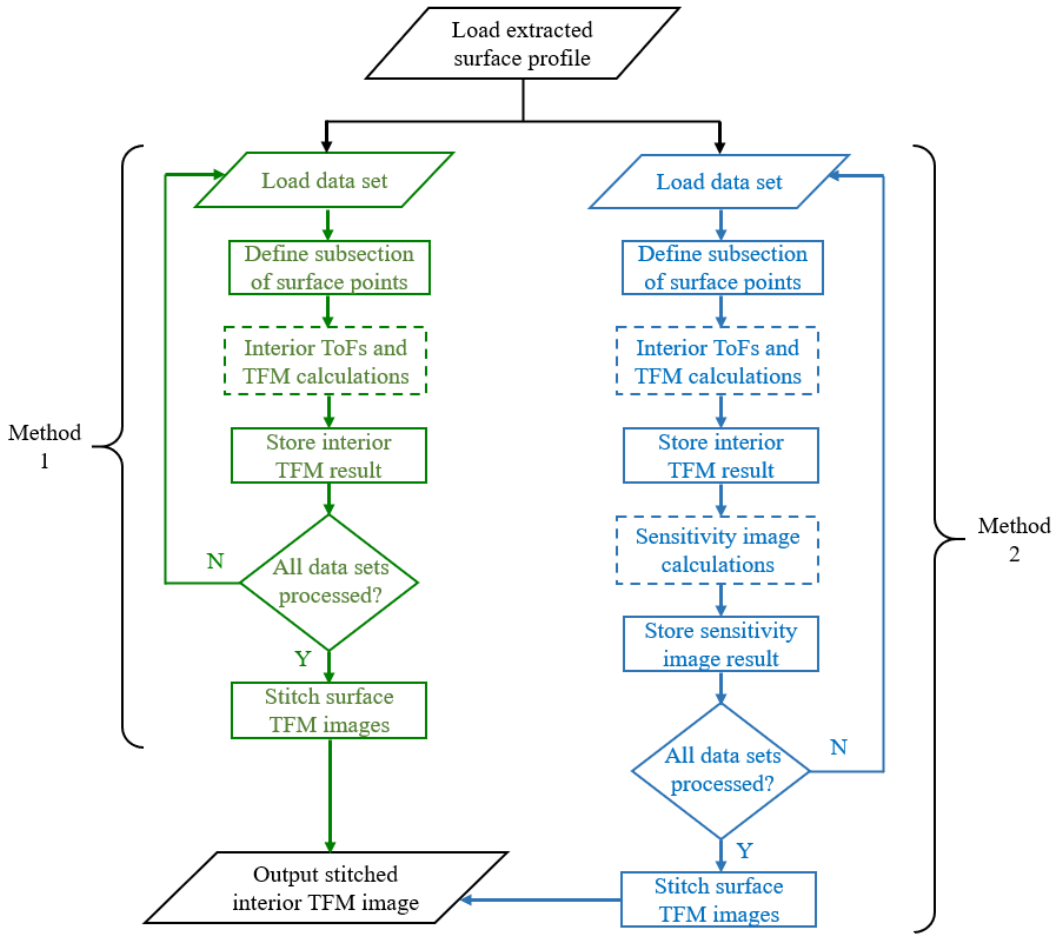

FIGURE 6.3. Flow diagram showing the key steps of the two stitching methods used for combining multiple interior TFM images into a single, larger TFM image. Method 1 is in green, while method 2 is in blue. Solid symbols are processes calculated on the CPU using MATLAB, while dashed symbols are processes calculated in parallel on the GPU using CUDA.

6.4.2 Results and discussion

The stitched 3D TFM image of the interior of the specimen using method 1 is given in Fig. 6.5, while the result using method 2 is shown in Fig. 6.6. Both figures are plotted at dB scales relative to their respective maximum amplitudes in FBH 7, highlighted by the blue box in the figures. The back wall is located at 71.4 mm below the array and is excluded for visual purposes. The indications in both images at $z = 50$ mm and $z = 60$ mm in the range $(80 < x < 120)$ mm are caused by second reflections from the horizontal slots, while the indication at $(x = 150, z = 50)$ mm is a second reflection from the longest angled slot. The FBHs were sized using the 6 dB drop method outlined in section 6.1 and

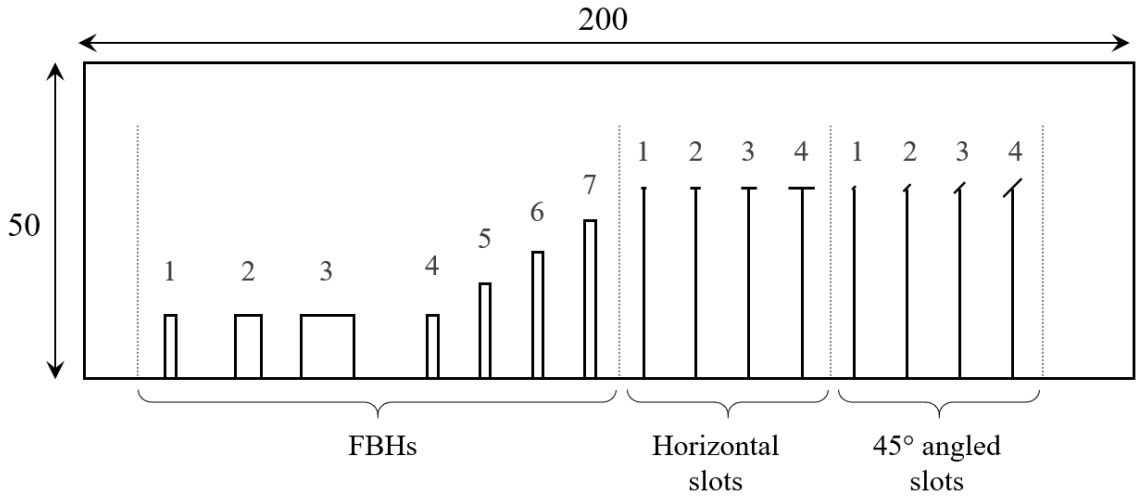

FIGURE 6.4. Diagram of test piece used in case #1 for defect characterisation.

the lengths and angles of the slots were found by reducing the 3D TFM images to 2D as was described in section 6.2. By visual comparison of the $(x-z)$ elevations of the stitched TFM images, all defects appear well-focused and easy to locate. It is easy to discern that the horizontal slots, located at $(80 < x < 120)$ mm, increase in length as x increases, and the crack tips of the 45° angled slots, located at $(120 < x < 160)$ mm, become more pronounced as the length of the defect increases. Table 6.2 shows the measured defect parameters using method 1 and method 2.

TABLE 6.1. Characterisation parameters of defects in specimen used for case #1. d is the hole diameter and l is slot length.

	d (mm)	d (λ_2)	Distance above back wall (mm)
FBH			
1	2	0.95	10
2	5	2.4	10
3	10	4.8	10
4	2	0.95	10
5	2	0.95	15
6	2	0.95	20
7	2	0.95	25
	l (mm)	l (λ_2)	Distance above back wall (mm)
Horizontal slot			
1	1	0.48	30
2	2	0.95	30
3	3	1.4	30
4	5	2.4	30
	l (mm)	l (λ_2)	Distance above back wall (mm)
45° angled slot			
1	1	0.48	30
2	2	0.95	30
3	3	1.4	30
4	5	2.4	30

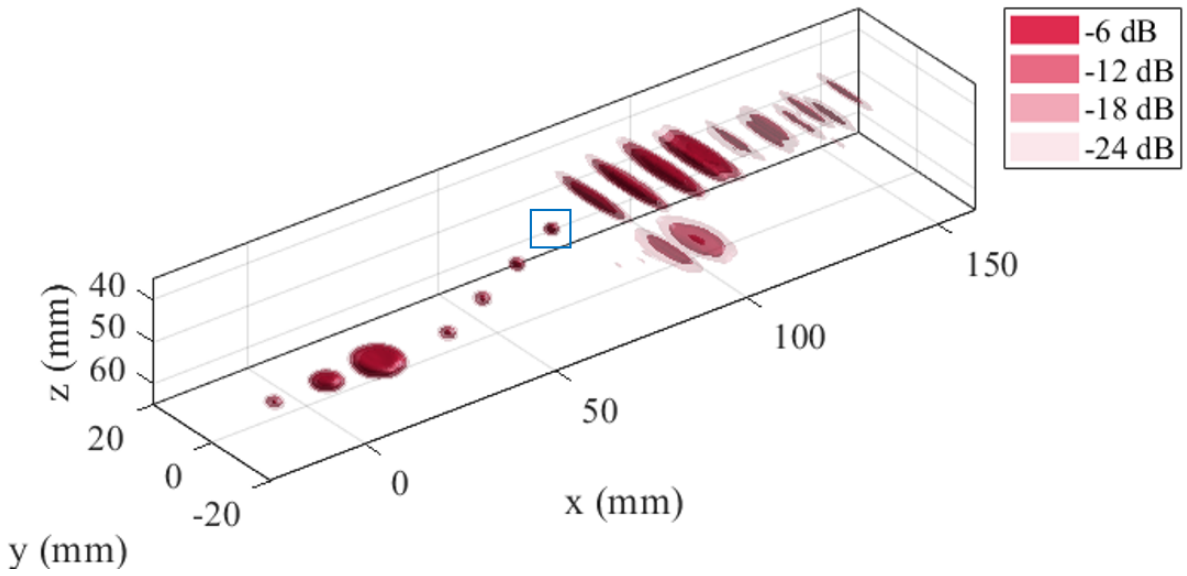

(a)

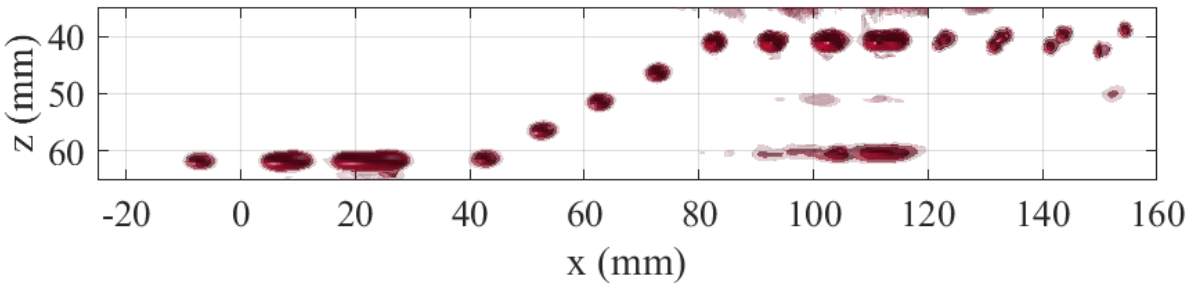

(b)

FIGURE 6.5. Stitched 3D interior TFM images through a planar surface using method 1. (a) shows a 3D view, while (b) shows the $(x-z)$ elevation. dB scale is relative to the maximum amplitude of FBH 7 (highlighted by blue box).

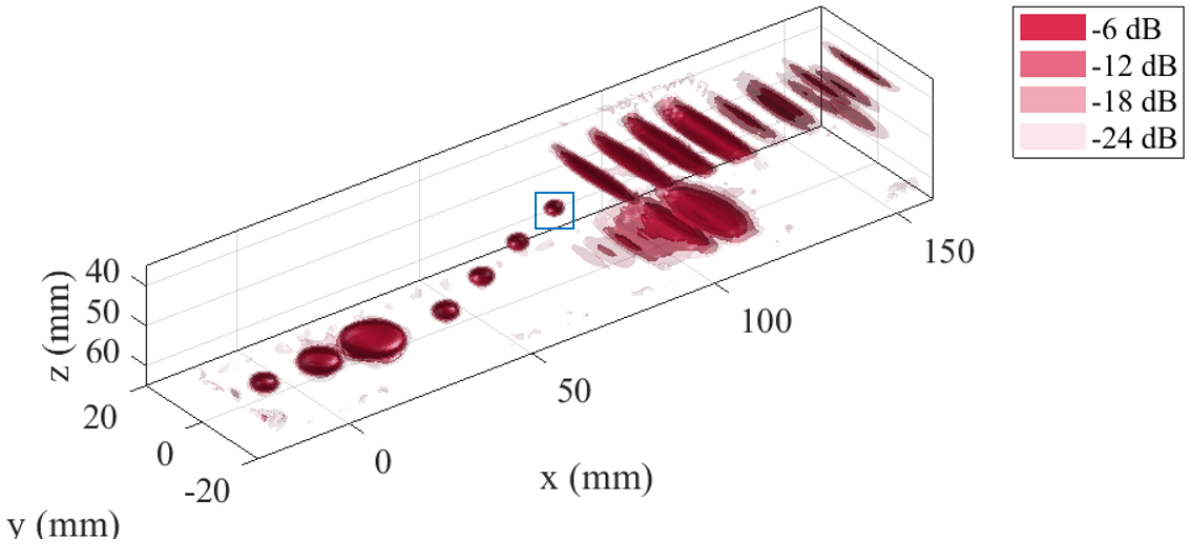

(a)

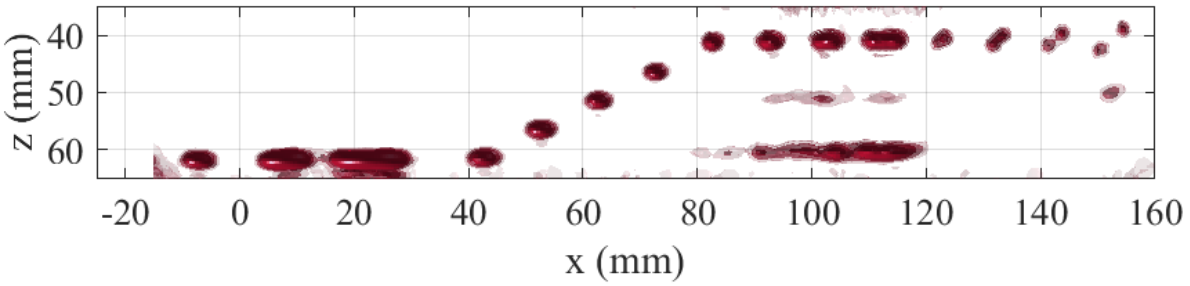

(b)

FIGURE 6.6. Stitched 3D interior TFM images through a planar surface using method 2. (a) shows a 3D view, while (b) shows the $(x-z)$ elevation. dB scale is relative to the maximum amplitude of FBH 7 (highlighted by blue box).

TABLE 6.2. Measured defect parameters for case #1 using both stitching methods.

	Method 1	**Method 2**	**True value**
		d (mm)	
FBH			
1	3.39	3.35	2
2	5.32	5.60	5
3	10.54	10.36	10
4	3.20	3.32	2
5	3.39	3.08	2
6	2.68	2.83	2
7	2.41	2.66	2
		l (mm)	
Horizontal slot			
1	2.59	2.35	1
2	2.61	2.83	2
3	3.35	3.64	3
4	5.98	5.94	5
		l (mm) / θ°	
45° angled slot			
1	1.87 / 45.4	1.91 / 45.4	1 / 45
2	3.02 / 45.4	2.96 / 45.4	2 / 45
3	4.03 / 39.1	3.88 / 39.1	3 / 45
4	5.76 / 38.3	5.69 / 38.3	5 / 45

The results in Table 6.2 show that overall, both stitching methods produce similar values for the measured defect parameters. As expected, defects with sizes close to λ_2 were overestimated as image-based sizing is less accurate. However, as the FBH diameter increases for FBH 2 and 3, the measured diameter agrees with the true values within an error of $\lambda_2/3$. FBHs 4–7 were unable to be accurately sized due to their diameters being less than λ_2. The same pattern is visible for the measured length of the horizontal slots: 1 and 2 are unable to be accurately sized but 3 and 4 agree with the true values within an error of λ_2. The measured lengths of the angled slots 3 and 4 also agree with the true values within λ_2. The measured angles were the same in both methods, where the smaller slots were measured to be 45°. As l increased, the θ reduced to within a $\pm$ 7° range.

The overestimation of all values is likely due to the resolution of the imaging

grids; the stitched TFM images have a grid spacing of $\lambda_2/4 \approx 0.53$ mm in all directions, which therefore results in a coarse grid when imaging defects of comparable size. Fig. 6.7 illustrates this using angled slot 4, where the red boxes represent the image points of maximum amplitude in each crack tip and the amplitude distribution along the blue line is considered during characterisation. Using a finer grid of image points would improve resolution, but significantly slow down processing time. However, during an inspection the scan could be used initially to determine defect locations, and then more detailed inspection can occur afterwards in any regions of interest. Overall, both stitching methods produced similar results which enabled defects larger than the wavelength to be sized within an error of λ_2 and angled notches were able to be determined within 7°.

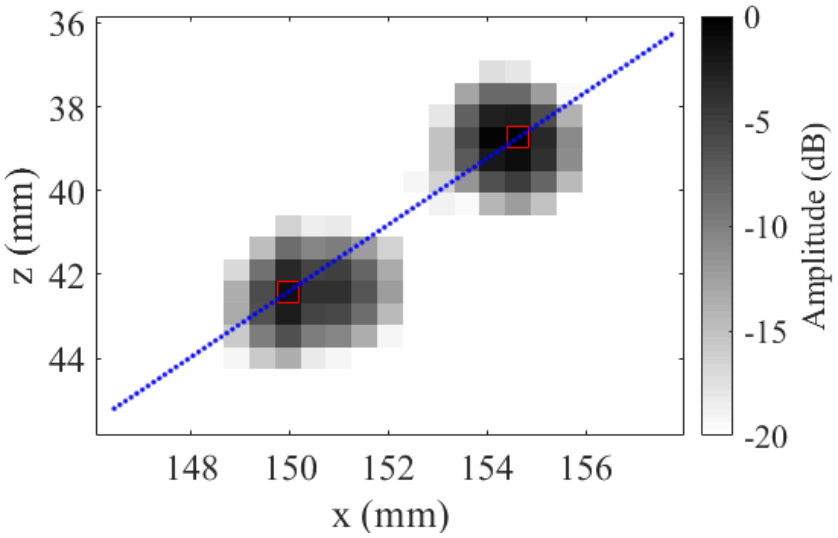

FIGURE 6.7. 2D TFM image of angled slot 4 plotted relative to maximum amplitude in the defect, imaged using method 1 and a grid resolution of $\lambda_2/4$. The locations of maximum amplitudes in each crack tip are highlighted by red boxes and the amplitude distribution along the blue line is used for slot characterisation.

6.5 Case #2 – Doubly curved specimen #2

In this section round bottom holes (RBHs) and FBHs are sized through a doubly curved surface. The array was scanned using a similar setup as was shown in Fig. 3.12, whereby the array footprint was mounted parallel to the back wall of the specimen and scanned in increments of 15 mm in the x and y directions, to yield a total of 225 array positions.

TABLE 6.3. Type and diameter of defects in doubly curved specimen #2.

Defect		
FBH	RBH	d (mm)
A	-	6
B1	B2	8
C1	C2	8
D1	D2	8
E1	E2	8
F1	F2	4
G1	G2	4
H1	H2	4
I1	I2	4
J1	J2	6
K1	K2	6
L1	L2	6
M1	M2	6
N1	N2	2
O1	O2	2
P1	P2	2
Q1	Q2	2

Array positions that were not directly over the specimen were discounted. Before the scan, v_1 and v_2 were measured to be 1480 m/s and 6470 m/s respectively.

6.5.1 Specimen description

The specimen used to investigate defect sizing through a doubly curved surface has an identical surface profile to doubly curved specimen #1 from section 3.5.1, i.e. it is described by Eq. (3.6), but the height of the base was reduced to allow defects to be machined. The specimen contains FBHs and RBHs of different diameters located 20 mm below the surface; FBHs were chosen because the flat tip appears like a circular crack when ultrasonically imaged from above, while the tip of RBHs resemble a spherical void. An illustration of the specimen design is shown in Fig. 6.8, with the defects labelled in the base view in Fig. 6.8(b). The diameters, d, and types of machined defects are given in Table 6.3.

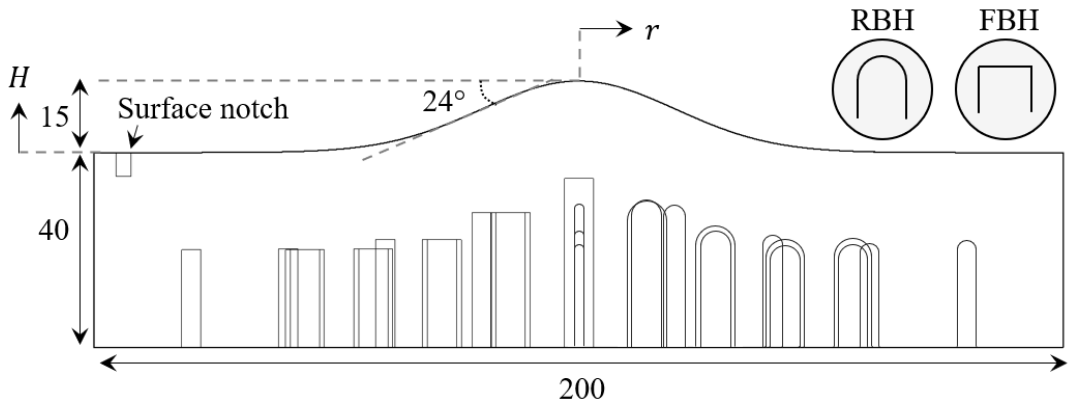

(a)

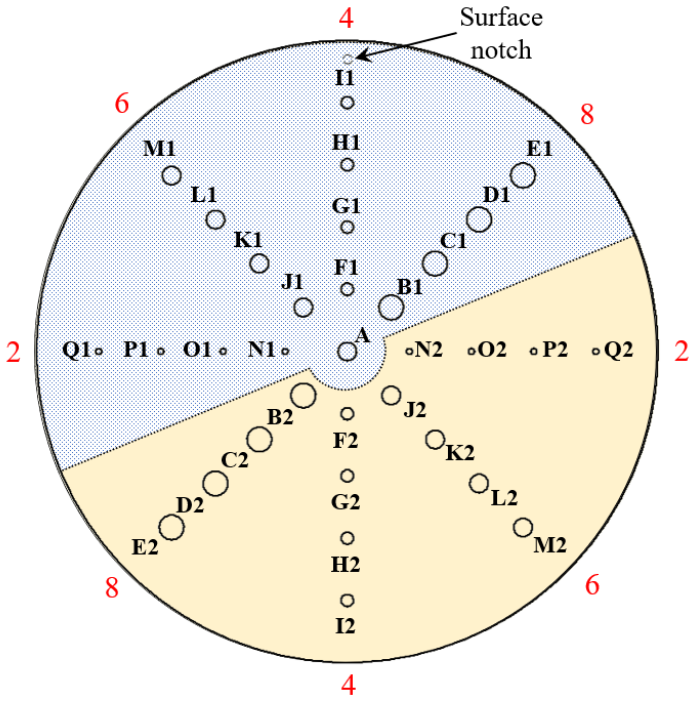

(b)

FIGURE 6.8. Illustration of doubly curved specimen #2. (a) shows the side profile and (b) shows the base view with the defects and hole diameters labelled in red. The defects in the dotted blue region of (b) correspond to FBHs, while the defects in the solid yellow region are RBHs. Units in mm.

6.5.2 Results and discussion

Figs. 6.9(a) and 6.9(b) show the 3D TFM images of the defects in doubly curved specimen #2, plotted using isosurfaces at multiple amplitude levels relative to the maximum amplitude in defect I1, using method 1 and method 2 respectively. The front and back walls have been excluded for visual purposes. In both figures the defects on the innermost, or first, ring (i.e. defects B, F, J and N) are not visible using the chosen dB scale, but the majority of the remaining defects are able to be visually identified. Fig. 6.9 illustrates that method 2 has reduced the variation in amplitude between defect responses, as evidenced by the higher indication amplitudes of defects in the second ring (i.e. defects C, G, K and O). This is expected due to the summing of weighted TFM images in method 2 to create uniform sensitivity throughout the individual images.

A significant difference between imaging methods is the ability to detect defects located on the first ring. When using method 1, the SNR of the defects are too low to determine their locations, however, the SNR increases when using method 2. Sizing was investigated by using the method outlined in section 6.1. Fig. 6.10 shows the measured diameters of the defects in comparison to their true values: Fig. 6.10(a) illustrates the results using method 1, while Fig. 6.10(b) shows the values obtained using method 2. Defects on the first ring have been excluded from the results in Fig. 6.10(a). Overall, both methods obtain similar estimations of defect diameters. For each stitching method, RBHs and FBHs of equal diameter (excluding those on the first ring) can be compared. The results show that the measured FBH diameters are larger than those obtained for the RBHs, the latter of which are consistently undersized. This is likely caused by the geometry of the defects. Each point on the surface of a RBH has a unique normal associated with it, as it is a doubly curved surface. Therefore, if the incoming rays are not travelling at near-normal incidence, the ray will be scattered and fall outside the measurement range of the array. Hence all that can be imaged is a small patch of the surface where the surface normals point back to the array and the defect is undersized. For this reason it is basically impossible to directly size spherical voids from an image. On the other hand, a FBH has a constant normal across the planar surface, so specular reflection is more likely to occur. Illustrations of the tip geometry of a RBH and FBH are shown in Fig. 6.11, where the regions highlighted in red can potentially result in the specular reflection of a ray when an array scanned above the defect in the $(x-y)$ plane.

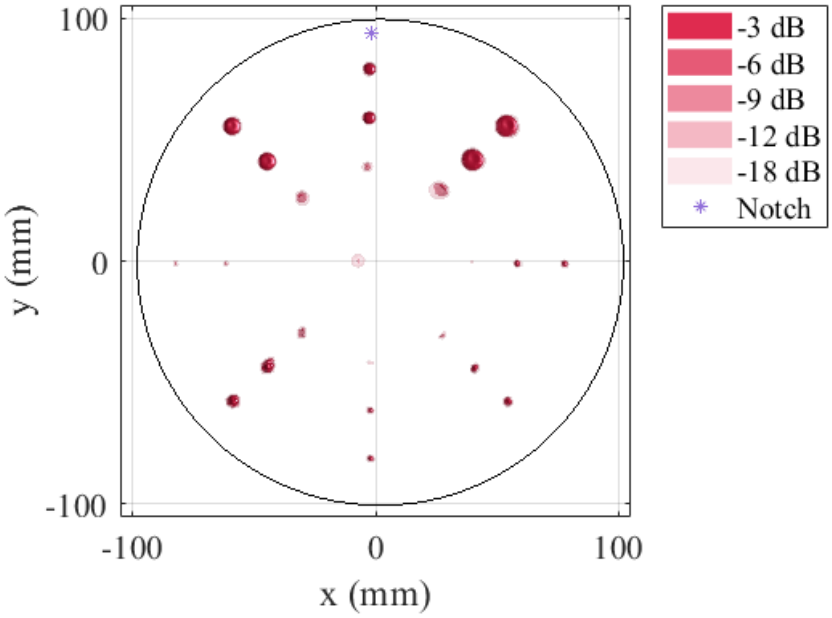

(a)

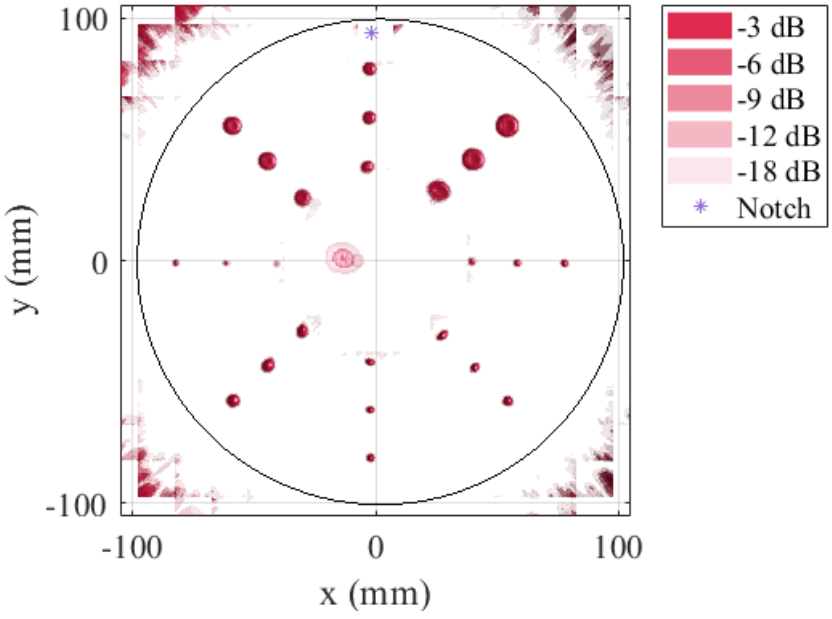

(b)

FIGURE 6.9. Stitched 3D TFM images of the defects in doubly curved specimen #2 using (a) method 1 and (b) method 2. The dB scales are relative to the maximum amplitude of FBH I1 and the outline of the specimen is in black.

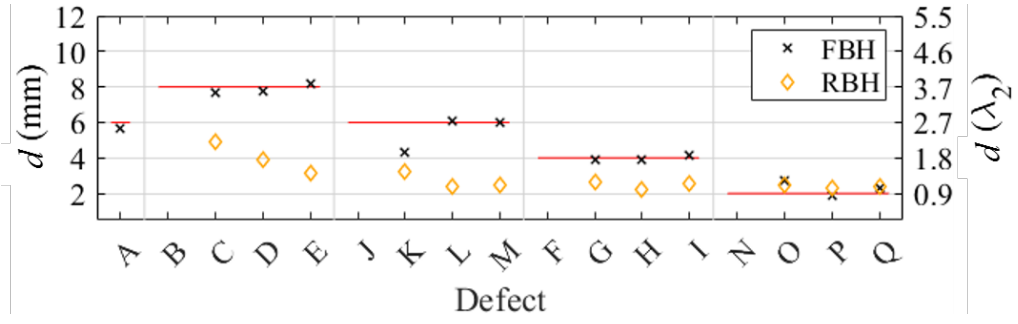

(a)

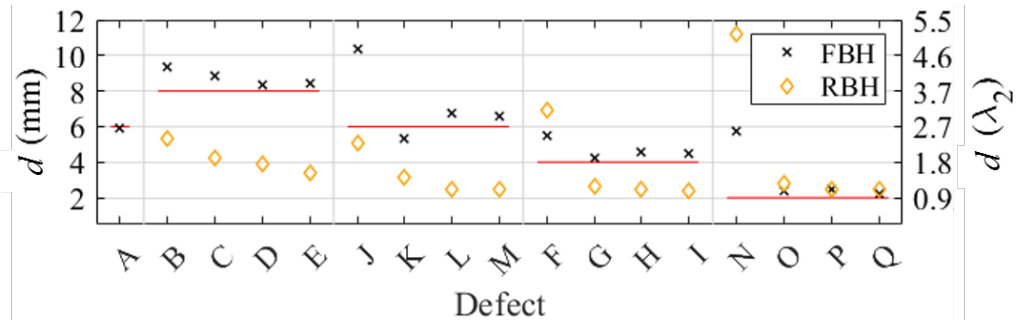

(b)

FIGURE 6.10. Comparison of measured defect diameters in doubly curved specimen #2 compared to true values. Results in (a) were obtained using stitching method 1, while (b) used stitching method 2. The red horizontal lines represent the true defect diameter.

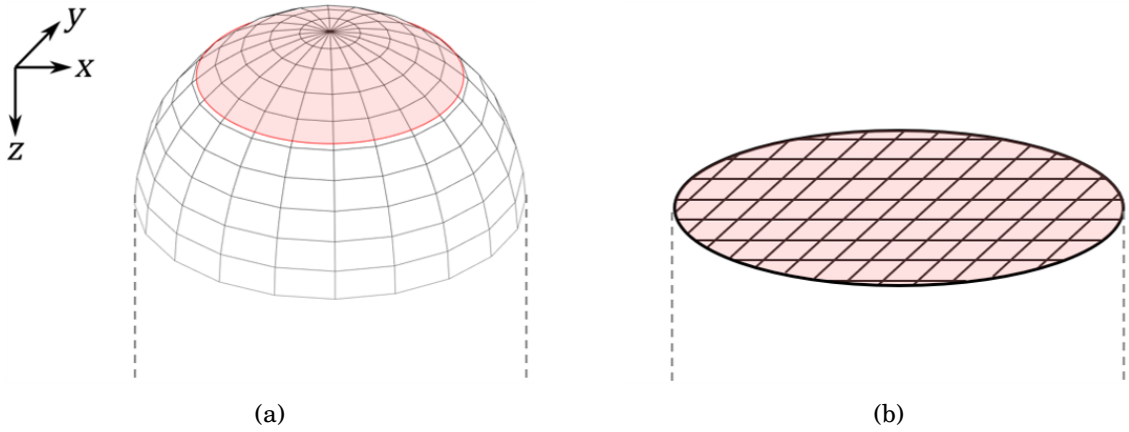

FIGURE 6.11. Geometry of the tip of a (a) RBH and (b) FBH. Regions highlighted in red represent parts of the defect that can specularly reflect an incoming ray when an array is scanned across the $(x-y)$ plane above the defect.

When considering defects within the first ring using method 2, the average defect amplitude is –27 dB. Therefore, when determining the number of voxels in the 6 dB drop method, the defect amplitudes are so low that noise or other artefacts can be included in the calculation. This is the reason why some diameter values are excessively large, such as defect N. For all FBH sizes, the defects that are located under the flatter regions of the surface are imaged better; this is no surprise due to previous analysis of the array and surface locations in the current setup.

Table 6.4 shows a summary of the mean and σ of the errors for the measured diameters when compared to their true sizes as presented in Fig. 6.10. When the first ring of defects are excluded, both imaging methods have similar error values. The FBHs are measured better, as the σ associated with these measurements is comparable to $0.25\lambda_2$, while the RBHs have a σ value of $\approx 0.9\lambda_2$. When the first ring of defects *are* included using method 2, σ for the FBHs more than triples and σ for the RBH almost doubles, which suggests that measurements of defects under the steeply inclined regions are challenging to size using the current setup, even though they can be detected. For all FBHs excluding the first ring, the mean error is within $0.17\lambda_2$, whereas the mean error is larger by a factor of 6 when considering the RBHs.

The total processing time to generate method 2 was 34,000 s, or approximately 9.4 hours, while processing time can be reduced to approximately 6 hours when using method 1 at the same grid resolution. Using this setup, there is a trade-off between time

TABLE 6.4. Summary of mean and standard deviation errors of measured FBHs and RBHs in doubly curved specimen #2 using both stitching methods. The individual defect errors can be seen in Fig. 6.10. Defects in the first ring (B, F, J and N) were unable to be imaged using method 1.

		Mean / σ errors of d (mm)	
		Method 1	Method 2
Including 1st ring of defects	FBH	-	-0.91 / 1.29
	RBH	-	1.04 / 3.42
Excluding 1st ring of defects	FBH	0.11 / 0.55	-0.35 / 0.39
	RBH	2.12 / 1.82	2.10 / 1.91

and the ability to detect defects under the steeply inclined surface region. In the current work, the imaging region for each array position was defined in x and y to be 1.5 times the diameter of the array, which was approximated as 30 mm. This means that only $\pm$22.5 mm in the x and y directions were imaged from the centre of the array; ideally, a larger region should be examined as the array is not necessarily most sensitive to the region directly underneath it when imaging a complex surface. An opportunity to further this work would therefore be to deduce the imaging region directly from the sensitivity image. This process would require intense calculations and a method of extracting a 3D S-matrix to improve the sensitivity model.

6.6 Summary

3D defect characterisation has been investigated in this chapter using a scanned array and two specimens with a range of defects. The data sets collected from the specimens were processed using the stitching methods described in chapters 4 and 5. The first specimen had a planar surface and contained a variety of FBHs and slots; the results showed that defects that are greater than the wavelength of sound were able to be accurately sized, and the inclination of the angled slots was able to be determined within 7°. Due to the diffraction limit for image-based sizing, defects smaller than the wavelength were unable to be accurately sized. Both stitching methods produced similar results in this case. Defect sizing through a doubly curved surface was then investigated; the specimen has a similar surface profile to the specimen that was investigated in chapter 4 and contained FBHs and RBHs of different diameters at constant depth beneath the surface. It was found that by stitching the images using sensitivity images,

defects that were unable to be imaged using the other method were now able to be detected. However, the amplitude signals of these defects were too low to allow accurate sizing. As was observed in the first specimen, both stitching methods produced similar results and the standard deviation of defect sizing was less than a quarter of the wavelength. Stitching images using sensitivity maps took on average 4 hours longer to process than the method of taking the maximum defect amplitude across multiple image frames, so there is a trade-off between processing time and the ability to detect defects.

Chapter 7

Conclusions

7.1 Review of thesis

This thesis has investigated 3D volumetric TFM imaging using a sparse 2D phased array and the subsequent ability to detect and characterise defects through complex surfaces.

First, in chapter 2, the imaging abilities of linear, matrix and sparse arrays were compared through a planar surface in contact and immersion setups using HMC and TFM. It was shown that the sparse array outperformed the other arrays as it produced well focused defects, made possible by the spread of elements across a 2D aperture allowing focusing throughout a 3D volume. Although a matrix array also has the ability to focus throughout a volume, the geometry of the element layout resulted in reduced focusing power.

The challenge of imaging through a non-planar surface that is doubly curved was considered in chapter 3. This highlights another benefit of 2D arrays: the ability to accurately focus through surfaces that are curved in multiple directions. This chapter introduced a novel image-based surface extraction algorithm, whereby a point cloud is extracted from an initial starting location within the limits of defined constraints. The surface extraction method resulted in a surface estimation that was shown to be in very good agreement with the equation of the surface. Defects within the specimen were then imaged and able to be accurately positioned, further confirming the accuracy of the surface extraction. A parallel computing implementation process was also described as a solution for overcoming the slow processing times that is associated with generating 3D TFM images.

A scanned array system was introduced in chapter 4, whereby the doubly curved specimen that was introduced in chapter 3 was imaged by translating the array over the surface at defined intervals and collecting a data set at position. An algorithm was introduced to combine the individually generated surface TFM images to create a single, large image of surface of the specimen in a process that is termed as 'stitching'. The surface extraction method described in the previous chapter was then applied and used for generating internal TFM images. However, only subsections of the extracted surface points were used for interior imaging due to speed. Individual interior TFM images were then stitched to generate a single image of the interior of the specimen. The stitching method used here involved taking the maximum amplitude of voxels that were imaged from more than one array location. Defects at different depths within the specimen were then able to be accurately detected and positioned using the stitched 3D TFM image.

Chapter 5 introduces 3D sensitivity images, which are used to predict the TFM amplitude of a given scatterer at a specific location. An individual TFM image can be weighed by its associated sensitivity image at the same location to yield a normalised TFM image with uniform sensitivity. This was demonstrated to reduce the variation of maximum amplitudes of identical defects at increasing depths in a specimen. An alternative stitching method for a scanned array inspection is introduced using sensitivity images, whereby the amplitude at each voxel is the weighted sum of the individual contributions from each array position in a scan. This method is applied to the same FMC data set that was used in chapter 4.

Finally, chapter 6 then assessed both stitching methods by characterising 3D defects through planar and doubly curved surfaces. A range of machined defects were sized and their orientations determined. The results show that both stitching methods produce defects that are easily identified and sized, but using the sensitivity image method allows defects to be detected that would otherwise not be visible using the standard stitching TFM method. However, stitching using sensitivity images was found to take a significantly longer time to process.

7.2 Future work

The work presented in this thesis has laid the foundations for 3D volumetric TFM imaging using 2D phased arrays. There are numerous potential avenues which can

therefore be explored. As only longitudinal wave modes were considered throughout this work, multi-view 3D TFM imaging could be investigated as a way to increase knowledge of a defect to allow for accurate detection and characterisation. As this is an active area of research using 2D images, expanding to 3D could lead to more accurate inspections. Data fusion in 2D is also currently being investigated, so using data obtained from a 2D array could enable the generation of a single image with maximum defect information.

Another highly relevant area of further work relates to the measurement of 3D S-matrices as this is a topic that has yet to be fully explored. 3D S-matrices can be used in the sizing of small defects and could also allow a more accurate sensitivity model to be generated. In the current work a simplification was used and the defects were assumed to behave as point reflectors. However, by including the S-matrix for a particular defect in the sensitivity image, the design of multi-view TFM inspections could be improved.

The entire process of generating 3D volumetric TFM images is highly computationally intense and processing times can be on the order of tens of minutes for a single data set. Therefore, in order to allow substantial progress in 3D TFM imaging, optimisation of the processing method is necessary. A significant bottleneck in the imaging process is the determination of surface-crossing points for an immersion setup between array elements and image voxels. Accelerating these calculations through creating an initial coarse grid and numerous iterations of refining it could be a potential way to speed things up, however this method could be subject to the nature of the surface. Similarly, generating sensitivity images for larger regions can be beneficial when imaging complex surfaces. In the current work only a relatively small region around the array footprint was imaged, but the detection of defects that are not located directly under the array could be improved. Consequently, the sensitivity map could then be used to determine which regions to apply an imaging algorithm to, thereby potentially reducing the number of voxels in the imaging region.

When considering a scanned array inspection, in the current work 50% was chosen as the array overlap between scans. It would be interesting to investigate the relationship between defect detectability and characterisation with array overlap percentage. As it is desirable to complete an inspection as efficiently as possible, determining the minimum array overlap that maintains the ability to accurately characterise defects would be desirable. Additionally, as TFM imaging requires data stored in FMC format, the amount of data captured can quickly become large. Therefore, PWI could be investigated

as another method for generating 3D volumetric images. As this technique requires fewer transmissions and reduced data sizes, imaging using this method could speed up the long processing times associated with TFM imaging.

Appendix A

Differential evolution (DE)

First presented in [82], DE is a parallel direct search method which seeks to minimise non-linear and non-differentiable objective functions. With more than 24,000 citations at the time of writing the current work, it is one of the most popular algorithms for solving complex optimisation problems. An outline of the procedure is as follows.

First, NP D-dimensional parameter vectors, or agent vectors, act as the initial population of candidate solutions for each generation, G:

$$\mathbf{X}_{i,G} = \left\{x^1_{i,G}, x^2_{i,G}, \ldots, x^D_{i,G}\right\} \qquad i = 1,2,\ldots,NP \tag{A.1}$$

NP is constant throughout the process and commonly taken as $10D$. The initial agent population covers the entire search space by randomising the individuals within the search space by minimum and maximum parameter bounds:

$$x_{min} = \left\{x^1_{min}, x^2_{min}, \ldots, x^D_{min}\right\} \quad \text{and} \quad x_{max} = \left\{x^1_{max}, x^2_{max}, \ldots, x^D_{max}\right\}, \tag{A.2}$$

and is chosen randomly. Considering the ith agent vector in the first generation, the jth parameter is calculated using:

$$x^j_{i,0} = x^j_{min} + rand(0,\,1)\cdot\left(x^j_{max} - x^j_{min}\right) \qquad j = 1,2,\ldots,D \tag{A.3}$$

where $rand(0,1)$ represents a uniformly distributed random variable within the range [0, 1]. Once all agent vectors are initialised, a mutation operation is employed to generate a mutant vector, $\mathbf{V}_{i,G}$, with respect to each agent vector, $\mathbf{X}_{i,G}$, in the current population. For

each agent vector, its associated mutant vector, $\mathbf{V}_{i,G} = \left\{v^1_{i,G}, v^2_{i,G}, \ldots, v^D_{i,G}\right\}$, in generation G is created according to:

$$\mathbf{V}_{i,G} = x_{r_1,G} + F \cdot \left(x_{r_2,G} - x_{r_3,G}\right) \tag{A.4}$$

with random indexes $(r_1, r_2, r_3 \in i)$ where $r_1 \neq r_2 \neq r_3 \neq i$ and F is a real, constant scale factor within the range [0, 1].

To increase the diversity of the parameter vectors, a crossover operation is then applied to each corresponding pair of agent and mutant vectors to generate a trial vector: $\mathbf{U}_{i,G} = \left\{u^1_{i,G}, u^2_{i,G}, \ldots, u^D_{i,G}\right\}$. By employing a binomial crossover defined as:

$$u^j_{i,G} = \begin{cases} v^j_{i,G} & \text{if } rand_j(0,1) \leq CR \text{ or } j = j_{rand} \\ x^j_{i,G} & \text{otherwise} \end{cases} \qquad j = 1,2,\ldots,D \tag{A.5}$$

where the crossover rate, CR, controls the fraction of parameter values copied from the mutant vector and is within the range [0,1]. j_{rand} is a randomly chosen integer in the range [0, D] which ensures the trial vector gets at least one parameter from the mutant vector. The binomial crossover copies the jth parameter of the mutant vector to the corresponding element in the trial vector if $rand_j(0,1) < CR$ or $j = j_{rand}$. Otherwise, it is copied from the corresponding agent vector.

Once the trial vectors have been generated, the selection operation is performed. The objective function value is calculated for each trial vector, $f\left(\mathbf{U}_{i,G}\right)$, and compared to that of the corresponding agent vector, $f\left(\mathbf{X}_{i,G}\right)$ in the current population. If the trial vector yields a value less than or equal to the objective function value (for minimisation), the trial vector replaces the agent vector and enters the population of the following generation. Otherwise, the agent vector enters the next generation and the trial vector is discarded:

$$\mathbf{X}_{i,G+1} = \begin{cases} \mathbf{U}^j_{i,G} & \text{if } f\left(\mathbf{U}_{i,G}\right) \leq f\left(\mathbf{X}_{i,G}\right) \\ \mathbf{X}^j_{i,G} & \text{otherwise} \end{cases} \tag{A.6}$$

where $f(\cdot)$ is the objective function to be minimised. The entire process is repeated until a criterion is reached or all generations are completed. The agent vector that yields the minimum cost function is then returned as the best candidate solution. The larger the population size, the higher the probability of finding a global optimum. However, a larger

population size results in slower convergence rate and therefore a longer processing speed.

To apply this to the current work, 5 dimensional parameter vectors were used to correspond to 3 translations (x, y, z) and 2 rotations (around x and y axes). An initial population size, NP, was chosen as $10D = 50$. The DE algorithm ran with 1,000 generations using $F = 0.4$ and $CR = 0.3$. The trial vectors are applied to the extracted surface points to create an updated surface location. The RMSE value between the equation of the surface given in Eq. (3.6) and the updated extracted surface points is calculated and compared to the current minimum RMSE value. The minimum RMSE value is constantly updated with each generation until a stopping criterion reached to end the algorithm. This halted the DE algorithm when the number of consecutive generations which resulted in no change of minimum RMSE value reached 50, which for this example was after 14.5 minutes. The best agent vector returned contained the translation/rotation values that should be applied to the extracted surface points in order to minimise the RMSE between the surface and Eq. (3.6).

Bibliography

[1] Sung-Jin Song, Hyeon Jae Shin, and You Hyun Jang. Development of an ultra sonic phased array system for nondestructive tests of nuclear power plant components. *Nuclear Engineering and Design*, 214(1-2):151–161, may 2002.

[2] M A Drewry and G A Georgiou. A review of NDT techniques for wind turbines. *Insight - Non-Destructive Testing and Condition Monitoring*, 49(3):137–141, mar 2007.

[3] R A Smith, J M Bending, L D Jones, T R C Jarman, and D I A Lines. Rapid ultrasonic inspection of ageing aircraft. *Insight - Non-Destructive Testing and Condition Monitoring*, 45(3):174–177, mar 2003.

[4] Robin Clark. Rail flaw detection: overview and needs for future developments. *NDT & E International*, 37(2):111–118, mar 2004.

[5] Paul D. Wilcox. Ultrasonic arrays in NDE: Beyond the B-scan. *Review of Progress in Quantitative Nondestructive Evaluation*, 1511:33–50, 2013.

[6] Bruce W. Drinkwater and Paul D. Wilcox. Ultrasonic arrays for non-destructive evaluation: A review. *NDT & E International*, 39(7):525–541, oct 2006.

[7] Caroline Holmes, Bruce W. Drinkwater, and Paul D. Wilcox. Post-processing of the full matrix of ultrasonic transmit–receive array data for non-destructive evaluation. *NDT & E International*, 38(8):701–711, dec 2005.

[8] Aladin Carovac, Fahrudin Smajlovic, and Dzelaludin Junuzovic. Application of ultrasound in medicine. *Acta Informatica Medica*, 19(3):168, 2011.

[9] Bjørn A.J. Angelsen, Hans Torp, Sverre Holm, Kjell Kristoffersen, and T.A. Whittingham. Which transducer array is best? *European Journal of Ultrasound*, 2(2):151–164, apr 1995.

[10] William Kerr, Philip Rowe, and Stephen Gareth Pierce. Accurate 3D reconstruction of bony surfaces using ultrasonic synthetic aperture techniques for robotic knee arthroplasty. *Computerized Medical Imaging and Graphics*, 58:23–32, jun 2017.

[11] A. Velichko, P. D. Wilcox, Donald O. Thompson, and Dale E. Chimenti. Defect characterization using two-dimensional arrays. In *Review of progress in quantitative nondestructive evaluation*, pages 835–842, 2011.

[12] Shyamal C. Mondal, Paul D. Wilcox, and Bruce W. Drinkwater. Design of two-dimensional ultrasonic phased array transducers. *Journal of Pressure Vessel Technology*, 127(3):336, 2005.

[13] Y. Mendelsohn and E. Wiener-Avnear. Simulations of circular 2D phase-array ultrasonic imaging transducers. *Ultrasonics*, 39(9):657–666, aug 2002.

[14] A. Tweedie, V. Murray, and G. Hayward. Aperiodic and deterministic 2D phased array structures for ultrasonic imaging. In *2009 IEEE International Ultrasonics Symposium*, pages 406–409. IEEE, sep 2009.

[15] O Martínez. A small 2D ultrasonic array for NDT applications. *NDT & E International*, 36(1):57–63, jan 2003.

[16] Sivaram N. Ramadas, Joseph C. Jackson, Jerzy Dziewierz, Richard O'Leary, and Anthony Gachagan. Application of conformal map theory for design of 2-D ultrasonic array structure for ndt imaging application: a feasibility study. *IEEE Transactions on Ultrasonics, Ferroelectrics, and Frequency Control*, 61(3):496–504, mar 2014.

[17] F. Joseph Pompei and Shi-Chang Wooh. Phased array element shapes for suppressing grating lobes. *The Journal of the Acoustical Society of America*, 111(5):2040, 2002.

[18] Paul D. Wilcox and Jie Zhang. Quantification of the effect of array element pitch on imaging performance. *IEEE Transactions on Ultrasonics, Ferroelectrics, and Frequency Control*, 65(4):600–616, apr 2018.

[19] T. S. Barber, P. D. Wilcox, and A. D. Nixon. A comparison of 1D and 1.5D arrays for imaging volumetric flaws in small bore pipework. In *AIP Conference Proceedings*, pages 962–969, 2015.

[20] E. D. Light, R. E. Davidsen, J.O. Fiering, T. A. Hruschka, and S. W. Smith. Progress in two-dimensional arrays for real-time volumetric imaging. *Ultrasonic Imaging*, 20(1):1–15, jan 1998.

[21] Léonard Le Jeune, Sébastien Robert, Eduardo Lopez Villaverde, and Claire Prada. Multimodal plane wave imaging for non-destructive testing. *Physics Procedia*, 70:570–573, 2015.

[22] Rosen K. Rachev, Paul D. Wilcox, Alexander Velichko, and Kevin L. McAughey. Plane wave imaging techniques for immersion testing of components with nonplanar surfaces. *IEEE Transactions on Ultrasonics, Ferroelectrics, and Frequency Control*, 67(7):1303–1316, jul 2020.

[23] A. Velichko and A. J. Croxford. Strategies for data acquisition using ultrasonic phased arrays. *Proceedings of the Royal Society A: Mathematical, Physical and Engineering Sciences*, 474(2218):20180451, oct 2018.

[24] R.J. Ditchburn, S.K. Burke, and C.M. Scala. NDT of welds: state of the art. *NDT & E International*, 29(2):111–117, apr 1996.

[25] A.N. Sinclair and A.M. Chertov. Radiation endurance of piezoelectric ultrasonic transducers – A review. *Ultrasonics*, 57:1–10, mar 2015.

[26] Mohammad Hossein Amini, Anthony N. Sinclair, and Thomas W. Coyle. A new high-temperature ultrasonic transducer for continuous inspection. *IEEE Transactions on Ultrasonics, Ferroelectrics, and Frequency Control*, 63(3):448–455, mar 2016.

[27] Jean-Pierre Monchalin. Laser-ultrasonics: Principles and industrial applications. *e-Journal of Nondestructive Testing*, 25(3), 2020.

[28] S.E. Burrows, Y. Fan, and S. Dixon. High temperature thickness measurements of stainless steel and low carbon steel using electromagnetic acoustic transducers. *NDT & E International*, 68:73–77, dec 2014.

[29] K. Turkowski. Filters for common resampling tasks. *Graphics Gems*, pages 147–165, 1990.

[30] R. V. Murphy. Ultrasonic defect-sizing using decibel drop methods volume I: Text. Technical report, N.B. Research & Productivity Council, 1987.

[31] Harry A. Bloxham, Alexander Velichko, and Paul David Wilcox. Combining simulated and experimental data to simulate ultrasonic array data from defects in materials with high structural noise. *IEEE Transactions on Ultrasonics, Ferroelectrics, and Frequency Control*, 63(12):2198–2206, dec 2016.

[32] Alan J. Hunter, Bruce W. Drinkwater, and Paul D. Wilcox. Autofocusing ultrasonic imagery for non-destructive testing and evaluation of specimens with complicated geometries. *NDT & E International*, 43(2):78–85, mar 2010.

[33] W. Deutsch, M. Joswig, Klaus Maxam, S. Nitsche, Tubes Düsseldorf, A. Noël, Patrick Pichard, and S. Deutsch. Phased array ultrasonic testing of heavy-wall seamless tubes by means of a testing portal authors:. 2010.

[34] Joseph L. Rose. Surface and subsurface waves. In *Ultrasonic Guided Waves in Solid Media*, pages 107–119. Cambridge University Press, New York, 2014.

[35] Miles Weston, Peter Mudge, Claire Davis, and Anthony Peyton. Time efficient auto-focussing algorithms for ultrasonic inspection of dual-layered media using Full Matrix Capture. *NDT & E International*, 47:43–50, apr 2012.

[36] Arthur Schuster. *An introduction to the theory of optics*. Edward Arnold, London, 1909.

[37] R. Long, J. Russell, P. Cawley, N. Habgood, Donald O. Thompson, and Dale E. Chimenti. Ultrasonic phased array inspection of flaws on weld fusion faces using full matrix capture. In *AIP Conference Proceedings*, pages 848–855. AIP, 2009.

[38] Robert E. Malkin, Amanda C. Franklin, Rhodri L.T. Bevan, Hiroshige Kikura, and Bruce W. Drinkwater. Surface reconstruction accuracy using ultrasonic arrays: Application to non-destructive testing. *NDT & E International*, 96:26–34, 2018.

[39] L. Le Jeune, S. Robert, P. Dumas, A. Membre, and C. Prada. Adaptive ultrasonic imaging with the total focusing method for inspection of complex components immersed in water. In *Review of Progress in Quantitative Nondestructive Evaluation*, pages 1037–1046, Boise, Idaho, 2015.

[40] A. Tweedie, R.L. O'Leary, G. Harvey, A. Gachagan, C. Holmes, P.D. Wilcox, and B.W. Drinkwater. Total focussing method for volumetric imaging in immersion non destructive evaluation. In *2007 IEEE Ultrasonics Symposium Proceedings*, pages 1017–1020. IEEE, oct 2007.

[41] B W Drinkwater and A I Bowler. Ultrasonic array inspection of the Clifton Suspension Bridge chain-links. *Insight - Non-Destructive Testing and Condition Monitoring*, 51(9):491–498, sep 2009.

[42] J. Russell, R. Long, and P. Cawley. Development of a twin crystal membrane coupled conformable phased array for the inspection of austenitic welds. *Review of Progress in Quantitative Nondestructive Evaluation*, 30:811–818, 2011.

[43] R. Long, P. Cawley, Donald O. Thompson, and Dale E. Chimenti. Further development of a conformable phased array device for inspection over irregular surfaces. In *AIP Conference Proceedings*, volume 975, pages 754–761. AIP, 2008.

[44] James P. Kirkpatrick, Paul D. Wilcox, and Robert A. Smith. Row–column addressed arrays for nondestructive evaluation applications. *IEEE Transactions on Ultrasonics, Ferroelectrics, and Frequency Control*, 66(6):1119–1128, jun 2019.

[45] Olivier Roy, Steve Mahaut, and Olivier Casula. Control of the ultrasonic beam transmitted through an irregular profile using a smart flexible transducer: modelling and application. *Ultrasonics*, 40:243–246, 2002.

[46] O Casula, C Poidevin, G Cattiaux, and G Fleury. A flexible phased array transducer for contact examination of components with complex geometry. In *Proceedings of the 16th World Conference on NDT*, 2004.

[47] Frédéric Lasserre, David Roue, Juergen Laube, Philippe Dumas, Bruno Kingler, François Cartier, and Olivier Roy. Industrialization of a large advanced ultrasonic flexible probe for non-destructive testing of austenitic steel pieces with irregular surface. *Journal of Civil Engineering and Architecture*, 11(10), oct 2017.

[48] Blair Rocks, Fabrizio Gaudenzi, Daniel Irving, and David Allan Hughes. Fully-flexible thin-film ultrasonic array for use in industrial NDE applications. In *2019 IEEE International Ultrasonics Symposium (IUS)*, pages 2493–2495. IEEE, oct 2019.

[49] J. Dziewierz and A. Gachagan. Computationally efficient solution of snell's law of refraction. *IEEE Transactions on Ultrasonics, Ferroelectrics, and Frequency Control*, 60(6):1256–1259, jun 2013.

[50] Grand Roman Joldes, Adam Wittek, and Karol Miller. Real-time nonlinear finite element computations on GPU – Application to neurosurgical simulation. *Computer Methods in Applied Mechanics and Engineering*, 199(49-52):3305–3314, dec 2010.

[51] Joshua A. Anderson, Chris D. Lorenz, and A. Travesset. General purpose molecular dynamics simulations fully implemented on graphics processing units. *Journal of Computational Physics*, 227(10):5342–5359, may 2008.

[52] Cris Cecka, Adrian J. Lew, and E. Darve. Assembly of finite element methods on graphics processors. *International Journal for Numerical Methods in Engineering*, 85(5):640–669, feb 2011.

[53] Peter Huthwaite. Accelerated finite element elastodynamic simulations using the GPU. *Journal of Computational Physics*, 257:687–707, jan 2014.

[54] CUDA C++ programming guide `https://docs.nvidia.com/cuda/cuda-c-programming-guide/index.html`.

[55] Hossein Taheri, Lucas Koester, Timothy Bigelow, Leonard J. Bond, Dominique Braconnier, Ewen Carcreff, Gavin Dao, Alan Caulder, and Ahmed Arabi Hassen. Fast ultrasonic imaging with total focusing method (TFM) for inspection of additively manufactured polymer composite component. In *ASNT 27th Annual Research Symposium Proceedings*, pages 212–220. ASNT, oct 2018.

[56] Frederic Cegla. High temperature ultrasonic monitoring with permanently installed sensors. In *Proceedings of the National Seminar & Exhibition on Non-Destructive Evaluation*, pages 360–363, 2011.

[57] C. Mineo, Douglas Herbert, S. Pierce, M. Morozov, I. Nicholson, and I. Cooper. Robotic non-destructive inspection. 2013.

[58] B.L. Luk, A.A. Collie, D. S. Cooke, and S. Chen. Walking and climbing service robots for safety inspection of nuclear reactor pressure vessels. *Measurement and Control*, 39(2):43–47, mar 2006.

[59] Robert Bogue. Robots in the nuclear industry: a review of technologies and applications. *Industrial Robot: An International Journal*, 38(2):113–118, mar 2011.

[60] Caroline Holmes, Bruce W. Drinkwater, and Paul D. Wilcox. Advanced post-processing for scanned ultrasonic arrays: Application to defect detection and classification in non-destructive evaluation. *Ultrasonics*, 48(6-7):636–642, nov 2008.

[61] Kalyanmoy Deb and Deb Kalyanmoy. *Multi-objective optimization using evolutionary algorithms*. John Wiley Sons, Inc., USA, 2001.

[62] Swagatam Das and Ponnuthurai Nagaratnam Suganthan. Differential evolution: A survey of the state-of-the-art. *IEEE Transactions on Evolutionary Computation*, 15(1):4–31, feb 2011.

[63] Lawrence E. Kinsler, Austin R. Frey, Alan B. Coppens, and James V. Sanders. *Fundamentals of acoustics*. John Wiley & Sons, 4th edition, 2000.

[64] Jeffrey T. Stetson and Walter De Odorico. Robotic inspection of fiber reinforced composites using phased array UT. pages 1889–1895, 2014.

[65] E. Cuevas, M. López, and M García. Ultrasonic techniques and industrial robots: natural evolution of inspection systems. In *4th International Symposium on NDT in Aerospace*, Ausburg, Germany, 2012.

[66] C Mineo, S G Pierce, B Wright, I Cooper, and P I Nicholson. PAUT inspection of complex-shaped composite materials through six DOFs robotic manipulators. *Insight - Non-Destructive Testing and Condition Monitoring*, 57(3):161–166, mar 2015.

[67] Nicolas Budyn, Rhodri Bevan, Anthony J. Croxford, Jie Zhang, Paul D. Wilcox, Artem Kashubin, and Peter Cawley. Sensitivity images for multi-view ultrasonic array inspection. In *AIP Conference Proceedings*, page 080001, 2018.

[68] Nicolas Budyn, Rhodri L. T. Bevan, Jie Zhang, Anthony J. Croxford, and Paul D. Wilcox. A model for multiview ultrasonic array inspection of small two-dimensional defects. *IEEE Transactions on Ultrasonics, Ferroelectrics, and Frequency Control*, 66(6):1129–1139, jun 2019.

[69] Rhodri L. T. Bevan, Nicolas Budyn, Jie Zhang, Anthony J. Croxford, So Kitazawa, and Paul D. Wilcox. Data fusion of multiview ultrasonic imaging for characterization of large defects. *IEEE Transactions on Ultrasonics, Ferroelectrics, and Frequency Control*, 67(11):2387–2401, nov 2020.

[70] Lester W. Schmerr. *Fundamentals of ultrasonic phased arrays*, volume 215 of *Solid Mechanics and Its Applications*. Springer International Publishing, 2015.

[71] Josef Krautkrämer and Herbert Krautkrämer. *Ultrasonic testing of materials*. Springer Berlin Heidelberg, Berlin, Heidelberg, 4th edition, 1990.

[72] Jie Zhang, B. Drinkwater, and P. Wilcox. Defect characterization using an ultrasonic array to measure the scattering coefficient matrix. *IEEE Transactions on Ultrasonics, Ferroelectrics and Frequency Control*, 55(10):2254–2265, oct 2008.

[73] Long Bai, Alexander Velichko, and Bruce Drinkwater. Ultrasonic characterization of crack-like defects using scattering matrix similarity metrics. *IEEE Transactions on Ultrasonics, Ferroelectrics, and Frequency Control*, 62(3):545–559, 2015.

[74] Minghui Li and Gordon Hayward. Optimal matched filter design for ultrasonic NDE of coarse grain materials. In *AIP Conference Proceedings*, page 020011, 2016.

[75] A. V. Oppenheim and G. C. Verghese. Signals, systems and inference — class notes for 6.011: Introduction to communication, control and signal processing spring 2010 (MIT) `https://ocw.mit.edu/courses/electrical-engineering-and-computer-science/6-011-introduction-to-communication-control-and-signal-processing-spring-2010/readings/MIT6{_}011S10{_}chap14.pdf` , 2010.

[76] Fatma Doga Ocal and Yuchun Xu. Using ndt techniques to detect and characterise the damage of end-of-life components in remanufacturing. *InImpact: The Journal of Innovation Impact*, 7:136, 2016.

[77] Jie Zhang, Bruce W. Drinkwater, and Paul D. Wilcox. The use of ultrasonic arrays to characterize crack-like defects. *Journal of Nondestructive Evaluation*, 29(4):222–232, dec 2010.

[78] Maria V. Felice, Alexander Velichko, and Paul D. Wilcox. Accurate depth measurement of small surface-breaking cracks using an ultrasonic array post-processing technique. *NDT & E International*, 68:105–112, dec 2014.

[79] Long Bai, Alexander Velichko, and Bruce W. Drinkwater. Ultrasonic defect characterisation—Use of amplitude, phase, and frequency information. *The Journal of the Acoustical Society of America*, 143(1):349–360, 2018.

[80] Chaoyong Peng, Long Bai, Jie Zhang, and Bruce W. Drinkwater. The sizing of small surface-breaking fatigue cracks using ultrasonic arrays. *NDT & E International*, 99:64–71, 2018.

[81] Ichiro Komura, Taiji Hirasawa, Satoshi Nagai, Jun-ichi Takabayashi, and Katsuhiko Naruse. Crack detection and sizing technique by ultrasonic and electromagnetic methods. *Nuclear Engineering and Design*, 206(2-3):351–362, jun 2001.

[82] Rainer Storn and Kenneth Price. Differential evolution – a simple and efficient heuristic for global optimization over continuous spaces. *Journal of Global Optimization*, 11(4):341–359, 1997.